SPATIOTEMPORAL DYNAMICS OF SOLAR RADIATION IN THE HIMALAYA: TOPOGRAPHIC FORCING AND GLACIER DYNAMICS

A Dissertation

by

ILIYANA DANCHEVA DOBREVA

Submitted to the Office of Graduate and Professional Studies of
Texas A&M University
in partial fulfillment of the requirements for the degree of

DOCTOR OF PHILOSOPHY

Chair of Committee,	Charles W. Lafon
Committee Members,	Vatche P. Tchakerian
	Anthony Filippi
	Courtney Schumacher
Head of Department,	David Cairns

December 2019

Major Subject: Geography

ABSTRACT

Glaciers across the Himalaya exhibit significant spatial variations in morphology and dynamics. Climate, topography and debris cover variations are thought to significantly affect glacier fluctuations and glacier sensitivity to climate change, although the role of topography and solar radiation forcing have not been adequately characterized and related to glaciers. Analyzed are a set of glaciers in the Karakoram mountain range, where a clustering of surge type glaciers occurs. The objective of this works is to investigate topographic effects on glacier state, such as if a glacier is of surge type or not, and if a glaciers is retreating or advancing. Specifically, the focus of this work is the spatiotemporal effects of solar radiation on glaciers as modulated by the topography. A geomorphic assessment of the glaciers is also performed, so that solar radiation forcing could be studied in the appropriate context. A rigorous GIS-based solar radiation model that accounts for the direct and diffuse-skylight irradiance components was developed and applied for an ablation season over the study area. The model accounts for multiple topographic effects on the magnitude of surface irradiance. Enhanced ablation was determined to be a distinguishing characteristic of surge type glaciers as indicated by the positive relation between ablation-season surface irradiance and the probability of a glacier being of surge type, as well as by the positive relation between lesser topographic shielding and the probability of a glacier being of surge type. These results demonstrate the important role that local and regional topography plays in governing climate-glacier dynamics in the Himalaya.

DEDICATION

To my husband, Jonathan Willis.

CONTRIBUTORS AND FUNDING SOURCES

Contributors

This work was supervised by Dr. Michael Bishop. The solar radiation simulations over the ablation season were performed in the research group of Dr. Steve Liu, and model parallelization was accomplished as a Master thesis by Da Liang. Dr. Andrew Bush reviewed and provided comments and edits on the text of the literature review and the solar radiation modeling. Bethany Beeler and Tyler Adams performed language editing and proofreading of the dissertation.

Funding Sources

Graduate study was supported by graduate teaching and research assistantships in the Department of Geography, Texas A&M University during the period of 2010 - 2015. Starting in 2016, the student was employed full time as a research associate at the Department of Soil and Crop Sciences, Texas A&M University in the research group of Dr. Dirk Hays.

TABLE OF CONTENTS

LIST OF FIGURES

FIGURE Page

LIST OF TABLES

1. INTRODUCTION

1.1 Research statement

The purpose of this research is to investigate the spatiotemporal dynamics of solar radiation in the Karakoram mountain range in the context of the topographic forcings on glacier dynamics. The Spectral-Topographic Solar Radiation Model (STSRM) accounting for multiscale topographic variations was developed and utilized to simulate direct and diffuse irradiance for the duration of an ablation season over the central portion of the Karakoram mountain range. A sample of glaciers was then characterized based on their geomorphic and surface irradiance properties, which were related to glacier state. This research is a component in furthering the knowledge of mountain geodynamcis as the coupling of climate, erosional processes, and tectonics is imprinted on the topography, which in turn is a forcing on glacial erosional processes.

1.2 Context and significance

Various Earth systems are in a state of transition due to climate change, and this has resulted in glacier retreat, ecosystem migration, an increase in natural hazards, and water resource issues (Vörösmarty et al., 2000; Walther et al., 2002; Beniston, 2003; Parmesan, 2006; Van Aalst, 2006; Akhtar et al., 2008; Xu et al., 2009). Changes in the Earth's cryosphere are one indicator of climate change (Anthwal et al., 2006; Kääb et al., 2012; Stocker et al., 2013), as the cryosphere is regulated by surface irradiance, atmosphic temperature and precipitation. Arctic sea ice and Northern Hemisphere snow cover are decreasing (Comiso et al., 2008; Brown and Robinson, 2011; Stroeve et al., 2014), the Antarctic and Greenland ice sheets are losing mass (Velicogna, 2009; Hanna et al., 2013; Shepherd et al., 2018), and glaciers worldwide are generally receding (Kaser et al., 2006; Gardner et al., 2013; Pendleton et al., 2019), although in some regions such as the Karakoram mountain range some glaciers are observed to be advancing (Kääb et al., 2012; Gardelle et al., 2013; Bishop et al., 2014). Furthermore, climate change increases human vulnerability due to temperature anomalies, as well as changes to precipitation regimes, and also increases the risk of adverse short-term events such as heat waves, intensified drought, storms, and flooding (Patz et al., 2005; Van Aalst, 2006; Bouwer, 2011; Ciscar et al., 2011; Pant et al., 2018).

Sea level rise, one of the most direct indicators of climate change, is due to melting of land ice and due to thermal expansion of oceans, and has a direct impact on coastal areas. Sea level rise observed through tidal gauges and satellite altimetry for the period of 1880 to 2009 is about 210 mm (Church and White, 2011). The consequences of sea level rise are inundation of wetlands and lowlands, increase in coastal erosion, and increase in saltwater penetration into groundwater, rivers and farmland (Vellinga and Leatherman, 1989). As a result sea level rise poses a threat due to flooding, damage to farmland and to coastal infrastructure. Shoreline erosion is of particular concern as coastlines are overdeveloped (Pilkey and Cooper, 2004). Additional concern is the loss of protective natural barriers that would expose the coastlines to natural hazards due to storm surges.

Melting of land ice contributes to sea level rise, but there are only limited mass balance measurements of mountain glaciers and therefore a better approach to deriving changes in mass balance is through satellite observations. The Gravity Recovery and Climate Experiment (GRACE) provides monthly gravity observations that allow the calculations of mass variations and it has been estimated that glaciers, excluding the Antarctic and Greenland ones, had contributed 0.41 ± 0.08 mm yr^{-1} to sea level rise for the period of January 2003 to December 2010 (Jacob et al., 2012). There is a high uncertainty for the record over the High Mountain Asia with an estimate of -4 ± 20 Gt yr^{-1} (Jacob et al., 2012).

Central Asia hosts the largest glaciated areas outside of the polar regions including the Himalaya mountain range with an estimated glaciated area of 33, 500 km^2 and the

Karakoram mountain range with an estimated glaciated area of 16, 600 km^2 (Dyurgerov and Meier, 2005). Assessing the impact of glacier change in the region is complicated due to the heterogeneous nature of the regional climates and terrain which results in varying glacier dynamics through the region. The two major climate forcing factors to glacier mass balance are solar radiation and precipitation. The Himalaya, however, exhibits a complex topography which modulates the effects of these forcings. Furthermore, the topography is not uniform through the region, and thus there are different effects on the glacier systems in the Himalaya.

Himalayan glaciers are a dynamic component of the Earth system with consequences not only to global sea level rise, but also to regional hydrological regimes. The societal impact of glaciers is enhanced due to the natural hazards they pose to local communities such as slope failure, snow avalanches, glacier outburst flooding, glacier surging, and glacier valley lake impoundments (Richardson and Reynolds, 2000; Kääb et al., 2003; Van Aalst, 2006; Helmer and Hilhorst, 2006; Ashraf et al., 2012; Harrison et al., 2018; Haritashya et al., 2018; Sherpa et al., 2019). Glacial Lake Outburst Floods (GLOFs) are the most catastrophic glacial hazard. GLOFs cause loss of life, destruction of property, and environmental degradation such as damage to agricultural land and destabilization of valley walls. In the Himalaya, GLOFs have increased in frequency during the second half of the 20$^{\text{th}}$ century (Richardson and Reynolds, 2000).

Human vulnerability to glacial fluctuations is also related to the threat to water resources that decreasing glaciers cause. The Himalayan region is known as the Asian Water Towers as it feeds major rivers (Xu et al., 2009; Immerzeel et al., 2010; Rowan et al., 2018), regulates downstream agriculture (Rasul, 2010, 2014, 2015), and governs ecosystem stability (Postel, 2003). As this is a vast area, not all rivers are impacted the same. For example, Immerzeel et al. (2010) demonstrated through analysis of normalized melt index that meltwater is important in the Indus and Brahmaputra basins and less important for the

Ganges, Yangtze, and Yellow river basins. Assessing the impact of glacier change on water resources requires understanding of the climate and topographic forcings on glaciation.

The Karakoram mountain range is one of the most intriguing geographic regions in the world. Active tectonics and the relatively young age of the mountain have created a spectacular high-relief topography. Climatically, the region is affected by winter western disturbances and the Southwest Indian summer monsoon providing sufficient snowfall to sustain some of the largest mountain glaciers on Earth. Since more remote sensing data has become available, we have learned that many of the glaciers in this region are surge type, which are glaciers that undergo long periods of inactivity followed by relative short periods of extreme terminus advance. Furthermore, very few of these glaciers are retreating, contrary to the world-wide trend of glacier retreat due to global warming. Thus, determining the unique glacier and environmental characteristics of the region has become an active area of research. This study is positioned within the glaciological framework of investigating the unique environmental conditions allowing for a clustering of predominantly surge type glaciers in the Karakoram mountain range.

1.3 Research questions and objectives

The main hypothesis of this work is that there is a topographic influence on the amount of solar radiation reaching glaciated surfaces, and thus there is a topographic control on glacier dynamics and glacial erosion. The main question that this work addresses is if and how geomorphic and surface irradiance characteristics of glaciers in the Karakoram mountain range are related to glacier dynamics. The following two objectives are pursued.

1.3.1 Objective 1

Develop and validate a robust solar radiation model that accounts for multiscale topographic variations and utilizes spectral characterization of solar radiation and atmospheric transmittance, long-term orbital variations, and subpixel calculations of cast shadow. The model was developed to study the influence of topography on climate-glacier dynamics.

1.3.2 Objective 2

Relate geomorphic and surface irradiance characteristics of glaciers in the Karakoram mountain range to glacier state. This objective examines the topographic controls on glacier dynamics. Glacier state is utilized as a proxy of glacier dynamics. Due to the unique environmental conditions of the region, the Karakoram mountain range is dominated by surge type glaciers, so statistical analysis was performed on surge type glaciers. Due to the small sample of advancing and retreating glaciers, only a qualitative analysis on advancing and retreating glaciers is performed.

2. STUDY AREA

The central Karakoram mountain range in Pakistan is the focus of this study (Figure 2.1). The Karakoram mountain range was formed at the collision of the Indian and Asian plates roughly 50 Ma ago, relatively recent in geologic timescale. The mountain range is characterized by relief production due to high erosion and uplift rates (Searle, 1991; Bishop et al., 2014). The study area was selected to extend over the Indus-Yarlung sature zone, and encompasses 74.3 - 76.8 decimal degrees East and 35.5°N - 36.7°N. The Main Karakoram Thrust line is located just south of the Hispar and Biafo glaciers, and the Karakoram Fault line lays to the north of the Hispar and Biafo glaciers (Searle, 1991).

The study area was selected because if includes glaciers at different states such as advancing and surge type glaciers which are rare globally. The so-called Karakoram Anomaly is well documented and an active area of research (Hewitt, 2011; Bishop et al., 2014; Bolch et al., 2017). The Karakoram mountain range exhibits unique geologic and climatological properties, along with the unanswered questions of why the glaciers there differ from the rest of the world, and thus is an appropriate setting for studying the geomorphic and surface irradiance properties of glaciers and how these relate to glacier state.

With over seven kilometers of topographic relief, the region exhibits high magnitude processes (Searle, 1991). It is also heavily glaciated with varying estimates of total glacierized area according to different studies: from 16,600 km^2 (Dyurgerov and Meier, 2005) to 21,771 km^2 (Arendt et al., 2012). Glaciers are visualized on the false-color composite of Landsat 8 images in Figure 2.1. The areas of greatest altitudes are in the southeast portion of the region near the K2 peak, and the lowest altitudes are in the southwest portion of the study area associated with the Indus River valley (Figure 2.2).

This region includes the large Batura, Hispar, Baltoro, and Biafo glaciers, as well as

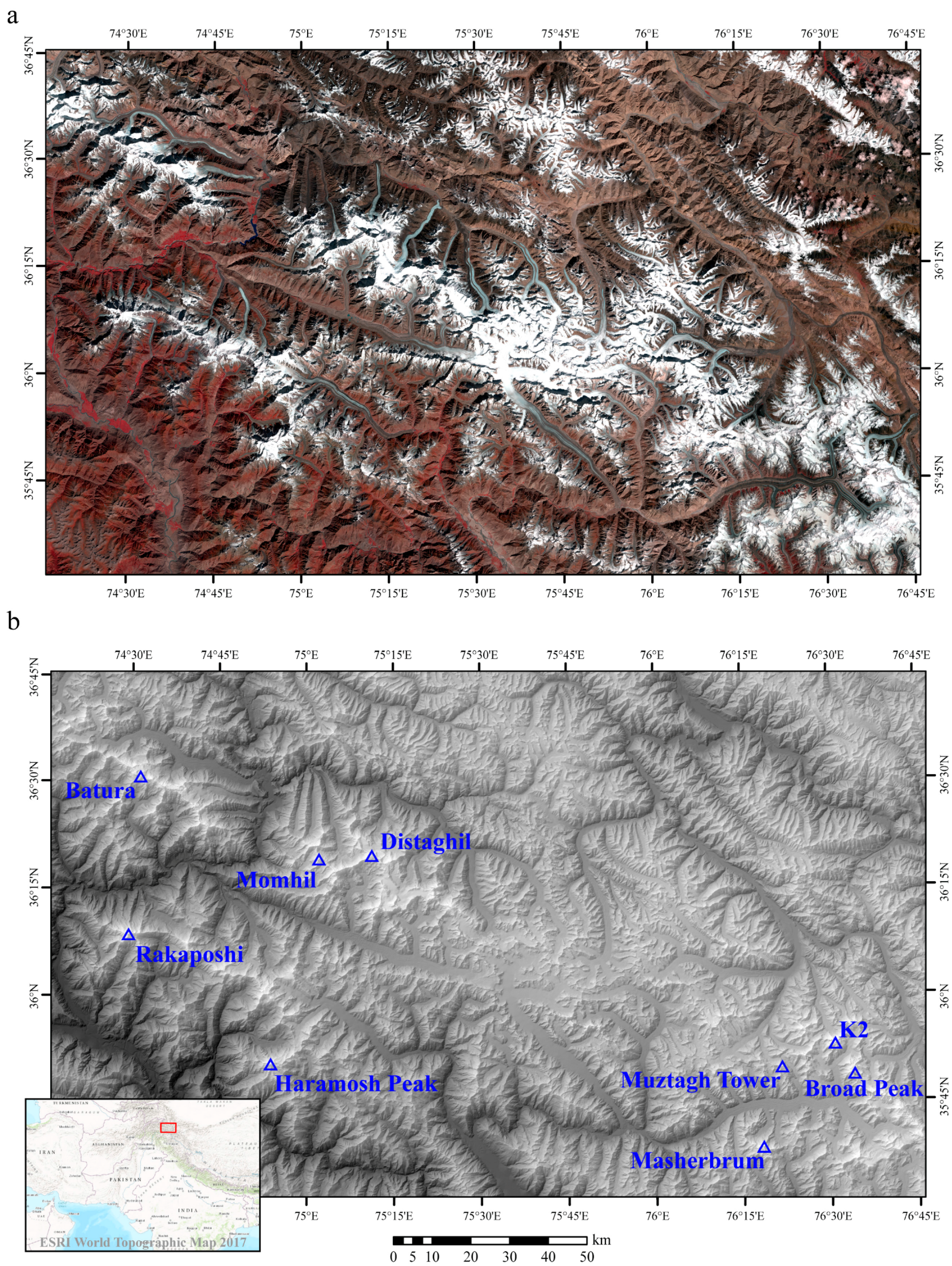

Figure 2.1: A map of the study area located in the Karakoram mountain range. The figure displays a Landsat 8 false-color composite image where near-infrared region of the electromagnetic spectrum is displayed as red, the red region of the electromagnetic spectrum - as green, and the green region of the electromagnetic spectrum - as blue (a). A Shuttle Radar Topographic Mapping Mission (SRTM) digital elevation model (DEM) shaded-relief map of the central Karakoram mountain range with major peaks identified is also displayed (b). Figure is reprinted with permission from Dobreva et al. (2017).

numerous smaller and intermediate-sized glaciers. Most of the glaciers in the area are heavily debris-covered, with larger glaciers exhibiting numerous ice cliffs and supraglacial lakes.

2.1 Topography

The Karakoram mountain range exhibits an extreme topographic complexity. Landscape evolution of the Karakoram mountain range has been studied (Seong et al., 2008, 2009; Shroder et al., 2011; Bishop et al., 2010). Seong et al. (2009) performed glaciological fieldwork including a geochronology, and concluded that the region had experienced significant glacial fluctuations. The interactions of climate, tectonics, and erosion are imprinted on the topography (Bishop and Dobreva, 2016), where glacial erosion is an active landscape process (Seong et al., 2008).

Altitude alone affects a suite of environmental variables such as air pressure, air temperature, and vegetation patterns (Huggett and Cheesman, 2002). The study area exhibits an extreme topographic variability (Figure 2.2) with a maximum elevation of eight and a half kilometers at the K2 peak in the northwest corner of the study area, down to a little over a kilometer at the Indus river valley in the southeast. The decrease in minimum altitude and also the lower mean altitude in the East shows this East-West gradient.

Relief in the study area is greatest in the east half and it decreases in the west half of the study area. The greater relief in the east half is due to the low altitude of the Indus river valley, and in the west half the minimum elevation is higher and thus the lower relief. Relief production is caused by different processes but generally erosion acts to reduce altitude, while differential uplift enhances altitude. Thus, the combination of glacial erosion and differential uplift are a major mechanism for relief production, and a forcing on landscape evolution in the Karakoram mountain range. Other processes affecting relief production are mass deposition which reduces relief, and climate-glacial erosion feedback which places a limit on maximum elevation (Seong et al., 2009)

Terrain slope and aspect are two fundamental properties of the topography. Terrain slope has a direct effect on erosional processes due to gravity. The study area is characterized with numerous cliffs with extreme near vertical walls. This is demonstrated in Figure 2.3 with slopes ranging up to 87° coinciding with the highest altitude in the region. The orientation structure of the terrain is directly affecting the energy fluxes on the landscape as it determines which areas are exposed to the Sun at any moment. The main orientation of the Karakoram mountain range is northwest to southeast. However, there are valley slopes oriented at different directions reflecting the complex erosional history of the region.

Terrain openness, also referred here as skyview, is the portion of the sky that is visible at any point on the landscape (Dozier and Frew, 1990; Bishop and Shroder, 2004). Thus, it is an indication of the exposure of the terrain to solar radiation. Figure 2.4 demonstrates that large valleys such as the ones of the Hispar, Batura and Baltoro glaciers are nearly completely exposed, while smaller valleys are more shielded. Most shielding corresponds to the slopes right below the highest peaks and ridges on the landscape.

Topography and climate are related through the effects of topography on surface irradiance through terrain orientation and openness, and through the effects of terrain orientation and altitude on orographic precipitation. Orographic precipitation as a major accumulation source is directly related to a glacier catchment's orientation towards the prevailing winds and the altitude of the accumulation area of the glacier. The Karakoram mountain range acts as a barrier to both winter western disturbances and the Southwest Indian summer monsoon, and thus any humid air masses that reach the region deposit precipitation according to the corresponding wind direction.

Winter western disturbances which are instabilities in the subtropical westerly jet stream are commonly observed at the 500 hPa geopotential height (Cannon et al., 2015a,b) which varies around 5600 m. With respect to the Southwest Indian summer monsoon, Dimri et al.

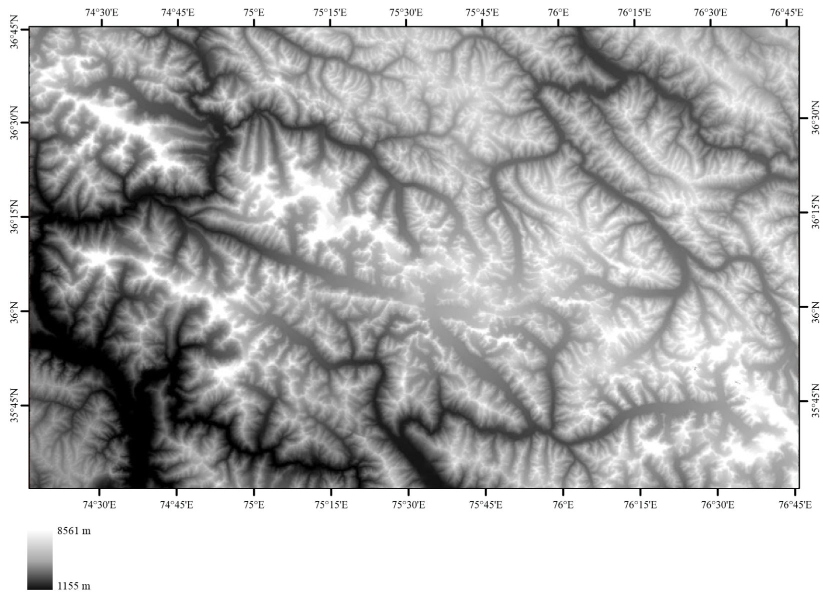

Figure 2.2: Elevation map of the study area.

(2013) demonstrated through simulations with regional climate models that orographic uplift is triggered by variations in topography at altitudes of approximately 4 km.

2.2 Climate

The climate of the Karakoram mountain range is described as mid-latitude high-mountain type with cold winters and mild summers (Forsythe et al., 2015). The Karakoram mountain range exhibits the expected altitudinal temperature and precipitation gradients given the high relief of the region. The region is under the influence of the winter western disturbances (Cannon et al., 2015a,b), and the Southwest Indian summer monsoon (Benn and Owen, 1998; Hewitt, 2014; Annamalai and Sperber, 2016). The Tibetan Anticyclone also affects the region mainly through its interaction with the Southwest Indian summer monsoon (Wake, 1989; Mayer et al., 2006).

Teleconnections are also affecting the active climate systems in the region. Research shows that a decrease in the intensity of the Southwest Indian summer monsoon during the

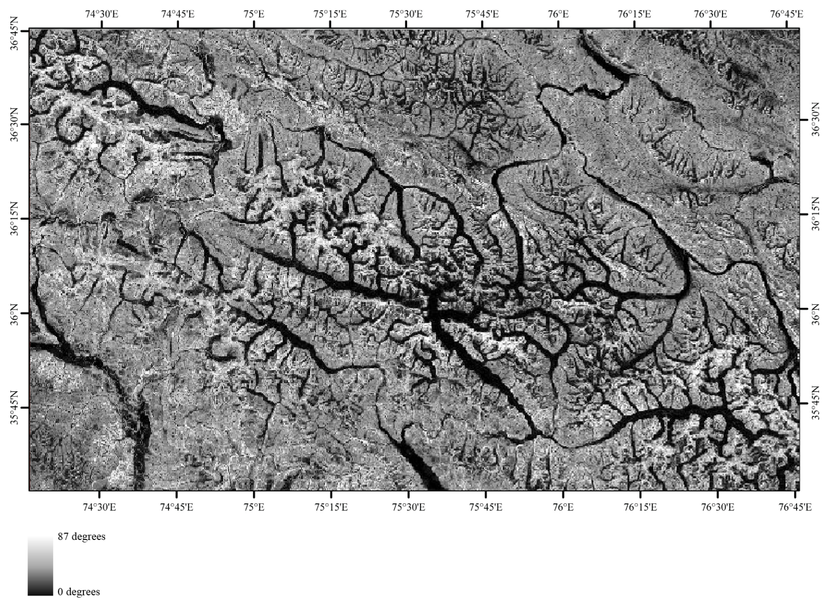

Figure 2.3: Terrain slope map of the study area. Values range from 0° in black to 87° in white.

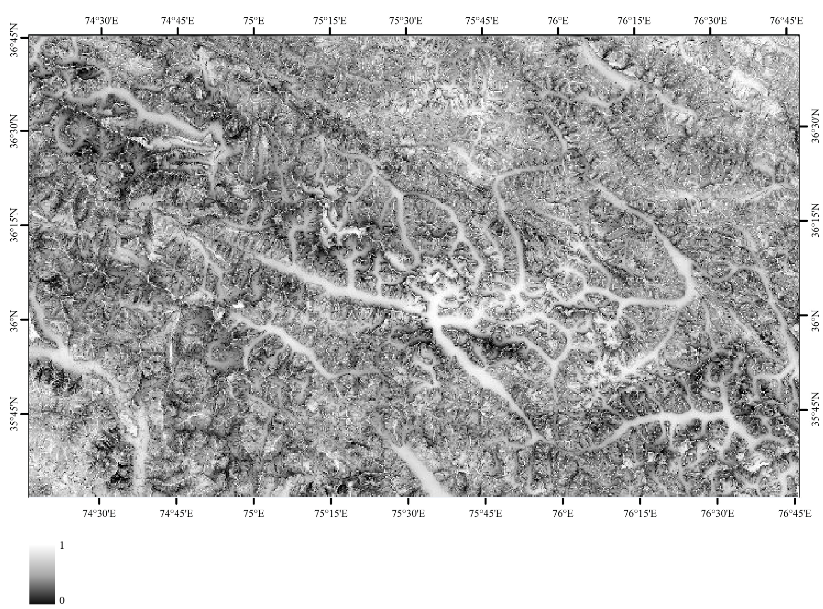

Figure 2.4: Skyview map of the study area. Values range from 0 in black to 1 in white.

El Niño phase of the El Niño-Southern Oscillation (ENSO) resulting in decrease of summer precipitation (Webster and Yang, 1992; Bishop et al., 2010). The opposite relationship is demonstrated with respect to winter western disturbances, where an increase in winter western disturbances during El Niño is demonstrated (Cannon et al., 2015a,b) implying an increase in winter precipitation.

The Pacific Decadal Oscillation (PDO) has similar but weaker in amplitude affect as compared to ENSO, and thus modulates the effects of ENSO in the region (Krishnamurthy and Krishnamurthy, 2014; Veettil et al., 2016). Specifically, the positive phase of PDO increases the influence of El Niño on the monsoon, and the opposite during negative PDO. A third teleconnection affecting the Karakoram mountain range is the Indian Ocean Dipole (IOD), which is also modulating the El Niño phase of ENSO by increasing the extremities in Southwest Indian summer monsoon precipitation (Gadgil et al., 2004; Maity and Nagesh Kumar, 2006).

Climate trends in temperature and precipitation are difficult to estimate as there are only a limited number of weather stations in the region, and they are mostly located in lower altitudes. Archer and Fowler (2004) and Fowler and Archer (2006) performed an analysis of the climate record in the Upper Indus Basin for the period 1895 to 1999 and found an increase in winter and summer precipitation, and a decrease in summer mean temperature.

2.3 Glaciers

The documented advancing and thickening of some Karakoram glaciers has been named the Karakoram Anomaly (Hewitt, 2005; Bishop et al., 2014). Moreover, the prevalence of surge type glaciers and the occurrence of advancing glaciers distinguishes this region's glaciers from the worldwide trend of retreat (Hewitt, 2005, 2011; Bolch et al., 2012; Bishop et al., 2014; Bolch et al., 2017).

Fundamental characteristics of the Karakoram glaciers is their debris cover. Mölg et al. (2018) estimated that glaciers across the region are about 10% debris covered. This study utilized Landsat images to estimate the debris cover. A limitation of debris cover mapping is that it is a challenge to estimate the depth of the debris, and at the same time the effects of debris-cover on glaciers is related to the depth and type of debris. Studies on Batura glacier, provided estimates of the depth of the debris cover. Bishop et al. (1995) estimated that 75.3% of the total area of Batura glacier is covered with debris more than 0.3 m deep. At such depth, the debris cover isolates the glacier from solar energy, however, rain water peculating down to the glacier surface and refreezing is a source of heat.

As the remoteness of the Karakoram glaciers has limited the necessary fieldwork studies, we base a lot of our understanding of glacier dynamics on estimates of glacier velocities. Glacier velocities are useful in studies of surge type glaciers, because glacier surges involve an increase in glacier velocity from 10 to 100 times greater than when the glacier is in its quiescent phase (Cuffey and Paterson, 2010). Moreover, latitudinal glacier velocity profiles may provide clues if a surge is thermally or hydrologically triggered. The study of Karakoram glacier dynamics through velocities information, however, is currently inconclusive with earlier studies pointing to thermal controls (Quincey et al., 2011), and later studies indicating both hydrological and thermal controls (Lv et al., 2018).

3. LITERATURE REVIEW *

The feedback between climate and topography in the context of glaciology is important to study because solar radiation is the main energy source for glacial ablation, and the spatiotemporal variability of surface irradiance is controlled locally by the terrain. Thus, this research addresses new aspects of climate-glaciers dynamics in the Himalaya. Nearly all of the energy available for glacier melt is provided by short-wave irradiance fluxes, and only a small amount is due to sensible and latent heat (Cuffey and Paterson, 2010). The development of a new GIS-based solar radiation model with better parameterizations of topography allows us to start quantifying the effects of topography on surface irradiance (Bishop et al., 2015). This literature review includes a broader discussion about the climate of the Karakoram mountain range as this is an important context for understanding Karakoram glacier dynamics. Secondly, this literature review includes a discussion focused on glaciers and climate-glacier dynamics. Finally, reviewed are existing solar radiation models.

3.1 Climate

The Karakoram mountain range is characterized by a mid-latitude high-mountain climate with cold winters and mild summers (Forsythe et al., 2015). Most of the precipitation over the area is due to winter western disturbances (Cannon et al., 2015a,b), even though western disturbances likely contribute during other times of the year. The contribution by western disturbances can, however, be influenced by other geographically remote factors through teleconnections (Bush, 2001; Bishop et al., 2010). The Southwest Indian summer monsoon, which is a part of the larger Asian-Australian monsoon system (Annamalai and Sperber, 2016), is also an important contributor to precipitation in the region (Benn and

*Sections 3.1 and 3.2 are reused with permission from the publication: "Climate-Glacier Dynamics and Topographic Forcing in the Karakoram Himalaya: Concepts, Issues and Research Directions" by Dobreva, I.D., Bishop, M.P., and Bush, A.B.G. Water 2017, 9(6), 405.

Owen, 1998; Hewitt, 2014). A third synoptic-scale climate feature affecting the region is the Tibetan Anticyclone, which is strong during the summer and affects the intrusion of the Southwest Indian summer monsoon into the Karakoram mountain range (Wake, 1989; Mayer et al., 2006). A recently discovered atmospheric system is the Karakoram/Western Tibetan vortex with studies focused on its effects on the climate of the western Tibetan Plateau (Li et al., 2018, 2019)

3.1.1 Climate systems

The subtropical westerly jet stream (also referred to as the westerlies) is a general circulation wind belt, driven by the thermal gradient between approximately 30° latitude and the poles in both hemispheres (Harman, 1991). Energy transport occurs due to cyclones and anticyclones which are generated through instability of the subtropical westerly jet stream as well as its interaction with the thermal and topographic characteristics of the underlying land masses and ocean (Harman, 1991). Western disturbances can also be generated by the notch between the western Himalaya and the Hindu Kush mountains (Lang and Barros, 2004), resulting in eastward-propagating extratropical cyclones that are prevalent over the Karakoram mountain range mainly during the winter and spring (Cannon et al., 2015a,b), but that are also observed during the summer (Bush, 2001; Bishop et al., 2010).

The cold fronts of these cyclones propagate into the warm tropical air mass of the Indian subcontinent. Precipitated water from these storm systems was originally evaporated from the Mediterranean, Red, Persian, Caspian, and Arabian Seas (Filippi et al., 2014; Cannon et al., 2015b). Even more importantly, the cyclones interact with the topography of the Karakoram mountain range, producing orographic precipitation that sustains the glaciers in the region (Machguth, 2014; Mölg et al., 2014). The influence of the winter western disturbances in the Karakoram mountain range does not have a specific geographic limit. Some research (e.g. Roohi, 2007), however, delineates climate geographic regions over

Pakistan through climate station data for the period 1951-2000. Roohi (2007), who utilized data from only a small number of stations at high altitude, shows that the region mainly influenced by the subtropical westerly jet stream is north of 35°N, and the area to the south of 35°N is mostly affected by the Southwest Indian summer monsoon. It should be noted that other research had demonstrated that the Karakoram mountain range is indeed affected by winter western disturbances (Cannon et al., 2015a,b).

The Karakoram mountain range is primarily dominated by the subtropical westerly jet stream, with dominant snowfall occurring in winter and spring, and with observed increases in winter precipitation over time (Archer and Fowler, 2004; Bolch et al., 2012; Yao et al., 2012). Teleconnections influence the circulation, and therefore regulate precipitation, particularly if they enhance the influence of the subtropical westerly jet stream (Bhutiyani et al., 2010; Janes and Bush, 2012; Ahmad et al., 2015; Cannon et al., 2015b). Simulation studies indicate that precipitation forcing could dominate until 2050, after which enhanced internal convective motion due to debris cover and increasing temperatures will dominate, suggesting that Karakoram glaciers will eventually exhibit negative mass balance (Janes and Bush, 2012; Collier et al., 2015).

The Karakoram mountain range is also heavily influenced by the Southwest Indian summer monsoon, part of the broader Asian-Australian monsoon system. The monsoon is driven by seasonal contrasts in surface temperature between the ocean and land surfaces. Related to the comparatively stable ocean temperature, land-surface temperature varies seasonally being relatively hot during the summer and relatively cold during the winter. The resulting pressure gradients drive the seasonal monsoon winds, with a reversal of the winds during the summer (as compared to winter) when the pressure gradient reverses. Monsoon rainfall therefore varies significantly over the dry and wet seasons. In the northern hemisphere summer, the monsoon extends from the Arabian Sea north and eastward into southern and southeastern Asia. During the southern hemisphere summer, it extends in the opposite direction westward towards Africa (Clift and Plumb, 2008). The importance of the Southwest Indian summer monsoon for Karakoram glaciers is that it generates topographically induced summer precipitation over much of Pakistan and India with intrusions into the Karakoram mountain range.

The strength of the monsoon plays a crucial role in regulating precipitation and snow accumulation (Bush et al., 2004; Janes and Bush, 2012). Monsoon incursions reach into the Karakoram mountain range during the summer months (Mayer et al., 2014), and teleconnections between tropical sea-surface temperatures and the strength of the monsoon have been shown to potentially dominate orbital forcing (Bush, 2001). The monsoon is thought to be responsible for the observed decreases in summer temperatures due to documented increase in cloud cover (Zafar et al., 2016), and thus summer cloudiness may be a contributing factor to snow accumulation. Research has validated the summertime cooling trend since the 1960s (Fowler and Archer, 2006; Shekhar et al., 2010). From a topographic perspective, the monsoon reaches into the Karakoram mountain range (via glacial valley pathways) and into the Hunza region and easterly over the Baltoro Glacier near K2 Mountain (Figure 3.1).

The Southwest Indian summer monsoon reaches deeper into the region when there is a weakening of the Tibetan anticyclone, which is a synoptic scale feature centered over Tibet in the summer. The Tibetan anticyclone is an upper tropospheric subtropical anticyclone that migrates from the Bay of Bengal in the winter to the Tibetan Plateau in the summer (Raghavan, 1973). The summer mode is referred to as the Tibetan anticyclone (Raghavan, 1973) or Inner Asian high-pressure system (Hewitt, 2014). It has a warm core and affects both regional weather conditions and large-scale atmospheric circulation (e.g. Yanai and Wu, 2006). Relevant to the study of Karakoram glaciers is that, during the irregular weakening of the Tibetan Anticyclone, the Southwest Indian summer monsoon reaches the Karakoram mountain range and deposits large amounts of precipitation (Wake, 1989;

Figure 3.1: Monsoon snowfall on the Baltoro glacier, as seen from Urdokas. Photo credit is to Andrew G.B. Bush, 2005; figure is reprinted with permission from Dobreva et al. (2017).

Mayer et al., 2006).

Teleconnections have a large influence on the climate patterns and dynamics over south Asia, particularly, those arising from disturbances in the tropical Pacific Ocean (e.g. Bush, 2001; Annamalai and Sperber, 2016). ENSO, for example, exhibits global effects through the planetary wave propagation that arises from surface forcing caused by sea surface temperature anomalies in the central and eastern tropical Pacific Ocean (e.g. Diaz and Markgraf, 2000). Additionally, the characteristics of ENSO can be altered by midlatitude processes (Bush, 2007).

Climate research shows that the intensity of the monsoon is negatively correlated with ENSO, such that during El Niño the monsoon is generally weaker but during La Niña it is stronger (e.g. Webster and Yang, 1992). Weakening of the Indian summer monsoon produces less precipitation and droughts whereas the stronger La Niña monsoon produces enhanced precipitation (Kumar et al., 1999; Krishnamurthy and Kirtman, 2009). The observed correlation between ENSO and the monsoon does not, however, guarantee a weakening of the Indian summer monsoon during an El Niño event due to the statistical nature of the relationship (Kumar et al., 1999; Bhutiyani et al., 2010; Gill et al., 2015). Elucidating a clearer understanding of the dynamical relationship between ENSO and the monsoon is important, as it is one of the important factors governing precipitation over the glaciers in the Karakoram mountain range.

The subtropical westerly jet stream is also strongly influenced by ENSO. During El Niño, a weaker monsoon implies that the influence of the subtropical westerly jet stream over the Karakoram mountain range is increased (Bishop et al., 2010; Veettil et al., 2016). An increase in winter precipitation during El Niño was also found for Northwestern India, with greater moisture flux from the Caspian and Arabian Seas (Dimri, 2013). Conversely during La Niña a strong monsoon reduces the influence of the subtropical westerly jet stream over the Karakoram mountain range. Through Empirical Orthogonal Function

(EOF) analysis, it was demonstrated that the leading EOF of observed precipitation variability contained 63.4% of the variance and was significantly correlated with the Southern Oscillation Index (Ahmad et al., 2015).

Another teleconnection pattern with influence over the Karakoram mountain range is the Pacific Decadal Oscillation (PDO). The PDO represents a combination of processes operating on different time scales and is driven by remote tropical forcing and North Pacific atmosphere-ocean interactions (Mantua et al., 1997; Newman et al., 2016). The teleconnection pattern associated with the PDO is similar to that of ENSO, only weaker in amplitude. It therefore modulates the effects of ENSO on the monsoon such that the positive phase of PDO increases the influence of El Niño on the Indian Summer monsoon (Krishnamurthy and Krishnamurthy, 2014; Veettil et al., 2016). Thus, when an El Niño event coincides with a positive PDO, there is a much weaker Southwest Indian summer monsoon than what is expected by the effects of El Niño alone. It was also demonstrated through a comparison between the leading EOF of observed precipitation variability and the 200 hPa geopotential height that there is a significant connection between spring precipitation in Pakistan and the Pacific-North American (PNA) teleconnection pattern associated with the PDO (Ahmad et al., 2015).

The equatorial Indian Ocean has a direct influence on the Southwest Indian summer monsoon and, like the Pacific Ocean, it exhibits interannual variability in the form of the Indian Ocean Dipole (IOD) which, like ENSO, is characterized by sea surface temperature anomalies. A composite index of ENSO and the IOD shows a significant relationship between Southwest Indian summer monsoon precipitation extremes and this composite index suggesting that, when the two teleconnections are in phase, the extremity of the Southwest Indian summer monsoon precipitation anomalies is enhanced (Gadgil et al., 2004). A similar conclusion was reached through a Bayesian dynamic modeling approach that determined the phases of ENSO and of the IOD have similar effects on Southwest

Indian summer monsoon precipitation (Maity and Nagesh Kumar, 2006).

3.1.2 Climate change and trends

Precipitation trends can be analyzed using weather station data, although existing stations are located at much lower elevations than the glaciers. Archer and Fowler (2004) analyzed the precipitation record of 17 stations in the Upper Indus Basin, which range from the Karakoram mountain range to the Hindu Kush mountain ranges. Station altitudes ranged between 980 m to 2394 m, and the time period ranged from 1895 to 1999. The authors found no significant trend in either annual or seasonal precipitation for the entire period; however, there was a positive trend in winter and summer precipitation for the period from 1961 to 1999.

Temperature trends for the same period using weather station data showed a significant increase in winter mean and maximum temperature (Fowler and Archer, 2006). The mean and minimum summer temperature, on the other hand, both exhibited a significant decrease. The authors suggest the observed increase in summer precipitation as a possible explanation for the decrease in summer mean temperature. The decrease in summer minimum temperature could be explained if there were a decrease in cloud cover during the night as this would allow more radiation to escape to space, but there is no data to support such an explanation.

The observed increase in winter and summer precipitation and decrease in summer temperature could explain the advance of glaciers in the Karakoram mountain range, as opposed to the glaciers in the central and eastern Himalaya. The increase in winter temperature is not important for the ablation of glaciers, as winter temperatures are below zero, and a modest increase would not raise the temperature above the freezing point. The decrease in summer mean temperature, however, is important because it occurs during the ablation season.

3.2 Glaciers

The global trend of glacier recession is paralleled in most of the Himalaya with variations in glacier state across the Himalaya and within the Karakoram mountain range. A regional-scale study was performed across eastern and western Himalaya, the Karakoram mountain range, and Pamir (Gardelle et al., 2012, 2013). A Shuttle Radar Topography Mission (SRTM) DEM from February 2000 was compared to DEMs from SPOT5 stereo images from 2008 to 2011. It was found that glaciers in the eastern and western Himalaya exhibit negative mass balance, while some glaciers in the Karakoram mountain range and Pamir exhibit positive mass balance. The total mass balance of the glaciers in the Pamir-Himalaya-Karakoram region was still estimated as negative at -0.14 $\pm$ 0.08 m yr^{-1}. It should be noted that the uncertainty of mass balance estimates derived through differencing of DEMs is related to the accuracy of these elevation datasets (Mukul et al., 2017), and preprocessing of DEMs to reduce error is essential (Nuth and Kääb, 2011).

Another regional-scale study of glacier thickness changes was performed by utilizing Ice, Cloud, and land Elevation Satellite (ICESat) altimetry data for 2003-2008 and the SRTM DEM (Kääb et al., 2012; Kääb et al., 2015). The large spatial footprint of ICESat allows for a comprehensive study of Himalayan mass balance change. The study confirmed the Karakoram Anomaly, but it also determined that the Karakoram mountain range is at the western limit of the region where glaciers are gaining mass with the largest mass gain present at the Eastern Nyainqêntanglha. Kääb et al. (2015) estimated 21,000 km^2 of glacierized area in the Karakoram mountain range and a net mass balance of -0.10 $\pm$ 0.06 m yr^{-1}.

The documented advancing and thickening of some Karakoram glaciers has been named the Karakoram Anomaly, in contrast to the decline of glaciers in other parts of the world (Hewitt, 2005). There are different estimates of the total glaciated area in the Karakoram mountain range: 16,600 km^2 (Dyurgerov and Meier, 2005); 21,771 km^2 (Arendt et al., 2012); and 21,000 km^2 (Kääb et al., 2015). The historical record of the state of retreat and advance of glaciers since the end of the Little Ice Age is lacking due to limited observations. A review of the observations of the Himalayan and Karakoram glaciers between 1850 and the 1970s is available by Mayewski and Jeschke (1979). Noted in the Karakoram was the presence of glaciers which were surging, but these were excluded from the analysis, as the authors determined that such glaciers represent only a small portion of the record and that the surges were spurious. From the rest of the observations, it was established that the glaciers in the region including the Karakoram mountain range were: either retreating or advancing between 1850 and 1880; equally in a state of retreat, advance, and stability between 1880 and 1940; or, in a state of retreat between 1940 and the 1970s (Mayewski and Jeschke, 1979). Since the late 1990s, the Karakoram glaciers are reported to have stabilized, and in certain high altitude areas, to advance, along with a great number of surge type glaciers (Hewitt, 2005, 2011; Bishop et al., 2014; Rankl et al., 2014; Sevestre and Benn, 2015; Bhambri et al., 2017).

3.2.1 Unique glacier characteristics

Several distinct glacier and environmental characteristics are offered as a possible explanation for the Karakoram Anomaly. Due to the geographic setting of the mountain range, both subtropical westerly jet stream and Southwest Indian summer monsoon reach the glaciers and supply precipitation. The glaciers are also heavily debris-covered which modulates the ablation regime of the glaciers. Arguably, climate change is affecting both precipitation and ablation; thus, glaciers may oscillate due to periodic influxes of mass. Furthermore, supraglacial lakes and ice cliffs can cause high ablation which will cause glacier downwasting. Since we do not have data to support these arguments, we are focused on identifying and quantifying each of the processes affecting Karakoram glaciers, such as the topographic effects on irradiance. Other processes that must be quantified are also the specific effects of debris load, orographic precipitation variations, basal ablation, ice velocity, but also others that ultimately determine glacier sensitivity to climate change.

Surge type and advancing glaciers, as well as positive mass balance conditions in the Karakoram mountain range, are related to the region's unique snowfall regime (Hewitt, 2011). Given a strong orographic effect, the maximum precipitation is deposited above the snow line creating favorable conditions for glacier formation and relatively high ice fluxes contributing to some of the largest glaciers outside of the polar regions (Hewitt, 2011). Extreme relief, steep slopes and high magnitude erosion processes and sediment fluxes generate significant debris loads over glaciers of all sizes, thus significantly altering the ablation regime of these glaciers (Mihalcea et al., 2008; Scherler et al., 2011; Collier et al., 2013, 2014, 2015).

In terms of the ablation regime of Himalayan glaciers, it is important to quantify how much of the ablation happens where different glacier features are located. Thus, an estimation of the ablation regime of a glacier may be possible if the spatial distribution of various features is mapped. Given this objective, Juen et al. (2014) applied a distributed ablation model to study ablation rates in western China. The authors estimated through image analysis that debris-cover extends over 32% of the glacier, and that ice cliffs and supraglacial lakes encompass 1.7% and 0.36% of the debris-covered area, respectively. The authors found that the ice cliffs account for much less ablation than previously reported - between 7% and 16% of the total ablation in the debris-covered area of this glacier, while the ablation over all debris-covered area accounts for between 17% and 33% of the total ablation of the glacier. Still, according to Kraaijenbrink et al. (2016), the effects of supraglacial lakes and ice cliffs counteract the effects of debris-cover on some glaciers, to the extent that Himalayan debris-covered glaciers may have similar rates of surface height change as debris-free glaciers.

A very important distinguishable characteristic according to Hewitt (2011) is the presence of thick debris-cover but only over portions of glacier surfaces (see Figure 2.1). For example, Bishop et al. (1995) utilized remote-sensing image analysis to estimate that 75.3% of the total area of Batura glacier is covered with debris more than 0.3 m deep. In certain areas, however, only a thin layer of debris is present, enhancing ablation, while there are also areas of clear ice where ablation is not enhanced. The portions covered with thin layers of debris, or those that are debris-free, are sensitive to summer precipitation as the occurrence of snowfall limits ablation. Note that debris-covered glaciers are also sensitive to precipitation, and ablation can occur at depth as the water makes it way to the glacier base.

The presence of debris-cover on Karakoram glaciers is an important surface property, as it modulates ablation rates. Any impurities on the glacier surface, including thin debris-cover, lowers the albedo of the glacier surface and thus enhances ablation. As the debris-cover thickens, it may insulate the glacial ice from the surface irradiance causing lower ablation. At the same time, debris-cover may allow rain to peculate deeper into the glacier which releases latent heat when the rain freezes and which in turn enhances ablation. Thus, the effects of thermal properties of debris-cover on Karakoram glaciers is important (Scherler et al., 2011; Benn et al., 2012; Rowan et al., 2015) and is expected to lead to erroneous mass balance estimates if not accounted for. Reznichenko et al. (2010) studied the effects of debris-cover on glacier ice in a laboratory environment. The insulating effect of thicker debris-cover (greater than 5 cm) is only possible when diurnal cycles of radiation forcing are present, as nighttime allows for the absorbed energy to be emitted back to the atmosphere. Another important finding was the impact of the permeability of debris-cover on heat transfer during rain events. In particular, thin and highly porous debris allows rain to reach the ice and advect heat to the glacier surface. However, if the debris is not highly permeable, the rain may freeze within the debris-cover at night and stay frozen during the day, not allowing further rain to reach the glacier surface, thereby decreasing ablation.

Rowan et al. (2015) coupled ice flow and debris-cover within the iSOSIA numerical model (Egholm et al., 2011), and included mass-balance and debris-accumulation feedback. The model was applied to the Khumbu Glacier, Nepal, revealing that the glacier responded to warming by mass loss and thinning - and not by a decrease in its spatial extent. The debris-cover also slowed the response of the glacier to warming. Even though the Khumbu Glacier is not located in the Karakoram mountain range and is in a different climate setting, the results of the study are still transferable, as the glacier is large, heavily debris-covered, and mostly avalanche-fed. This modeling effort focused on the spatial pattern of debris-cover but ignored the temporal evolution of debris production.

In the Karakoram mountain range, Mihalcea et al. (2008) investigated the effects on glacier ablation through a distributed surface energy-balance study. The research involved remote-sensing, ASTER, and field data to derive the spatial distribution of debris-cover over the Baltoro Glacier and a meteorological station adjacent to the glacier in order to measure the energy available at that location. This study also highlighted the importance of accounting for debris-cover in the energy regime of the glaciers.

Alternatively, Collier et al. (2015) investigated the effects of debris-cover on glacier-atmospheric interactions by introducing surficial debris to the coupled atmosphere-glacier model WRF-CMB. Accounting for debris-cover is essential to the modeling of Karakoram glaciers because excluding debris-cover could lead to an approximately 14% overestimation of ice loss. It should also be noted that there is a feedback between climate and erosion because debris-cover is a function of the erosional processes in the vicinity of a glacier, since mass movement supplies the material that is deposited on the glacier. In addition, debris-cover is also a function of the topography of the terrain because steep accumulation areas are related to the formation of debris-covered glaciers (Scherler et al., 2011). Understanding debris production and its effects on glaciers is essential, and it has been demonstrated by Scherler et al. (2011) that similar climate settings result in different glacier behavior in the Himalayas depending on the presence of debris-cover.

Debris-cover is highly variable, both horizontally and vertically, with most of it being present in the ablation area of the Karakoram glaciers, and with thickness generally increasing toward the terminus of the glaciers, reaching a maximum depth greater than 5 m (Bishop et al., 2010). Mapping debris-cover and estimating its depth are active research areas in glaciology (Bishop et al., 1995; Mihalcea et al., 2006, 2008; Bhardwaj et al., 2014; Ghosh et al., 2014; Veettil et al., 2014; Khan et al., 2015; Carenzo et al., 2016). An innovative study also mapped geochemical composition of debris-cover cover through in-situ and remote sensing spectral analysis (Casey and Kääb, 2012; Casey et al., 2012).

Some of the early work on debris-cover mapping was performed by Bishop et al. (1995), using SPOT images and ISODATA unsupervised classification to derive not only the spatial variability but also the thickness of debris-cover. Mihalcea et al. (2006, 2008) utilized the thermal ASTER bands and mapped the spatial distribution and thickness of debris-cover through a correlation between surface kinetic temperature and debris-cover characteristics. This correlation was applied over the Baltoro glacier even though it was developed over the Miage Glacier, Italy with a stronger correlation of $R = 0.8$ over a continuously debris-covered area, as well as a weaker relationship of $R = 0.69$ over the whole glacier tongue. Khan et al. (2015) also mapped different types of land cover common in glacierized basins such as perennial snow-cover, clean ice, and debris-covered ice. This is a semi-automated approach, using Landsat images and terrain slope as inputs to a supervised maximum likelihood classification that segments the study area, which is then completed by manual post-processing. All of these efforts in mapping debris-cover are essential, as we need to be able to better characterize glacier surface energy-balance conditions.

The presence of ice cliffs and supraglacial lakes is another unique characteristic of Karakoram glaciers (Figures 3.2 and 3.3) as both of these features are associated with high-magnitude ablation. Ice cliffs contribute considerably to the overall ablation of a glacier even though they often cover only a small percentage of the glacier surface (Han et al., 2010; Basnett et al., 2013; Reid and Brock, 2014; Buri et al., 2016; Kraaijenbrink et al., 2016). Theoretically, these features and glacier ablation form a positive feedback loop - an ice cliff exposes clean ice which is then covered by a thin layer of debris enhancing the ablation of the exposed ice. At the same time, supraglacial lakes also exhibit low albedo. Thus, both the ice cliffs and the supraglacial lakes increase ablation. The enhanced ablation further contributes to the expansion of the ice cliffs and supraglacial lakes. In actuality, ablation rates on ice cliffs vary according to their orientation and inclination, local shielding effects, and the presence of debris-cover as demonstrated on the Lirung and Khumbu Glaciers, Nepal (Sakai et al., 2002).

Ice-cliff formation, however, has not been studied sufficiently with only two formation mechanisms described in the literature - ice cliffs can be formed when the roof of an englacial conduit collapses or when a debris-layer slides and exposes clear ice (Sakai et al., 2002, 1998, 2000; Kirkbride, 1993). Ice cliffs occur commonly over the lower portions of a glacier due to mass wasting, thinning of the ice, and the eventual collapse of the roof of conduits. When that happens, the resulting feature appears as a funnel-shaped sink hole (Kirkbride, 1993). Ice cliffs are dynamic and are further modified by ablation and ice flow.

Sakai et al. (2002) identified four types of ice cliffs during their study of Lirung Glacier, Nepal - decayed, temporary, developed, and stable. When they are first developed, their area increases. When they are stable their area does not change. Decaying ice cliffs lose their surface area. The identified temporary ice cliffs were formed due to debris-layer sliding during the monsoon season, and are covered again with debris in the post-monsoon season.

Ice cliffs vary in shape but also in type due to their different orientation, as orientation represents a strong controlling factor for ice-cliff ablation. On Lirung Glacier, Nepal, ice

Figure 3.2: A debris-covered ice cliff and a small supraglacial lake on Baltoro glacier. Photo credit is to Andrew G.B. Bush, 2005; figure is reprinted with permission from Dobreva et al. (2017).

Figure 3.3: A large supraglacial lake surrounded by ice cliffs on Blatoro glacier. Photo credit is to Andrew G.B. Bush, 2005; figure is reprinted with permission from Dobreva et al. (2017).

cliffs facing north to west were larger and were determined to have continuous ice exposure with similar ablation at their lower and upper parts, and thus these ice cliffs maintained their steep slopes (Sakai et al., 2002). At the same time, ice cliffs facing northeast to south were smaller and appeared shielded at their lower portions exhibiting lower slopes, which also tend to be covered by debris. Sakai et al. (2002) explain these differences given variations in shortwave and longwave irradiance. A more recent object-oriented analysis of glacier features on Langtang Glacier, Nepal also identified north-facing ice cliffs as larger and often accompanied by a supraglacial lake formation (Kirkbride, 1993).

Further insight into ice-cliff dynamics was gained by Buri et al. (2016) who developed a grid-based model of cliff backwasting which accounts for the interactions between shortwave and longwave irradiance, and glacier topography. The model was applied to two ice-cliff features on Lirung Glacier, Nepal, and pre-monsoon, monsoon, and post-monsoon radiation fluxes were computed. In all six scenarios, the diffuse irradiance was the largest shortwave component when compared to direct or adjacent-terrain irradiance, with mean diffuse irradiance varying from 48.8% to 64.8% of the mean incident shortwave irradiance. In four out of the six scenarios, the mean outgoing longwave irradiance was larger than the mean incoming longwave irradiance. However, the amount of the incoming longwave irradiance is still important with the sky-longwave irradiance dominating but with considerable mean debris-emitted longwave irradiance ranging from 24.2% to 27% of the total incident longwave irradiance. These estimates confirm the importance of considering the terrain but also the type and relative location of debris-cover when examining the effects of ice cliffs on ablation.

Ablation is enhanced due to exposed ice, so often supraglacial lakes are formed at the base of ice cliffs. Kraaijenbrink et al. (2016) demonstrated the prevalence of these coupled systems by mapping them over a lower portion of the Langtang Glacier, Nepal. Supraglacial lake formation is also of extreme interest because such lakes are a hazard for the onset of Glacial Lake Outburst Floods (GLOFs) and large lakes upstream from mountain communities are often monitored (Reynolds, 2000; Kargel et al., 2016; Song et al., 2016). Thus, most of the effort in studying glacier lake formation has been focused on moraine-dammed lakes at the terminus of the glaciers which are at risk of GLOFs, and Sakai and Fujita (2010) demonstrated statistically that such lakes form on glaciers where the inclination of the glacier surface is less than 2° and also where there has been lowering of the glacier surface since the Little Ice Age.

In terms of supraglacial lakes not at the terminus of the glacier, the general understanding is that they are also due to lowering of the glacier surface. Kraaijenbrink et al. (2016) deployed an unmanned aerial vehicle (UAV) over Langtang Glacier, Nepal and found that glacier surface curvature is not related to the presence of supraglacial lakes - the authors identified a decrease in the total extent of supraglacial lakes over a relatively straight stretch of the glacier.

Essential to our understanding of Karakoram glaciers is consideration of the highly variable ice dynamics even along portions of the same glacier (Copland et al., 2009; Quincey et al., 2009; Scherler and Strecker, 2012; Quincey et al., 2015). Glacier profiles of ice velocities provide insight into glacier dynamics and can be used to identify surge type glaciers in their active phase of surging. Paul et al. (2015) introduced a procedure for deriving glacier velocities developed within the Glaciers Climate Change Initiative (CCI) of the European Space Agency (ESA). Ice velocities currently may be derived through offset tracking of either repeat optical remote sensing images or SAR images (Paul et al., 2015).

3.2.2 Glacier state overview

Glacier fluctuation rates are often used to characterize glacier state as stable, retreating, advancing, or oscillating. Depending on the time frame of the analysis glaciers may be characterized as exhibiting different states. In addition, glaciers that appear stable according to their terminus location may be downwasting and still loosing mass.

Bishop et al. (2014) describe the glaciers in the central Karakoram mountain range as fluctuating differently according to environmental variability. In particular, the authors identified location, topographic variation and debris-cover as affecting the variability in glacier fluctuations. However, we have not yet been able to predict glacier type as a function of these environmental conditions. This study is contributing to the efforts of predicting glacier state by relating glacier geomorphic and surface irradiance characteristics to the probability of a glacier being a surge type ot not.

3.2.3 Surge type glaciers

The large number of surge type glaciers uniquely defines the Karakoram mountain range (Shroder and Bishop, 2010; Hewitt, 2014). Surge type glaciers differ from advancing glaciers in that they undergo long periods of no movement (quiescent phase) and shorter periods of surge (Cuffey and Paterson, 2010). During a surge, a large volume of ice is transferred from the upper portion of the glacier (reservoir area) to the lower portion (receiving area). The velocity of a surging glacier is often 10 to 100 times greater than the velocity of the glacier when quiescent. Furthermore, the velocity is too great to be due to ice deformation alone; therefore, basal slip must be occurring as well (Cuffey and Paterson, 2010).

There is still not a complete understanding of surging mechanisms, but there are several observations made on surging glaciers which suggest surging mechanisms (Cuffey and Paterson, 2010). First observation is that meltwater moves much slower through the glacier during a surge than after a surge. This suggests a distributed drainage system during the surge leading to more meltwater available at the glacial bed. Once a tunnel system develops at the end of the surge, the meltwater drains more efficiently. This means that during a surge a glacier contains more basal water for lubrication. Another observation is that glaciers tend to surge in areas with soft sediment and in tectonically active mountain ranges undergoing rapid erosion. And finally, there needs to be a certain mass in the reservoir area of the glacier for the surge to commence.

Three types of instabilities are commonly discussed with respect to instabilities causing surge initiation and these are thermal instability, hydrological instability, and instability of a deformable bed (Cuffey and Paterson, 2010; Jiskoot, 2011). Thermal instability is typical for polythermal glaciers and happens when the ice in the reservoir area accumulates to a point where the basal pressure is increased and the basal ice reaches the melting point. Once some basal ice melts there is meltwater available to lubricate the glacial bed and to initiate the surge.

A hydrological trigger occurs when the tunnels of the drainage system of a glacier collapse (Cuffey and Paterson, 2010). After such a collapse, water drains the cavities leading to decrease flow in the tunnels and consequently collapse of the tunnels, which is in effect a switch to a drainage system that does not drain water as quickly. Thus, the initiation of a surge and its abrupt end may be due to switching between these two drainage systems. Note that, hydrological triggers assume hard bed for the cavities to form, while most but not all surging glaciers are observed to be over soft beds.

Instabilities due to soft bed deformation require a thick layer of fine-grained till and a large amount of water stored subglacially (Jiskoot, 2011). An increase in water pressure and shear stress causes the destruction of the subglacial drainage system (Jiskoot, 2011). The subsequent elevated water pressure results in increase in sediment deformation and an increase in ice flow velocities. The thinning of the till layer due to the surge leads to decrease in the subsurface sediment mobility terminating the surge (Jiskoot, 2011).

Surge dynamics of Karakoram glaciers were studied by Quincey et al. (2011). The authors identified five glaciers in Pakistan. Surface velocities were derived through feature tracking of remote sensing images. Landsat TM and Landsat ETM+ images were used to generate the velocity fields of the three larger glaciers, while finer resolution PALSAR was employed for two smaller glaciers. The authors concluded that the surges of these glaciers are thermally and not hydrologically controlled, the evidence for which was the seasonality of surge commencements, as one surge was initiated in the late summer and another in the fall. Quincey et al. (2011) indicate that previous work had shown that hydrological surges are most often initiated in the winter and end in the summer when there is enough meltwater to re-establish the subglacial hydrological system.

Additional evidence used to justify thermal control was that the glaciers accelerated gradually after the surge started, with peak velocities being reached about two years later. The quiescent state was reached about two to three years after the peak, with the smaller glaciers advancing considerably. The two smaller glaciers were not heavily debris-covered and are glaciers that were not previously reported to have surged. However, additional research on surging glaciers in the neighboring Pamir Mountains, indicated that both hydrological and thermal controls are causing glacier surge initiation Lv et al. (2018). These conflicting findings indicate the need for more research on surge mechanics.

Geomorphic characteristics of surge type glaciers have been studied for different regions. A characteristic of surge type glaciers is that they are generally longer than non-surge glaciers in the same region (Jiskoot et al., 2000). Jiskoot et al. (2000) offered several explanations for that. For example, longer glaciers also mean that the glacier is larger which relates to larger glaciers being more likely to surge. Also, longer glaciers are affected by a larger stress gradient and thus there are more opportunities to develop a trigger zone for initiating a surge. And a third explanation is that longer glaciers are more prone to ice instability due to the greater production of fine-grained sedimentary rocks at the bed.

Barrand and Murray (2006) investigated a suite of geomorphic variables over a set of Karakoram glaciers and found that the median glacier area of surge type glaciers is close to two and a half larger than the median area of non-surge type glaciers (164 km^2 as compared to 68 km^2). Sevestre and Benn (2015), who analyzed a global set of glaciers, also found a statistically significant difference between the size of the area of surge type versus non-surge type glaciers collocated in the same geographic region. Pertaining to this study is their finding that the smallest difference in size between the two groups is actually in High Mountain Asia and the Caucasus. The size of glaciers being a control on surge type may be due to the larger catchment size and the subsequent larger amount of snow accumulation on such glaciers.

This study in particular, focuses on differentiating surge type versus non-surge type glaciers by the amount of surface irradiance received. Surface melt has been identified as an active control on glacier surges in other parts of the world (Dunse et al., 2015). Thus, the external forcing of surface irradiance and the affects of topography on surface irradiance are are important to investigate.

3.2.4 Effects of topography on glaciers

Topography has been related to different responses of glaciers to changes in Equilibrium Line Altitude (ELA). Pratt-Sitaula et al. (2011) analyzed the change in ELA for different climates for glaciers in two neighboring valleys in Nepal. The glaciers were reconstructed through a cellular automata model to their simulated extent for the early Holocene and late-glacial periods. Climate was simulated from cooler and drier to warmer and wetter, as was at the transition to the Holocene. The results showed that advance of the glacier at the higher elevation, but a retreat of the lower-laying glacier. The authors linked glacier response to changes in climate to differences in hypsometry. The study had ensured that the aspects of the two valleys where the glaciers are located are the same. However, other topographic parameters such as relief and shielding were not considered.

Yu et al. (2013) investigated the mass balance variation between 2005-2008 and 2004-2008 of two glaciers located on north-facing and south-facing slopes, respectively, in the

West Nyenchen Tanglha mountain range, Tibetan Plateau. It was found that the glacier on the north slope experienced larger negative balance for all years except the last one. Time series of precipitation and temperature from stations located on the south and north slopes of the West Nyenchen Tanglha mountain range showed that atmospheric temperature increase is larger on the north slopes, while total precipitation is larger on the south slopes. The authors suggest that the different mass balance of the two glaciers may be related to topography such as orientation, area-altitude distribution of the ice, and different elevation of the accumulation area of the ice.

The effects of the topography on glacier mass balance in the Himalayas have also been demonstrated by Wagnon et al. (2007) who surveyed the two main flows and a tributary of the Chhota Shigri glacier, India for four consecutive years. The annual mass balance curves showed larger vertical gradient of mass balance in the higher portion of the ablation area than for the lower portion, which means that smaller altitudinal change in the higher portion of the glacier results in larger change in mass balance. This was explained as the effect of the shading from the steep valley walls in the glacier tongue. Additionally, (Wagnon et al., 2007) demonstrated that there was a difference in vertical mass balance gradient for glaciated areas that are at the same elevation but at different orientation explained by the different amounts of solar radiation received according to terrain azimuth.

3.3 Solar radiation modeling

Solar radiation is the largest external energy source governing Earth systems and surface processes (Clauser, 2006; Ugwu and Ugwuanyi, 2011; Slater, 2016). Current research shows that the net absorbed solar radiation by the Earth is 240 Wm^{-2}, which is countered by 239 Wm^{-2} of outgoing thermal radiation (Wild et al., 2013). The resulting thermal imbalance governs various changes in climate, hydrologic, and cryospheric systems (Wild and B., 2010; Stocker et al., 2013; Kargel et al., 2014). Monitoring and simulations of surface irradiance are essential for estimating and predicting changes in evapotranspiration, ablation, surface temperature, and microclimatic conditions which are all processes essential for understanding the spatiotemporal dynamics of Earth's systems. Moreover, surface irradiance fluxes govern a variety of landscape parameters and processes, but are especially important for the cryosphere. Surface irradiance is directly affecting glacier ablation, and is the largest positive term in the energy balance of glaciers (Cuffey and Paterson, 2010).

3.3.1 Components of surface irradiance

Surface irradiance is composed of direct irradiance, diffuse-skylight irradiance, and adjacent-terrain irradiance components, each having a decreasing contribution of energy in relation to the overall surface irradiance. Modeling the direct irradiance component over time requires orbital, atmospheric, and topographic information. The Earth-Sun orbital parameters account for daily and annual changes in solar geometry, and additional orbital parameters account for changes in eccentricity, axial tilt, and precession in accordance with the Milankovich cycles. Spectral-based implementation of atmospheric parameters and constituents that attenuate energy passing through the atmosphere is important because different atmospheric constituents attenuate solar energy in different portions of the electromagnetic spectrum (Muhammad Iqbal, 1983). Since most solar radiation models do not account for the spectral nature of atmospheric transmittance, the developed solar radiation model, STSRM, implements spectral-based parametrization of atmopsheric attenuation to account for these wavelength-dependent processes

Diffuse irradiance is hemispherically produced and known to be anisotropic in nature (Vartiainen, 2000; Ivanova, 2013). Topographic shielding reduces this irradiance component across the landscape in accordance with the complexity and the mesoscale relief of the topography, and there are various parameterizations of diffuse irradiance (e.g. Bird and Riordan, 1986).

The adjacent-terrain irradiance component can also be highly variable and depends upon land cover variations, the nature of the bidirectional reflectance distribution function (BRDF) at a particular location, the nature of the local and mesoscale topographical geometric relationships that govern the magnitude of irradiance, and the degree of atmospheric attenuation given the geometry of the topography. All of these relationships vary hemispherically around any one particular point on the landscape (Muhammad Iqbal, 1983). Given this complexity and relatively small contributions of energy, adjacent-terrain irradiance is not generally accounted for in surface irradiance distributions (e.g., ArcGIS). Implementations of the adjacent-terrain irradiance component require users to provide an albedo map of their study area or to use a single albedo value for the whole scene (e.g., QGIS). Therefore, this component of solar irradiance is currently not implemented in STSRM.

3.3.2 Review of solar radiation models

A brief review of solar radiation models follows. The limitations of these models are that they are either not GIS-based, or that their parameterizations are simplified and thus inappropriate to model topographic effects on glaciers. Solar radiation models are broadly classified as deterministic physics-based, semi-empirical, or empirical models (Ahmad and Tiwari, 2010; Katiyar and Pandey, 2013). Physics-based models parameterize the processes related to scattering, transmittance, absorption and refraction without using fitted parameters, while empirical models utilize equations that attempt to characterize relationships with empirically derived constants. Many models integrate a combination of physics and empirical equations, and such models could be classified as semi-empirical. Other solar radiation models utilized remote sensing observations and model solar radiation based on that. And yet another type of solar radiation modeling involves machine learning.

Essential in the modeling of short-wave surface irradiance is the atmospheric attenuation due to atmospheric constituents such as water vapor, aerosols, ozone, primary gases and other. Modeling of the extinction of solar electromagnetic radiation through the atmosphere ranges from complex radiative transfer models such as MODerate resolution atmospheric TRANsmission (MODTRAN) (Kniezys et al., 1996; Berk et al., 1999, 2014; Berk and Hawes, 2017), Discrete Anisotropic Radiative Transfer (DART) (Grau et al., 2013), and Community Radiative Transfer Model (CRTM) (Weng et al., 2005) to empirical formulations based on a coefficient such as the Linke turbidity factor, which is a broadband coefficient that accounts for atmopsheric attenuation due to scattering by aerosols and absorption of water vapor (Louche et al., 1986; Chaâbane et al., 2004).

An example of a solar radiation model that is a combination of a radiative transfer and empirical modeling is Simple Model for the Atmospheric Radiative Transfer of Sunshine (SMARTS2) (Gueymard, 1995) that uses temperature or pressure dependent extinction coefficients derived from spectroscopic studies or from MODTRAN2 (a version of MODTRAN provided to the authors of the SMARTS2 model), which is utilized in this study.

More recent modeling efforts of solar radiation include various machine learning approaches aimed at a better characterization of surface irradiance. For example, (Yan et al., 2016) coupled an artificial neural network to a longwave radiation topographic model to satellite images acquired from MODIS. All possible topographic effects in a rugged terrain are considered, and the study demonstrated that topographic effects on longwave radiation cannot be ignored for grid cells less than 5 km. This is an important finding that confirms that need for better representation of topography in solar radiation models, even though the focus of our study is shortwave radiation.

Piri and Kisi (2015) offered several empirical models based on artificial neural networks. A limitation to these is that they are trained on data from specific solar radiation weather stations and are thus not necessarily applicable to other areas. To address this limitation, regression models on a global scale are good studies creating unique solar radiation datasets (Vindel and Polo, 2014; Vindel et al., 2015), but not operational for simulation of surface irradiance over a specific study area.

A suite of solar radiation models that utilize satellite remote sensing data has also been developed. Carmona et al. (2015) developed a method for estimating instantaneous, daily, and daytime net radiation from Landsat satellite data on clear-sky days. This approach however assumes no topographic effects are altering the images and thus is not as accurate in areas with high relief. Zhang et al. (2015) analyzed the estimates of short-wave radiation from four satellite products, however, the spatial resolution of these is between one degree and 280 km which is much greater than what a DEM could resolve.

A sun position calculator is provided by Seong (2015) for the purposes of correcting satellite images for terrain effects. The model utilizes geodetic latitude and provides solar position for each pixel within the image. This model falls short of being a solar radiation model but is useful for satellite image correction. Another study provides simulations of satellite data utilizing radiative transfer model and terrain conditions such as surface cover (Meharrar and Bachari, 2014), which is important for comparing simulated to acquired satellite data and thus for studying the quality of satellite image correction.

3.3.2.1 GIS-based solar radiation models

There also exist several GIS-based solar radiation models, such as Solar Analyst implemented in the ArcGIS software package (Fu, 2000; Fu and Rich, 2002), r.sun implemented in the QGIS software package (Hofierka and Šurí, 2002), spatially distributed radiation (SRAD) model (McKenney, 1999), and Solei-32 (Mészároš et al., 2002). Previous work evaluated these models against measured surface irradiance in rugged terrain (Ruiz-Arias et al., 2009). The study determined that r.sun and Solei-32 were able to reproduce the surface irradiance distribution well, while Solar Analyst and SRAD were not successful in reproducing the spatial distribution of surface irradiance.

The two most popular GIS-based solar radiation models are Solar Analyst (ArcGIS) and r.sun (QGIS). Although they can be easily utilized in a GIS-environment, they are not spectral based, which means that they do not account for variations in atmospheric attenuation as a function of wavelength. In addition, these two GIS-based solar radiation models cannot be used to accurately hindcast or predict variations over long periods of time, as changes in orbital parameters govern the solar geometry on geologic scale (Berger, 1978b,a; Berger and Loutre, 1991). Thus, these approximations do not allow for usage of the model centuries in the past or in the future, which is a requirement for landscape evolution models.

Although these two models attempt to address multiscale topographic effects, they also utilize approximations to reduce computational time. Thus, a distinction between those models and the ones that account for multiscale topographic effects and spectral characterization of atmospheric parameters is warranted.

Atmospheric attenuation for the Spatial Analyst implementation in ArcGIS is handled through a user-provided transmissivity value (Fu, 2000; Fu and Rich, 2002; ArcGIS, 2016). The provided value is the ratio of the solar energy at the top of the atmosphere to the solar energy received at the surface, which is a limitation of the software, as users either have to estimate or utilize external models for identifying the appropriate atmospheric transmissivity value for given atmospheric conditions. The r.sun model implemented in QGIS (Hofierka and Šurí, 2002) similarly requires a user-specified parameter of atmospheric attenuation. Unlike Spatial Analyst, r.sun requires the Linke turbidity coefficient, which has physical basis and may be calculated through an equation accounting for multiple atmospheric conditions (Louche et al., 1986). Both of these models, though, are limited by the requirement of a user-specified parameter describing the atmospheric conditions.

The simplicity of the GIS-based solar radiation models implemented in ArcGIS and QGIS makes them inappropriate to use in a high-relief terrain such as the Karakoram mountain range. At the same time, the radiative transfer models that account for physics-based processes are not available to use within a GIS software and thus are not available to us. Thus, this study focused on developing GIS-based solar radiation model that provides spectral characterization of atmospheric transmissivity and accounts for topographic effect, while still being available within a GIS-based environment.

4. METHODS *

4.1 Solar radiation model parametrization

The development of a new GIS-based spectral-topographic solar radiation model was necessary so that various topographic effects on surface solar irradiance are modeled (Figure 4.1). The solar radiation model accounts for variations in topography because atmospheric properties, such as water content, change as a function of elevation. Multiscale topographic effects are also considered because the surrounding terrain may block the direct solar radiation or may obscure a fraction of the sky affecting the diffuse irradiance. Additionally, a solar radiation model should be spectral in nature to properly account for wavelength-dependent matter-energy interactions.

Orbital variations are also accounted for in this model envisioning it as a component in landscape evolution models. Furthermore, by utilizing High Performance Computing (HPC) technologies, the computational efficiency of the model is increased to allow for spatiotemporal simulations of surface irradiance over large geographic areas for long periods of time, and with a small time step. The new solar radiation model is validated against measured station solar irradiance and also the new model is compared to the solar radiation models implemented in ArcGIS and QGIS.

4.1.1 Orbital parameters

Variations in Sun-Earth orbital parameters control the amount of solar energy reaching the top of the Earth's atmosphere. These orbital forcings are accounted for through modeling eccentricity (e), obliquity (ϵ), as well as a parameter related to Earth's precession - the

*Portions of section 4.1 are reused with permission from the publication: Bishop, M. P., I. D. Dobreva and C. Houser (2015). Geospatial Science and Technology for Understanding the Complexities of the Critical Zone In J. R. Giardino and C. Houser (Eds.), *Principles and Dynamics of the Critical Zone* (pp. 523-561), Copyright 2015 Elsevier.

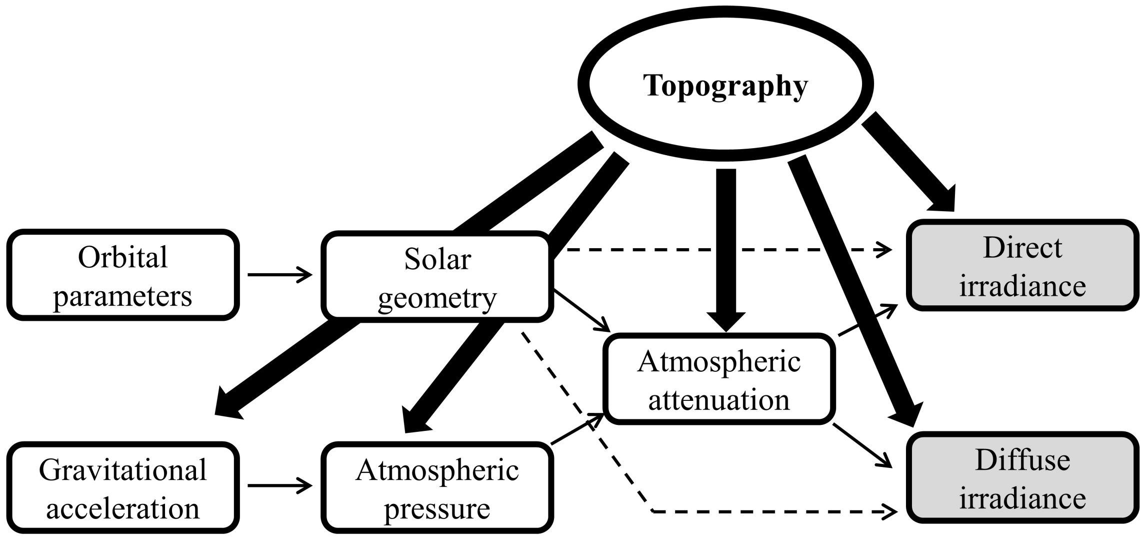

Figure 4.1: Solar radiation model components accounting for topography.

longitude of perihelion (ϖ) measured from the moving vernal equinox of a date (Berger, 1978b,a).

Berger (1978b) provided the trigonometric expansion of ϵ, $e \sin \varpi$, and e, along with the amplitudes, rates, and phases of the expansion. This so-called BER78 solution is valid for reproducing the orbital parameters for the last 1.5 million years, and it is used in this model. An alternative BER90 solution could be used over even longer time-scales (Berger and Loutre, 1991). Modeling orbital variations accounts for Milankovitch cycles, and thus STSRM is appropriate to use for paleoclimate modeling.

The obliquity, eccentricity, and longitude of perihelion are calculated for each year. These parameters are used to calculate the longitude (λ_{MS0}) of the mean Sun at the vernal equinox through the following approximation (Berger, 1978b):

$$\begin{aligned}\lambda_{MS0} = \lambda_{TS} - 2[&(0.5e + 0.125e^3)(1 + \beta_\lambda)\sin(\varpi + \pi) \\ &- 0.25e^2(0.5 + \beta_\lambda)\sin(2(\varpi + \pi)) \\ &+ 0.125e^3(1/3 + \beta_\lambda)\sin(3(\varpi + \pi))]\end{aligned} \tag{4.1}$$

where λ_{TS} is the longitude of the true Sun, which is 0 at the vernal equinox. β_λ is calculated as:

$$\beta_\lambda = (1 - e^2)^{0.5} \tag{4.2}$$

The longitude of the mean Sun at any other day is calculated by adding an incremental longitude:

$$\lambda_{MS} = \lambda_{MS0} + (D_c - 80) \times 2\pi/365 \tag{4.3}$$

where D_c is the day of year, and 80 is the day of year at the vernal equinox for non-leap years. Using this formula, small error is introduced for leap years. The longitude of the true Sun is then calculated as (Berger, 1978b):

$$\begin{aligned}\lambda_{TS} = \lambda_{MS} &+ (2e - 0.25e^3)\sin(M_a) + 1.25e^2\sin(2M_a) \\ &+ (13/12)e^3\sin(3M_a)\end{aligned} \tag{4.4}$$

where M_a is the mean anomaly of the Sun and is calculated by the following formula:

$$M_a = \lambda_{MS} - (\varpi + \pi) \tag{4.5}$$

The true anomaly (v_A) of the Sun is calculated as:

$$v_A = \lambda_{TS} - (\varpi + \pi) \tag{4.6}$$

and is used to calculate the distance (D) between the Sun and the Earth for a particular day:

$$D = D_m(1 - e^2)/(1 + e\cos(v_A)) \tag{4.7}$$

where D_m is the mean Sun-Earth distance; in this study a value of 149597870.7 AU is used (NASA, 2018).

The eccentricity correction factor, which is used for calculating direct irradiance, is calculated from D:

$$F_{ec} = \left(\frac{a_o}{D}\right)^2 \tag{4.8}$$

where a_o is the semi-major axis of the orbit, and its value is set to 150×10^6

4.1.2 Solar Geometry

Computing the solar geometry requires calculations of solar declination (δ) and solar hour angle (H_{TS}) for a particular time. The solar declination is computed using the following formula:

$$\delta = \arcsin(\sin(\epsilon)\sin(\lambda_{TS})) \tag{4.9}$$

Computing the solar hour angle requires correction of the mean solar time (T_{MS}) to true solar time (T_{TS}) through the Equation of Time (ET):

$$T_{TS} = T_{MS} + ET; \tag{4.10}$$

where T_{MS} is calculated from Greenwich Mean Time (GMT) and the longitude of a location (λ_l) as:

$$T_{MS} = GMT + (\lambda_l/15); \tag{4.11}$$

The hour angle is then calculated as:

$$H_{TS} = 15T_{TS} \tag{4.12}$$

where 15 is a factor in the conversion between hours and degrees.

Civil time is related to the motion of Earth along its orbit and to Earth's rotation. The following discussion is from Smart (1970). When the Sun is on the meridian of a location, it is apparent solar noon there, and an apparent solar day is concluded with the next passing of the Sun over the meridian. Time measured with respect to the apparent motion of the Sun relative to Earth is called Sidereal Time. However, relative to Earth, the Sun does not move uniformly. For time keeping, therefore, a mean Sun which appears to move uniformly along the celestial equator such that it completes a revolution at the same time as the true Sun is assumed. Additionally, to account for variations in Earth's rotation, the mean Sun moves at a rate such that, at each instant, it is directly proportional to the Earth's angular velocity. The difference between the right ascension (α_{MS}) of the mean Sun and the right ascension (α_{TS}) of the true Sun is called the Equation of Time (ET) and is defined as:

$$ET = \alpha_{MS} - \alpha_{TS} \tag{4.13}$$

Equivalently, ET could also be defined as the difference between the hour angle (H_{TS}) of the true Sun and the hour angle (H_{MS}) of the mean Sun:

$$ET = H_{TS} - H_{MS} \tag{4.14}$$

Both right ascension and hour angle are measured with respect to the vernal equinox. The true vernal equinox changes periodically due to precession and nutation, and the moving mean equinox is defined as the position of the true vernal equinox if nutation is ignored. Nutation causes small oscillatory motion of the equinox, with a period of about 18 years, and there is up to a 1.2 second difference between the right ascension with respect to the true equinox and the right ascension with respect to the moving mean equinox. In the following equations, right ascension with respect to the moving mean equinox is assumed.

The hour angle (H_{GMS}) of the mean sun at the Greenwich meridian plus a 12-hour offset is defined as Universal Time (UT), or Greenwich Mean Time (GMT):

$$UT \equiv GMT = 12 + H_{GMS} \tag{4.15}$$

Since UT is defined by the rotation of Earth, it is not uniform. Ephemeris Time, however, is defined by the gravitational dynamics of the solar system and is uniform.

In equation (4.13), α_{MS} can be calculated with respect to Universal Time, but α_{TS} can only be calculated in advance with respect to Ephemeris Time, because we are unable to calculate the variations in Earth's rotation. The Equation of Ephemeris Time (ET_E) is calculated by instead using the right ascension (α_{FMS}) of a fictitious mean Sun that moves along the equator with the Sun's mean angular velocity:

$$ET_E = \alpha_{FMS} - \alpha_{TS} = \lambda_{MS} - \alpha_{TS} \tag{4.16}$$

The right ascension of the fictitious mean Sun also equals the Sun's mean longitude, which is the Sun's celestial longitude if Earth's orbit is assumed circular and the Sun is assumed to be moving at a uniform motion.

Considering that α_{FMS} equals the Sun's mean longitude, the Equation of Ephemeris

Time (4.16) may be written as:

$$ET_E = (\lambda_{TS} - \alpha_{TS}) - (\lambda_{TS} - \lambda_{MS}) \tag{4.17}$$

The first part of the equation is called the 'reduction of the equator' and is a function of the obliquity of the ecliptic. It can be expressed as a series in terms of the true Sun's longitude:

$$\lambda_{TS} - \alpha_{TS} = y_\lambda \sin(2\lambda_{TS}) - \frac{1}{2}y_\lambda^2 \sin(4\lambda_{TS}) + \frac{1}{3}y_\lambda^3 \sin(6\lambda_{TS}) \tag{4.18}$$

In the above equation y_λ is defined as:

$$y_\lambda \equiv \tan^2 \frac{\epsilon}{2} \tag{4.19}$$

The second part of the equation may be expressed in terms of the Sun's true (v_A) and mean (M_A) anomalies and is known as the 'equation of center':

$$\lambda_{TS} - \lambda_{MS} = v_A - M_A \tag{4.20}$$

and thus equation (4.17) becomes:

$$\mathrm{ET_E} = -(\alpha_{TS} - \lambda_{TS}) - (v_A - M_A) \tag{4.21}$$

The 'equation of center' depends on the orbital eccentricity. It can be expressed as a series in terms of the Sun's mean anomaly:

$$v_A - M_A \equiv \lambda_{TS} - \lambda_{MS} = 2e \sin M_A + \frac{5}{4}e^2 \sin(2M_A) \tag{4.22}$$

Substituting (4.18) and (4.22) into the Equation of Ephemeris Time (4.21) and approximating $\sin(4\lambda_{TS}) = \sin(4\lambda_{MS})$ leads to:

$$\begin{aligned} \mathrm{ET_E} =& y_\lambda \sin(2\lambda_{MS}) - 2e \sin M_A + 4ey_\lambda \sin M_A \cos(2\lambda_{MS}) \\ & - \frac{1}{2} y_\lambda^2 \sin(4\lambda_{MS}) - \frac{5}{4} e^2 \sin(2M_A) \end{aligned} \tag{4.23}$$

The Equation of Ephemeris Time (4.23) is used in this study instead of the Equation of Time as the difference between the two is small.

The cosine of the geocentric solar zenith angle (θ_s^g) is calculated as (Jacobson, 2005):

$$\cos\theta_s^g = \sin\varphi \sin\delta + \cos\varphi \cos\delta \cos H_{ts} \tag{4.24}$$

where φ is the geodetic latitude of the location. The geocentric solar zenith angle is calculated from the center of the Earth; however, parallax correction ($\delta\theta_p$) is required to compute the apparent solar zenith angle (θ_s^a) from the Earth's surface:

$$\theta_s^a = \theta_s^g + \delta\theta_p \tag{4.25}$$

The parallax correction is calculated as a function of Earth's radius (R, equation 4.37), height (h) relative to the ellipsoid, and distance from the Sun (D) as (DMA, 1992; Blanco-Muriel et al., 2001):

$$\delta\theta_p = \frac{R(\varphi) + h}{D} \sin(\theta_s) \tag{4.26}$$

and added to the geocentric solar zenith angle:

$$\theta_s^a = \theta_s^g + \delta\theta_p \tag{4.27}$$

Atmospheric refraction correction ($\delta\theta_r$) is a function of apparent (θ_s^a) solar zenith angle and temperature in units of °C, and is provided in The Astronomical Almanac (2013).

$$\delta\theta_r = \begin{cases} \dfrac{0.00452P\tan\theta_s^a}{273+T} = \dfrac{0.00452P}{(273+T)\tan\alpha_s^a}, & \text{if } \theta_s < 75 \text{ degrees} \\ \\ \dfrac{P(0.1594+0.0196\alpha_s^a+0.00002(\alpha_s^a)^2)}{(273+T)(1+0.505\alpha_s^a+0.0845(\alpha_s^a)^2)}, & \text{if } \theta_s \geq 75 \text{ degrees} \end{cases} \quad (4.28)$$

where $\alpha_s^a = 90 - \theta_s^a$ is the solar elevation angle. The atmospheric refraction correction is subtracted from the apparent solar zenith angle:

$$\theta_s = \theta_s^a - \delta\theta_r \quad (4.29)$$

The solar azimuth angle (ϕ_s^{nc}) is calculated as:

$$\phi_s^{nc} = \pi + \text{atan2}(Y_s, X_s) \quad (4.30)$$

where the sine (Y_s) and the cosine (X_s) components are computed from the following equations:

$$Y_s = (-\cos\delta\sin H_{TS})/\cos\alpha_s; \quad (4.31)$$

and

$$X_s = (\sin\alpha_s\sin\varphi - \sin\delta)/(\cos\alpha_s\cos\varphi); \quad (4.32)$$

Solar azimuth angle (ϕ_s^g) is corrected (DMA, 1992) for grid convergence where the grid north differs from true north. Grid convergence ($\delta\phi_{gc}$) is a function of the latitude and the longitude of a location and the longitude of the central meridian of the projection used (λ_{cm}):

$$\delta\phi_{gc} = -\sin(\varphi)tan(\lambda_l - \lambda_{cm}) \quad (4.33)$$

True azimuth is calculated by subtracting the grid convergence:

$$\phi_s = \phi_s^{nc} - \delta\phi_{gc} \tag{4.34}$$

The grid convergence in the Northern Hemisphere is negative to the east of the central meridian and positive to the west of the central meridian; it is the opposite in the Southern Hemisphere.

The local ellipsoidal radius (R) is a parameter used in the modeling of gravitational acceleration, which in tern is necessary for calculating atmospheric pressure. R is formulated in terms of geocentric latitude (φ_{gc}) as (DMA, 1987):

$$R(\varphi_{gc}) = \frac{a\sqrt{1 - e_{re}^2}}{\sqrt{1 - e_{re}^2 \cos^2 \varphi_{gc}}} \tag{4.35}$$

where a is the semi-major axis [m] of the reference ellipsoid and e_{re} is the first numerical eccentricity of the reference ellipsoid (see Table 4.1). Conversion between geocentric and geodetic (φ) latitude is performed through the following equation:

$$\varphi_{gc} = \tan^{-1}[(1 - e_{re}^2) \tan \varphi] \tag{4.36}$$

In terms of geodetic latitude, R is expressed as:

$$R(\varphi) = \frac{a\sqrt{1 - e_{re}^2}}{\sqrt{1 - e_{re}^2 \cos^2(\tan^{-1}[(1 - e_{re}^2) \tan \varphi])}} \tag{4.37}$$

The ellipsoidal radius may also be approximated as (Hofmann-Wellenhof and Moritz, 2006) :

$$R(\varphi) = a(1 - f \sin^2 \varphi) \tag{4.38}$$

where f is the ellipsoidal flattening of the reference ellipsoid (see Table 4.1).

Table 4.1: Derived ellipsoid constants. In this table, a and b are the semi-major and semi-minor axes af the ellipsoid, Ω is the Earth's angular velocity $[\mathrm{rad\,s^{-1}}]$, G is the universal gravitational constant and M_e is Earth's mass $[\mathrm{kg}]$ (NIMA 2000 and Hofmann-Wellenhof and Moritz 2006).

Constant	Formula	Units
Flattening	$f = \frac{a-b}{a}$	dimensionless
Liner eccentricity	$E = \sqrt{a^2 - b^2}$	m
First numerical eccentricity	$e_{re} = \frac{E}{a}$	dimensionless
Second numerical eccentricity	$e'_{re} = \frac{E}{b}$	dimensionless
	$m_a = \frac{\Omega^2 a^2 b}{GM_e}$	dimensionless
Ellipsoid gravity at the equator	$g_e = \frac{GM_e}{ab}(1 - \frac{3}{2}m - \frac{3}{14}e'^2_{re}m)$	$\mathrm{m\,s^{-2}}$
Ellipsoid gravity at the poles	$g_p = \frac{GM_e}{a^2}(1 + m + \frac{3}{7}e'^2_{re}m)$	$\mathrm{m\,s^{-2}}$
	$k = \frac{bg_p}{ag_e} - 1$	dimensionless
	$f_2 = f + \frac{5}{2}m + \frac{1}{2}f^2 - \frac{26}{7}fm + \frac{15}{4}m^2$	dimensionless
	$f_4 = -\frac{1}{2}f^2 + \frac{5}{2}fm$	dimensionless
Gravitational flattening	$f^* = \frac{g_p - g_e}{g_e} = f_2 + f_4$	dimensionless

Gravity is modeled in terms of height (h) above the reference ellipsoid and requires the conversion of height above sea level (H) to h through the height of the geoid (N):

$$H = h - N \tag{4.39}$$

The theoretical gravity (g_h) in units of $\mathrm{m\,s^{-2}}$ above or below the ellipsoid is defined as the total normal gravity vector's component that is colinear with the geodetic normal line and that has a positive direction downward. At small geodetic height (up to 7000 m above the ellipsoidal surface), an approximation of theoretical gravity based on Taylor series expansion (NIMA, 2000) could be used.

The theoretical gravity should not (NIMA, 2000) be approximated through series expansion at moderate and high geodetic height. Instead, a close approximation of g_h is achieved by expressing the theoretical gravity vector ($\vec{g_E}$) in the ellipsoidal coordinate system and equating g_h to the vector's magnitude. The so-called *close approximation* of g_h differs less than one $\mu\mathrm{gal}$ ($10^{-8}\ \mathrm{m\,s^{-2}}$) for geodetic heights up to $20,000$ m, and it is used for calculating gravity in STSRM.

The theoretical ellipsoid gravity (g_t) in units of $\mathrm{m\,s^{-2}}$ is a function of geodetic latitude and is formulated as a closed-form expression by Somigliana 1930 (in NIMA, 2000; Hofmann-Wellenhof and Moritz, 2006). It is expressed in terms of the semi-major and semi-minor (b) axes of the ellipsoid in units of meters, Earth's mass (M_e) in units of kg, Earth's angular velocity (Ω) in units of $\mathrm{rad\,s^{-1}}$, and the universal gravitational constant ($G = 6.6270 \times 10^{-11}\ \mathrm{m^3\,kg^{-1}\,s^{-2}}$). Additionally, the formulation employs the linear eccentricity (E), the first (e_{re}) and second (e'_{re}) numerical eccentricity, the theoretical ellipsoid gravity at the equator (g_e) and at the poles (g_p), and the numerical abbreviations m_a and k (see Table 4.1).

Note that the theoretical ellipsoid gravity is also called normal gravity and is the magnitude of the potential of the normal gravity field. The actual gravity field is the normal gravity field plus the anomalous gravity field. Also note that ellipsoid gravity is usually notated with γ while g is reserved for gravity measured at the physical surface.

Two forms of the closed formula of Somigliana (1930) are

$$g(\varphi) = \frac{a g_e \cos^2\varphi + b g_p \sin^2\varphi}{\sqrt{a^2\cos^2\varphi + b^2\sin^2\varphi}} \quad [\mathrm{m\,s^{-2}}] \tag{4.40a}$$

and

$$g(\varphi) = g_e \frac{1 + k\sin^2\varphi}{\sqrt{1 - e_{re}^2\sin^2\varphi}} \quad [\mathrm{m\,s^{-2}}] \tag{4.40b}$$

Equation (4.40b) is preferred by the developers of the World Geodetic System 1984 Ellipsoid as it is more convenient computationally and contains the theoretical gravity at the equator as a first term (DMA, 1991). The normal gravity formulation could also be approximated as a second-order series expansion (Hofmann-Wellenhof and Moritz, 2006; Moritz, 1988) in terms of geodetic latitude, theoretical gravity at the equator, the ellipsoidal and gravitational flattening (f^*), and the numerical abbreviation m_a (see Table 4.1):

$$g_t(\varphi) = g_e(1 + f^* \sin^2 \varphi - \frac{1}{4} f_4 \sin^2 \varphi) \quad [\mathrm{m\,s^{-2}}] \tag{4.41}$$

The theoretical gravity (g_h) in units of $\mathrm{m\,s^{-2}}$ above or bellow the ellipsoid is defined as the total normal gravity vector's component that is collinear with the geodetic normal line and that has a positive direction downward.

At small geodetic height (up to 7000 m above the ellipsoidal surface), an approximation of theoretical gravity based on Taylor series expansion (NIMA, 2000) is formulated as:

$$g_h(\varphi, h) = g_t \left[1 - \frac{2}{a}\left(1 + f + m_a - 2f \sin^2 \varphi\right) h + \frac{3}{a^2} h^2\right] \quad [\mathrm{m\,s^{-2}}] \tag{4.42}$$

where h is height relative to the ellipsoid in units of meters (eq. 4.39) .

The theoretical gravity should not (NIMA, 2000) be approximated through series expansion at moderate and high geodetic height. A close approximation of g_h is achieved by expressing the theoretical gravity vector ($\vec{g_E}$) in the ellipsoidal (u, β and λ_l) coordinate system and equating g_h to the vector's magnitude.

Let P be a point that is h meters above or below the ellipsoid. The curvature (R_n) in the prime vertical is

$$R_n = \frac{a}{\left(1 - e_{re}^2 \sin^2 \varphi\right)^{1/2}} \tag{4.43}$$

and the rectangular coordinates of P are computed from the point's geodetic coordinates and curvature in the prime vertical as:

$$x = (R_n + h)\cos\varphi\cos\lambda_l \tag{4.44a}$$

$$y = (R_n + h)\cos\varphi\sin\lambda_l \tag{4.44b}$$

$$z = \left(\left(\frac{b^2}{a^2}\right)R_n + h\right)\sin\varphi \tag{4.44c}$$

where λ_l is geodetic longitude.

The position of P is then expressed in terms of two of its ellipsoidal coordinates (u and β):

$$u = \left[\frac{1}{2}\left(x^2 + y^2 + z^2 - E^2\right)\left\{1 + \sqrt{1 + \frac{4E^2z^2}{\left(x^2 + y^2 + z^2 - E^2\right)^2}}\right\}\right]^{1/2} \tag{4.45a}$$

$$\beta = \arctan\left(\frac{z\sqrt{(u^2 + E^2)}}{u\sqrt{x^2 + y^2}}\right) \tag{4.45b}$$

The ellipsoidal coordinates of P are the semi-minor axis (u) of the ellipsoid of revolution that passes through P, the reduced latitude (β), and the geodetic longitude (λ_l). Additionally, the following numerical abbreviations are computed:

$$w = \sqrt{\frac{u^2 + E^2\sin^2\beta}{u^2 + E^2}} \tag{4.46a}$$

$$q = \frac{1}{2}\left[\left(1 + 3\frac{u^2}{E^2}\right)\arctan\left(\frac{E}{u}\right) - 3\frac{u}{E}\right] \tag{4.46b}$$

$$q_0 = \frac{1}{2}\left[\left(1 + 3\frac{b^2}{E^2}\right)\arctan\left(\frac{E}{b}\right) - 3\frac{b}{E}\right] \tag{4.46c}$$

$$q' = 3\left[1 + \frac{u^2}{E^2}\right]\left[1 - \frac{u}{E}\arctan\left(\frac{E}{u}\right)\right] - 1 \tag{4.46d}$$

The ellipsoidal components of the theoretical gravity vector $\vec{g}_{total}$ are then computed as:

$$g_u(u,\beta) = -\frac{1}{w}\left[\frac{GM}{u^2+E^2} + \frac{\Omega^2 a^2 E}{u^2+E^2}\frac{q'}{q_0}\left(\frac{1}{2}\sin^2\beta - \frac{1}{6}\right)\right] + \frac{1}{w}\Omega^2 u\cos^2\beta \tag{4.47a}$$

$$g_\beta(u,\beta) = \frac{1}{w}\frac{\Omega^2 a^2}{\sqrt{u^2+E^2}}\frac{q}{q_0}\sin\beta\cos\beta - \frac{1}{w}\Omega^2\sqrt{u^2+E^2}\sin\beta\cos\beta \tag{4.47b}$$

$$g_\lambda = 0 \tag{4.47c}$$

At P the angular separation (ε_{as}) between the normal gravity vector ($\vec{g}_{total}$) and the component (g_h) that is collinear to the geodetic normal could be ignored. Then, g_h at P is approximated as:

$$g_h(\varphi,\lambda_l,h) \cong |\vec{g}_{total}| = \sqrt{g_u^2 + g_\beta^2 + g_{\lambda_l}^2} \quad [\mathrm{m\,s^{-2}}] \tag{4.48}$$

Atmospheric pressure at any height above a reference height can be expressed in terms of the scale height (H_s) of the atmosphere in units of km. The scale height of the atmosphere is the height from a reference height at which the pressure decreases to $1/e$ of the pressure at the reference height. The scale height is expressed as (Jacobson, 2005):

$$H_s = \frac{k_B T_v}{\bar{M} g} \tag{4.49}$$

where T_v is the virtual temperature(in K), gravity is in units of $\mathrm{m\,s^{-2}}$, $k_B = 1.380658 \times 10^{-23}\ \mathrm{kg\,m^2\,s^{-2}\,K^{-1}\,molec.^{-1}}$ is the Stephan Boltzman constant, and $\bar{M} = 4.8096 \times 10^{-26}\ \mathrm{kg}$ is the average mass of one air molecule. Virtual temperature can be expressed in terms of temperature and specific humidity (q_v):

$$T_v = T(1 + 0.608 q_v) \tag{4.50}$$

Table 4.2: MODTRAN atmospheric profile for temperature and water mixing ratio.

Atmospheric profile	Option Number
Tropical	1
Midlatitude Summer	2
Midlatitude Winter	3
Subarctic Summer	4
Subarctic Winter	5
US Standard	6

where specific humidity (in $\mathrm{kg\,kg^{-1}}$) can be calculated from the mass mixing ratio (w_v in $\mathrm{kg\,kg^{-1}}$) of water vapor as:

$$q_v = \frac{w_v}{1 + w_v} \tag{4.51}$$

The mass mixing ration of water vapor may be acquired from a Standard Atmosphere profile.

Using the scale height of the atmosphere, pressure as a function of altitude can be calculated as:

$$p_a = p_{a,ref} e^{-(H - H_{ref})/H_s} \tag{4.52}$$

where $p_{a,ref}$ is the air pressure [hPa] at the reference altitude H_{ref} and H is the altitude (in km) at which p_a is calculated. This equation allows the atmosphere to be separated into different layers, where the top of one layer is the reference height of the next layer. Alternatively, the reference height could be set at sea level. In this study, the reference height is set at sea level and only one atmospheric layer is considered.

4.1.3 Atmospheric attenuation

Different atmospheric models for temperature- and water-mixing ratio profiles, for the effective path length of ozone, and for aerosol models are provided as they are available from MODTRAN (Tables 4.2, 4.3, and 4.4).

Table 4.3: Atmospheric model for the effective path length of ozone.

Atmospheric model	Option Number
USSA (U.S. Standard Atmosphere), 45°N	1
MLS (Mid Latitude Summer), 45°N	2
MLW (Mid Latitude Winter), 45°N	3
SAS (Sub Arctic Summer), 60°N	4
SAW (Sub Arctic Winter), 60°N	5
TRL (Tropical), 15°N	6
STS (Sub Tropical Summer), 30°N	7
STW (Sub Tropical Winter), 30°N	8
AS (Arctic Summer), 75°N	9
AW (Arctic Winter), 75°N	10

Table 4.4: Diffuse aerosol model options.

Model	Option Number
Continental aerosol model	1
Urban aerosol model	2
Maritime aerosol model	3

Traveling through the atmosphere, solar energy is attenuated by the scattering and absorption by atmospheric constituents. STSRM utilizes the atmospheric attenuation parameterizations of the SMARTS 2 model (Gueymard, 1995) for Rayleigh, ozone, and water vapor attenuation. Mie scattering due to aerosols is modelled through the Ångstrøm turbidity formula.

Atmospheric extinction is wavelength (λ [μm]) dependent, and the beam irradiance ($E_b(\lambda)$ [W m$^{-2}\mu$m^{-1}]) received at a surface normal to the sun is (Gueymard, 1995):

$$E_b^n(\lambda) = E^0(\lambda)\mathbf{T}^{\downarrow}(\lambda) \tag{4.53}$$

where $E^0(\lambda)$ is the top of the atmosphere irradiance corrected for Sun-Earth distance and

$\mathbf{T}^{\downarrow}(\lambda)$ is the total transmissivity, a dimensionless parameter, which is the product of the transmissivity coefficients from extinction processes.

The transmissivity due to a single extinction process i can be expressed as:

$$\mathbf{T}_i^{\downarrow}(\lambda) = \exp(-m_i \tau_i(\lambda)) \tag{4.54}$$

where m_i is the optical mass and $\tau_i(\lambda)$ is the optical thickness of an extinction process. A parametrization of the optical mass is provided by Gueymard (2005):

$$m_i = (\cos(\theta_s) + a_{i1}(\theta_{s,deg})^{a_{i2}}(a_{i3} - \theta_{s,deg})^{a_{i4}})^{-1} \tag{4.55}$$

where $\theta_{s,deg}$ indicates that the solar zenith angle is expressed in degrees. The coefficients (a) are provided in table 4.5.

Table 4.5: Coefficients for optical masses (Gueymard, 2005)

Extinction process	a_{i1}	a_{i2}	a_{i3}	a_{i4}	m_i at $\theta_{s,deg} = 90\,\mathrm{deg}$
Rayleigh	4.5665×10^{-1}	0.07	96.4836	-1.6970	38.136
Ozone	2.6845×10^{2}	0.5	115.420	-3.2922	16.601
Nitrogen dioxide	6.0230×10^{2}	0.5	117.960	-3.4536	17.331
Mixed gases	4.5665×10^{-1}	0.07	96.4836	-1.6970	38.136
Water vapor	3.1141×10^{-2}	0.1	92.4710	-1.3814	71.443
Aerosols	3.1141×10^{-2}	0.1	92.4710	-1.3814	71.443

4.1.3.1 Rayleigh attenuation

Rayleigh transmissivity ($\mathbf{T_r}(\lambda)$) can be expressed as (Gueymard, 2005):

$$\mathbf{T_r}(\lambda) = \exp(-\mathbf{m_r}\tau_{\mathbf{r}}(\lambda)) = \exp(-\mathbf{m_r}\frac{\mathbf{P_c}}{\mathbf{a_1}\lambda^{\mathbf{4}} + \mathbf{a_2}\lambda^{\mathbf{2}} + \mathbf{a_3} + \mathbf{a_4}\lambda^{-\mathbf{2}}}) \tag{4.56}$$

where P_c is the pressure correction calculated from air pressure and air pressure at sea level (p_{0a}) is defined as:

$$P_c = \frac{p_a}{p_{0a}} \tag{4.57}$$

and the coefficients are:

$a_1 = 117.2594\,\mu\mathrm{m}^{-4}$

$a_2 = -1.3215\,\mu\mathrm{m}^{-4}$

$a_3 = 3.2073 \times 10^{-4}\,\mu\mathrm{m}^{-4}$

$a_4 = -7.6842 \times 10^{-5}\,\mu\mathrm{m}^{-4}$

4.1.3.2 Ozone attenuation

Ozone absorption ($\mathbf{T_{O_3}}(\lambda)$) is expressed as (Gueymard, 2005):

$$\mathbf{T_{O_3}}(\lambda) = \exp(-\mathbf{m_{O_3}}\tau_{\mathbf{O_3}}(\lambda)) \tag{4.58}$$

and the ozone optical thickness as:

$$\tau_{O_3}(\lambda) = u_{O_3} A_{O_3}(\lambda) \tag{4.59}$$

where u_{O_3} is the effective path length (provided for different Standard Atmospheres) and $A_{O_3}(\lambda)$ are ozone spectral absorption coefficients which are provided in (Gueymard, 2005). The effective path length (u_{O_3}) for different Standard Atmospheres is provided in (Gueymard, 2005) and the model allows for variations in u_{O_3} according to the choice of a Standard Atmosphere.

4.1.3.3 Water vapor attenuation

Water vapor transmittance ($\mathbf{T}_{H_2O}(lambda)$) is expressed as (Gueymard, 2005):

$$\mathbf{T}_{H_2O}(\lambda) = \exp(-[(m_w w_p)^{1.05}(f_w)^n B_w A_{w\lambda}]^c) \tag{4.60}$$

where w_p is total precipitable water, c and n are wavelength-dependent exponents, B_w is a correction factor, f_w is a pressure scaling factor, and $A_{w\lambda}$ are wavelength-dependent water vapor absorption coefficients. The pressure scaling factor is calculated as:

$$f_w = k_w[0.394 - 0.26946\lambda + (0.46478 + 0.23757)P] \tag{4.61}$$

where P is the pressure correction (eq. 4.57) and k_w is calculated as:

$$k_w = \begin{cases} 1 & \text{if } \lambda \leq 0.67\ \mu\text{m} \\ (0.98449 + 0.023889\lambda)w^q & \text{otherwise} \end{cases} \tag{4.62}$$

with

$$q = -0.02454 + 0.037533\lambda \tag{4.63}$$

The wavelength-dependent exponents are calculated as:

$$n(\lambda = 0.88631 + 0.025274\lambda - 3.5949\exp(-4.5445\lambda) \tag{4.64}$$

$$c(\lambda) = 0.53851 + 0.003262\lambda + 1.5244\exp(-4.2892\lambda) \tag{4.65}$$

The correction factor is calculated as

$$B_w = h(m_w w)\exp(0.1916 - 0.0785m_w + 4.706 \times 10^{-4}(m_w)^2) \tag{4.66}$$

where

$$h(m_w w) = \begin{cases} 0.624 m_w w^{0.457} & \text{if } A_{w\lambda} < 0.01 \\ (0.525 + 0.246 m_w w)^{0.45} & \text{otherwise} \end{cases} \tag{4.67}$$

4.1.3.4 Aerosol attenuation

For Mie scattering (aerosol transmissivity) ($\mathbf{T}_a(\lambda)$), the Ångstrøm turbidity formula was used, which is expressed as:

$$\mathbf{T}_a(\lambda) = \exp(-m_a \beta \lambda^{-\alpha}) \tag{4.68}$$

where β is the Ångstrøm turbidity coefficient. This is a user-controlled parameter and suggested values are 0.1 for clear atmosphere, 0.2 for turbid atmosphere, and 0.4 for very turbid atmosphere. The wavelength exponent (α) is related to the size distribution of the aerosols (also user-controlled parameter), and typical values range between 1.3 and 1.5. Wavelength in the Ångstrøm turbidity formula is in units of micrometers.

4.1.4 Direct irradiance

The exoatmospheric solar radiation ($E_m^0(\lambda)$) in units of W $\text{m}^{-2}\mu\text{m}^{-1}$ that is provided by spectral libraries has to be corrected for variation in earth-Sun distance using the eccentricity correction factor (4.8):

$$E^0(\lambda) = E_m^0(\lambda) F_{ec} \tag{4.69}$$

$E^0(\lambda)$ is the exoatmospheric solar radiation at normal-to-the-Sun surface. To derive the direct or beam Earth surface irradiance (E_{bn}) to normal-to-the-Sun surface, the atmospheric attenuation of solar irradiance is modeled. E_{bn} is related to the top of the atmosphere irradiance though the total transmission coefficient ($\mathbf{T}^{\downarrow}(\lambda)$) calculated as the product of the transmission coefficient ($\mathbf{T_i}(\lambda)$) of each extinction process (Muhammad Iqbal, 1983):

$$\mathbf{T}^{\downarrow}(\lambda) = \prod_{i=1}^{i=j} \mathbf{T_i}(\lambda) \tag{4.70}$$

In STSRM, attenuation due to Rayleigh scattering, ozone absorption, water vapor absorption, and aerosols extinction (see section 4.1.3) are considered. $\mathbf{T}^{\downarrow}(\lambda)$ is calculated as:

$$\mathbf{T}^{\downarrow}(\lambda) = \mathbf{T}_r(\lambda)\mathbf{T}_{O_3}(\lambda)\mathbf{T}_{H_2O}(\lambda)\mathbf{T}_a(\lambda) \tag{4.71}$$

The direct solar irradiance at the Earth surface normal-to-the-Sun is then expressed as:

$$E_{bn}(\lambda) = E^0(\lambda)\mathbf{T}^{\downarrow}(\lambda) \tag{4.72}$$

The solar irradiance is corrected for the Sun's position relative to the location of interest. Direct irradiance (E_b^h) on a horizontal surface is a function of the Sun's zenith angle (θ_s):

$$E_b^h(\lambda) = E_{bn}(\lambda) \cos \theta_s \tag{4.73}$$

If the surface is not horizontal but tilted, the direct solar irradiance is a function of the incidence angle (θ_i), which is the angle between the Earth-Sun vector and the normal to the surface:

$$E_b(\lambda) = E_{bn}(\lambda) \cos \theta_i \tag{4.74}$$

For arbitrary-oriented surface, the solar incidence angle is calculated as (Bishop and Colby, 2011):

$$\cos \theta_i = \cos \theta_s \cos \theta_t + \sin \theta_s \sin \theta_t \cos(\phi_t - \phi_s) \tag{4.75}$$

where θ_t is the terrain slope angle, ϕ_t is the terrain azimuth angle, and ϕ_s is the solar azimuth angle.

In STSRM, the shading of the terrain (S), which is 1 for no shading and 0 for shading (Bishop and Colby, 2011), is accounted for, and the direct beam irradiance is then expressed as:

$$E_b(\lambda) = E_{bn}(\lambda) S \cos\theta_i \tag{4.76}$$

Combining equations (4.71), (4.69), and (4.76) the following formulation is derived which is implemented in STSRM:

$$E_b(\lambda) = E_m^0(\lambda) F_{ec} \mathbf{T}^{\downarrow}(\lambda) S \cos\theta_i \tag{4.77}$$

4.1.5 Diffuse irradiance

The diffuse irradiance (E_d^h) on a horizontal surface may be divided into Rayleigh-scattered diffuse irradiance (E_r), aerosol-scattered diffuse irradiance (E_a), and diffuse irradiance scattered multiple times between ground and sky (E_g):

$$E_d(\lambda) = E_r(\lambda) + E_a(\lambda) + E_g(\lambda). \tag{4.78}$$

To account for the obstruction of the sky by the terrain, the total diffuse irradiance on an inclined unobstructed surface is multiplied by the hemispherical sky-view factor coefficient (V_f):

$$V_f = \sum_{\phi=0}^{360} \cos^2\theta_{max}(\phi, d) \frac{\Delta\phi}{360}, \tag{4.79}$$

where θ_{max} is the maximum local horizon angle at a given azimuth, ϕ, over a radial distance of d.

STSRM utilizes the parameterization of Bird and Riordan (1986) but have not accounted for the secondary influence by ground reflectance. The Rayleigh and aerosol components are computed as:

$$E_r(\lambda) = E_m^0(\lambda) F_{ec} \cos\theta_s \mathbf{T}_{O_3}(\lambda) \mathbf{T}_{gas}(\lambda) \mathbf{T}_{H_2O}(\lambda) \mathbf{T}_{aa}(\lambda) \left(1 - \mathbf{T}_r(\lambda)\right) 0.5 \tag{4.80}$$

$$E_a(\lambda) = E_m^0(\lambda) F_{ec} \cos\theta_s \mathbf{T}_{O_3}(\lambda) \mathbf{T}_{gas}(\lambda) \mathbf{T}_{H_2O}(\lambda) \mathbf{T}_{aa}(\lambda) \mathbf{T}_r^{1.5}(\lambda)(1 - \mathbf{T}_{as}(\lambda)) F_s \tag{4.81}$$

$$\mathbf{T}_{as}(\lambda) = \exp(-\omega(\lambda)\tau_a(\lambda) m_{re}) \tag{4.82}$$

$$\mathbf{T}_{aa}(\lambda) = \exp[-(1 - \omega(\lambda))\tau_a(\lambda) m_{re}] \tag{4.83}$$

where $\mathbf{T}_{aa}(\lambda)$ is the transmittance term for aerosol absorption, $\mathbf{T}_{as}(\lambda)$ is the transmittance term for aerosol scattering, F_s is the fraction of aerosol scattering that is downward, m_{re} is the relative air mass, and $\omega(\lambda)$ is the aerosol single scattering albedo defined by Gueymard (1995).

Calculating the diffuse irradiance due to aerosols requires the use of the spectral asymmetry factor, which accounts for humidity (Gueymard, 1995). STSRM allows for different values of the asymmetry factor through the choice of a Continental aerosol model, Urban aerosol model, or Maritime aerosol model (Table 4.4).

The parameter $\tau_a(\lambda)$ is the aerosol optical depth and can be calculated using the Ångstrøm turbidity formula:

$$\tau_a(\lambda) = \beta\lambda^{-\alpha}, \tag{4.84}$$

where β is the turbidity coefficient and α is the aerosol size distribution parameter.

The fraction of aerosol scatter that is downward is calculated as a function of the solar zenith angle:

$$F_s = 1 - 0.5 \exp[(A_{fs} + B_{fs} \cos\theta_s) \cos\theta_s], \tag{4.85}$$

$$A_{fs} = A_{lg}[1.459 + A_{lg}(0.1595 + A_{lg} 0.4129)], \tag{4.86}$$

$$B_{fs} = A_{lg}[0.0783 + A_{lg}(-0.3824 - A_{lg}0.5874), \tag{4.87}$$

$$A_{lg} = \ln(1 - g_a). \tag{4.88}$$

The diffuse irradiance is then be calculated as:

$$E_d = E_d^h \left\langle \left\{ E_b/[E_m^0(\lambda)F_{ec}\cos(\theta_s)] \right\} + 0.5[1 + cos(\theta_t)][1 - E_{bn}/(E_m^0(\lambda)F_{ec})] \right\rangle$$
$$+0.5E_t^h \alpha_g [1 - \cos(\theta_t)]V_f \tag{4.89}$$

where E_t^h is the total surface irradiance on a horizontal surface, and E_{bn} is the direct irradiance at a normal to the Sun surface:

$$E_t^h = E_b^h + E_d^h \tag{4.90}$$

4.2 Solar radiation model validation

Validation of the solar radiation model is performed in two stages. In the first stage, solar radiation simulations are compared to measurements obtained at a number of National Renewable Energy Laboratory (NREL) solar radiation stations (Wilcox, 2012). The second validation stage compares solar radiation simulations of the new model, as well as of the models implemented in ArcGIS (Fu, 2000; Fu and Rich, 2002) and QGIS (Hofierka and Šurí, 2002). Validating to solar radiation measurements allows for estimates of the accuracy of the new model. The comparisons to the other two solar radiation models, however, provide only information as to the difference between the three sets of results, but without the ability to assess accuracy.

4.2.1 Validation with measured solar radiation

NREL offers the Solar Radiation Database 1991-2010 (Wilcox, 2012), which provides solar and meteorological data for 1,454 stations in the United States, most of which provide only modeled solar radiation. However, 38 of the stations with instrumentation to measure direct, diffuse, and total solar radiation (Fig. 4.2) are located in the contiguous U.S. and Alaska. The record contains missing data for some periods during these ten years. The 38 stations with available solar radiation measurements are located in 21 states. One station per state was selected at random (Fig. 4.2), of which two stations were not used: Barrow, Alaska (not used because it is beyond the Arctic Circle); and Bismarck, North Dakota (not used because none of the data of the station passed our semi-automatic data quality filter described below).

We randomly selected one year from each station from among the years with available solar radiation measurements. Years with extensive periods of no measurements were excluded from this selection. For the random year, one day per season was selected (through a semi-automated analysis) to be compared to the solar radiation model results. Seasons were defined as Winter, Spring, Summer, and Fall, which respectively comprise the months of December through February, March through May, June through August, and September through November.

The current implementation of this solar radiation model does not account for cloud cover. Therefore, to compare the model to measured solar radiation, it was important to select days with none to minimal cloud cover. This was achieved by a simple calculation of the difference between total daily and direct daily solar irradiance measured by the station. The day with the smallest difference was identified and visually examined to ensure that it did not exhibit any irregularity in the measured direct solar radiation that would be indicative of cloud cover. If it was so indicative, then the next best day was selected.

In terms of assessing the ability of STSRM to account for topography, it should be noted that the ideal validation of the solar radiation model would involve comparisons of simulated solar irradiance to measured solar irradiance at locations with various topographic effects. However, solar radiation is regularly measured at locations that minimize terrain

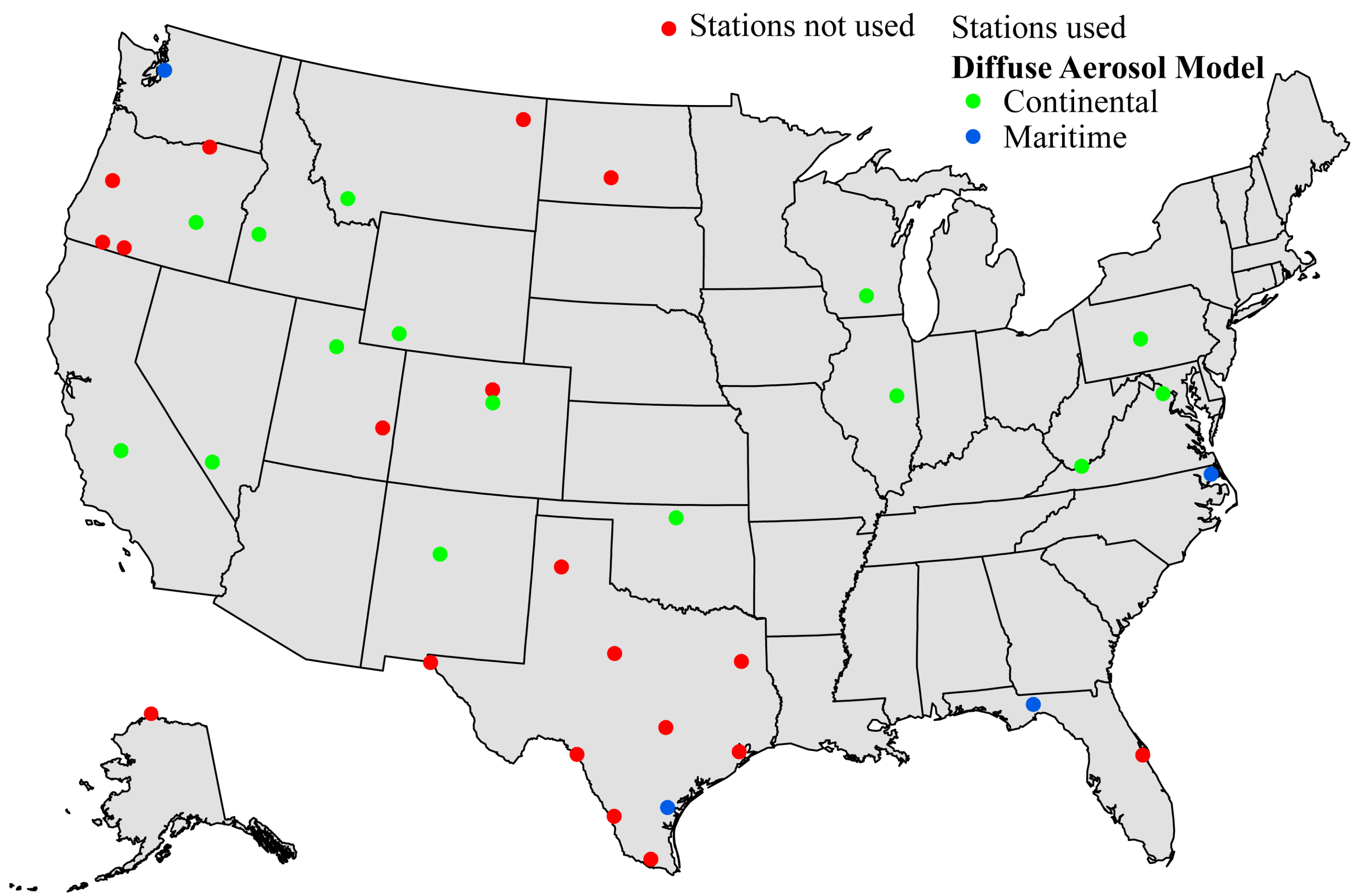

Figure 4.2: NREL stations with solar radiation measurements.

effects. For example, stations in mountainous areas are often located at high elevation locations, such as the NREL station in Bluefield, WV. Thus, the comparison of STSRM simulations to NREL station observations does not involve computing the cast shadow or the skyview factor, both of which are used by STSRM to model the topographic effects on solar radiation.

4.2.2 Comparison to ArcGIS and QGIS

STSRM is compared to the models in ArcGIS (Fu and Rich, 2002) and QGIS (Hofierka and Šurí, 2002) over a 75 km by 75 km area centered over the region surrounding Nanga Parbat, Pakistan (Figure 4.3). Nanga Parbat is the ninth highest mountain in the world, and the terrain represents one of the most extreme regions in the world with respect to topography characterized by more than seven thousand meters of relief (Fig. 4.3). It was selected because of our focus on the effects of the topography on surface solar irradiance.

Table 4.6 provides the model parameters used to simulate solar irradiance of the three models. Since STSRM does not yet provide a cloud cover parameterization, it was important to choose parameters for the other two models that characterize clear sky conditions. Thus, a uniform sky-diffuse model and transmissivity of 0.5 were selected for ArcGIS, and a Linke turbidity coefficient of 3 was selected for QGIS, as suggested by the documentation of the two software packages. Note that the solar radiation model within QGIS also produces adjacent-terrain (reflected) irradiance, unlike the other two models. We are aware that we could have computed the Linke turbidity coefficient and that we also could have created an albedo map over the study area instead of using the default values of these parameters within QGIS; however, we decided to test the models without providing additional information, mimicking a user experience when one does not have this additional information.

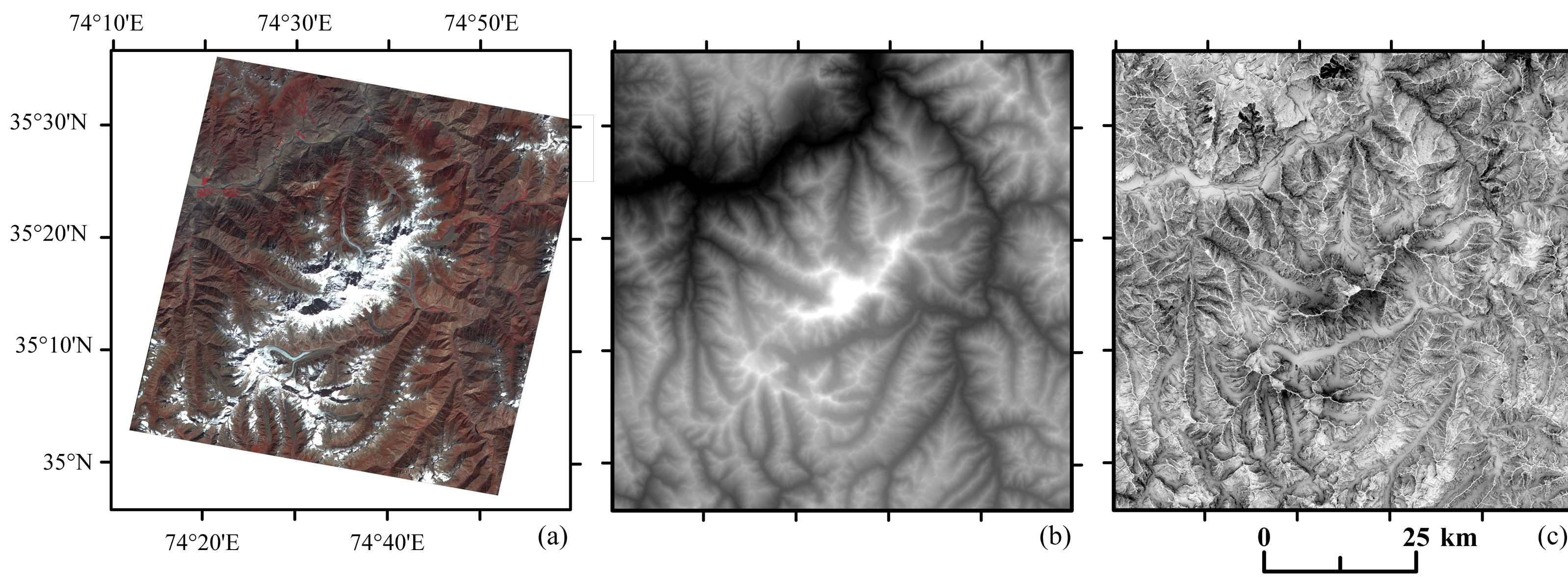

Figure 4.3: The Nanga Parbat massif located in northern Pakistan.

Table 4.6: The parameters of the solar radiation models used for validation.

STSRM	ArcGIS	QGIS
Atmo. profile - Midlatitude Summer Ozone path length - Sub Tropical Summer Diffuse Aerosol Model - Continental	Sky size / Resolution - 1024 **Topographic Parameters:** Z factor - 1 Slope and aspect from DEM Calculate directions - 360 **Radiation Parameters:** Zenith divisions - 8 Azimuth divisions - 8 Diffuse model type - Uniform sky Diffuse proportion - 0.3 Transmissivity - 0.5	Linke turbidity coef. - 3 Ground albedo coef. - 0.2 Sampling distance step coef. - 0.5 (Any other parameters - left blank)

4.3 Glacier selection

A total of 97 glaciers (Figure 4.4) were selected for this study, and the corresponding glacier outlines from the Randolph Glacier Inventory (RGI 6.0) were identified. RGI 6.0 is a global glacier inventory created and maintained within the Global Land Ice Measurements from Space initiative (Consortium et al., 2017). Ideally, every glacier within the study area will be considered to avoid any subjectivity in the analysis. However, this was not possible in this study, because certain variables required a substantial amount of manual effort. For example, the set of characterization variables includes several catchment-scale characteristics, which required the manual delineation of catchment boundaries.

Various software and scripts were explored for automated delineation of catchments. Ultimately, PyGeoprocessing was utilized to outline catchment boundaries. PyGeoprocessing is a collection of geoprocessing routines developed at the Natural Capital Project

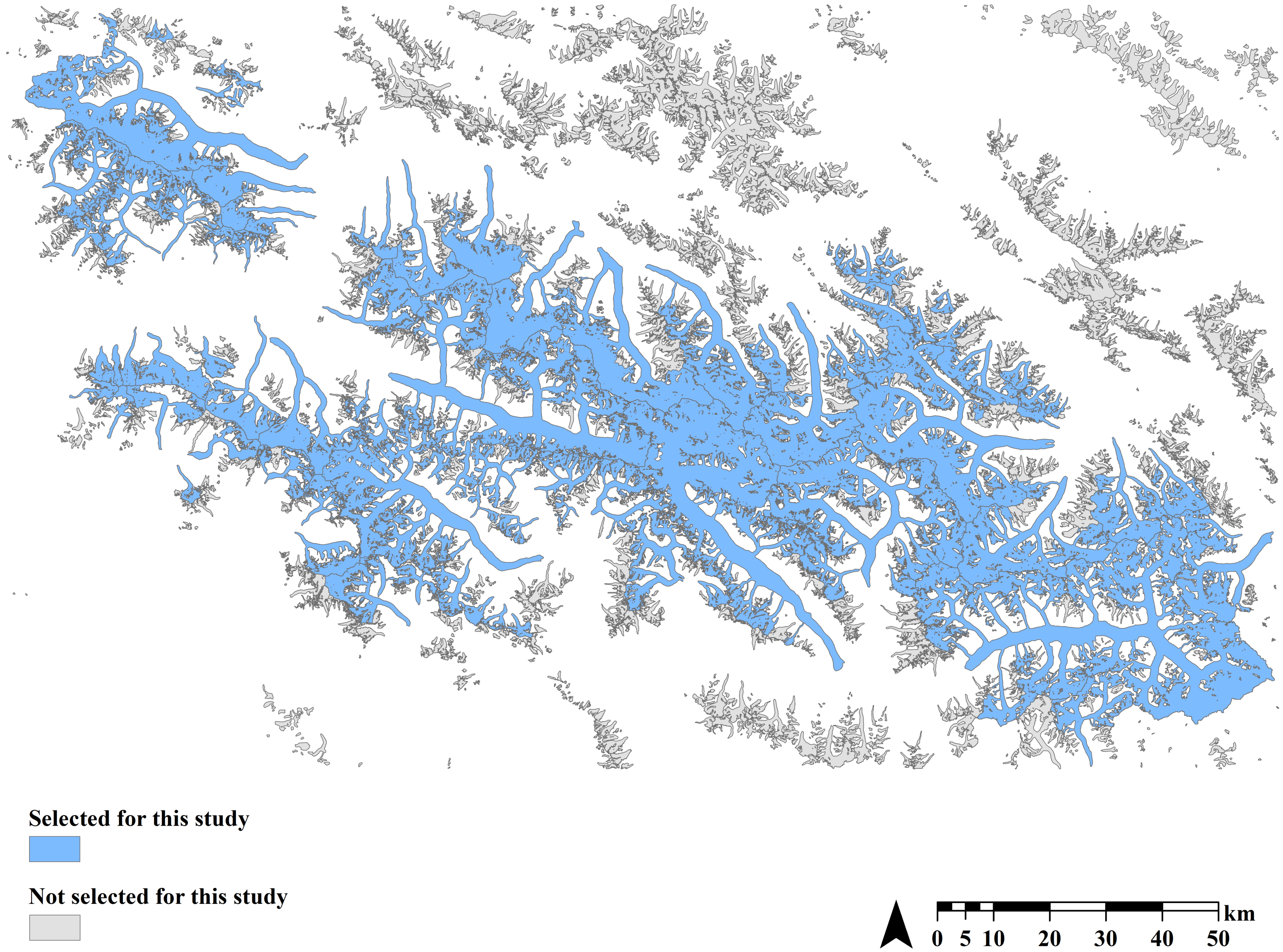

Figure 4.4: Glacier outlines as provided by RGI 6.0 (Consortium et al., 2017). The 97 selected glaciers for this study are in blue.

(Natural-Capital-Project, 2018). However, manually modifying the outlines was still necessary. The skyview map of the study area and Google Earth were used to visually identify where the boundaries should be. A map of the delineated catchments is presented in Figure 4.5.

4.4 Glacier characterization

4.4.1 Surge type glaciers

Glaciers in the Karakoram mountain range are an active area of research, especially because they represent a cluster of surge type glaciers. There are three recent studies that identify a cluster of surge type glaciers in the region. Rankl et al. (2014) utilized Landsat data from 1976 to 2012, as well as synthetic aperture radar (SAR) data, to map advancing, stable, retreating, and surge type glaciers in the Karakoram mountain range (Figure 4.6). A finding of her study is that surge type glaciers are generally longer than non-surge type glaciers, and length is one of the glacier variables included in our analysis.

Sevestre and Benn (2015) investigated the climate and glacier geometry controls on global surge type glacier distribution. A global database of surge type glaciers was compiled, through information from previous published research (Figure 4.7). Surge type glacier codes are provided through with RGI 6.0 (Consortium et al., 2017) - observed, probable and possible surge type.

The third and most recent Karakoram surge type glacier database is provided by Bhambri et al. (2017), who utilize previous work and archival materials collected since the 1840s, and also Landsat and ASTER data plus ground observations. Four surge type and two surge-like categories are identified. For our study, we chose to use this database as it is the most recent and most comprehensive to-date database of Karakoram surge type glaciers. All four surge type categories are combined for this study (Figure 4.8).

There is evidence that surge type tributary glaciers are generating surge-modified be-

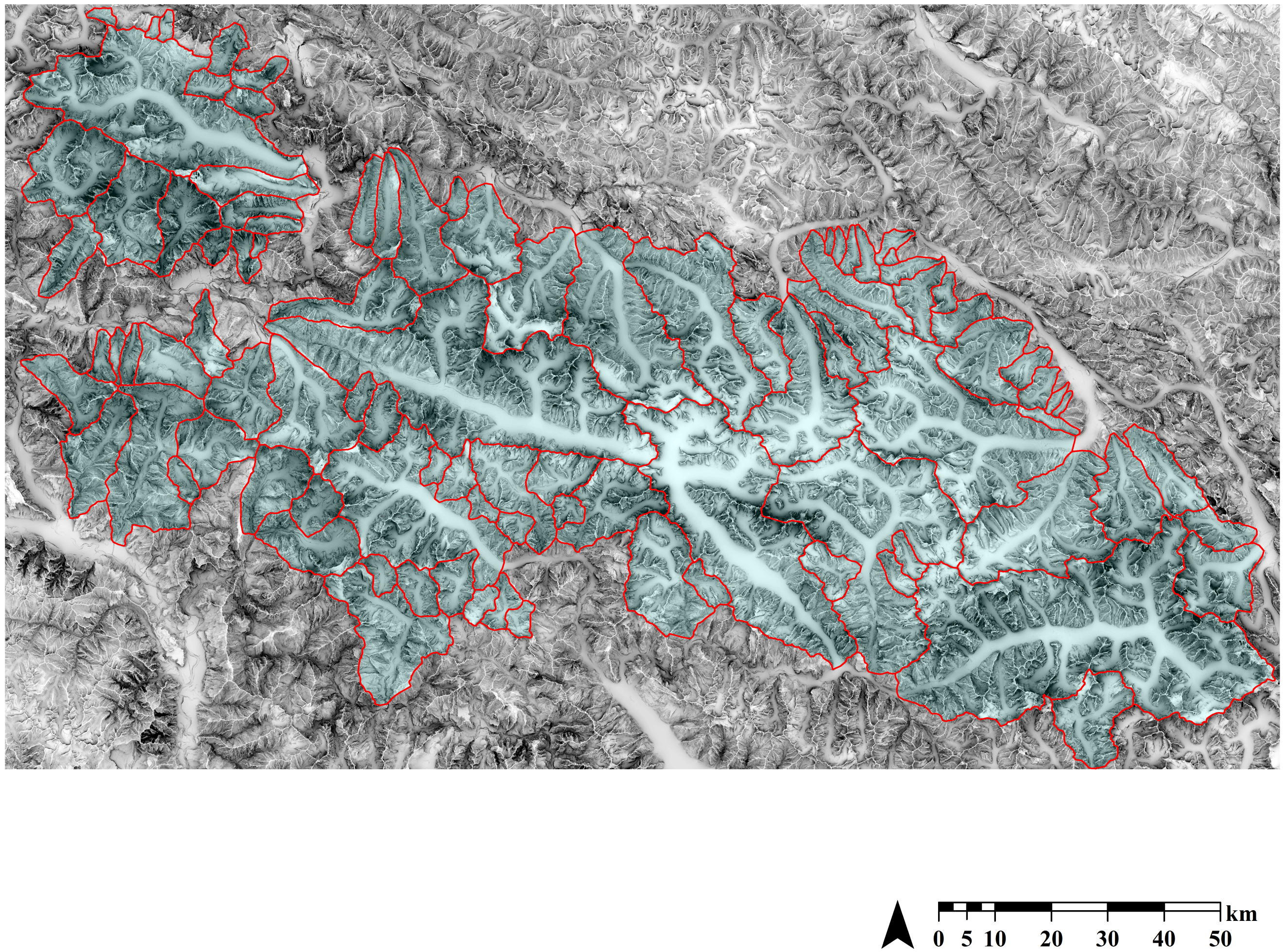

Figure 4.5: The delineated catchments outlined in red.

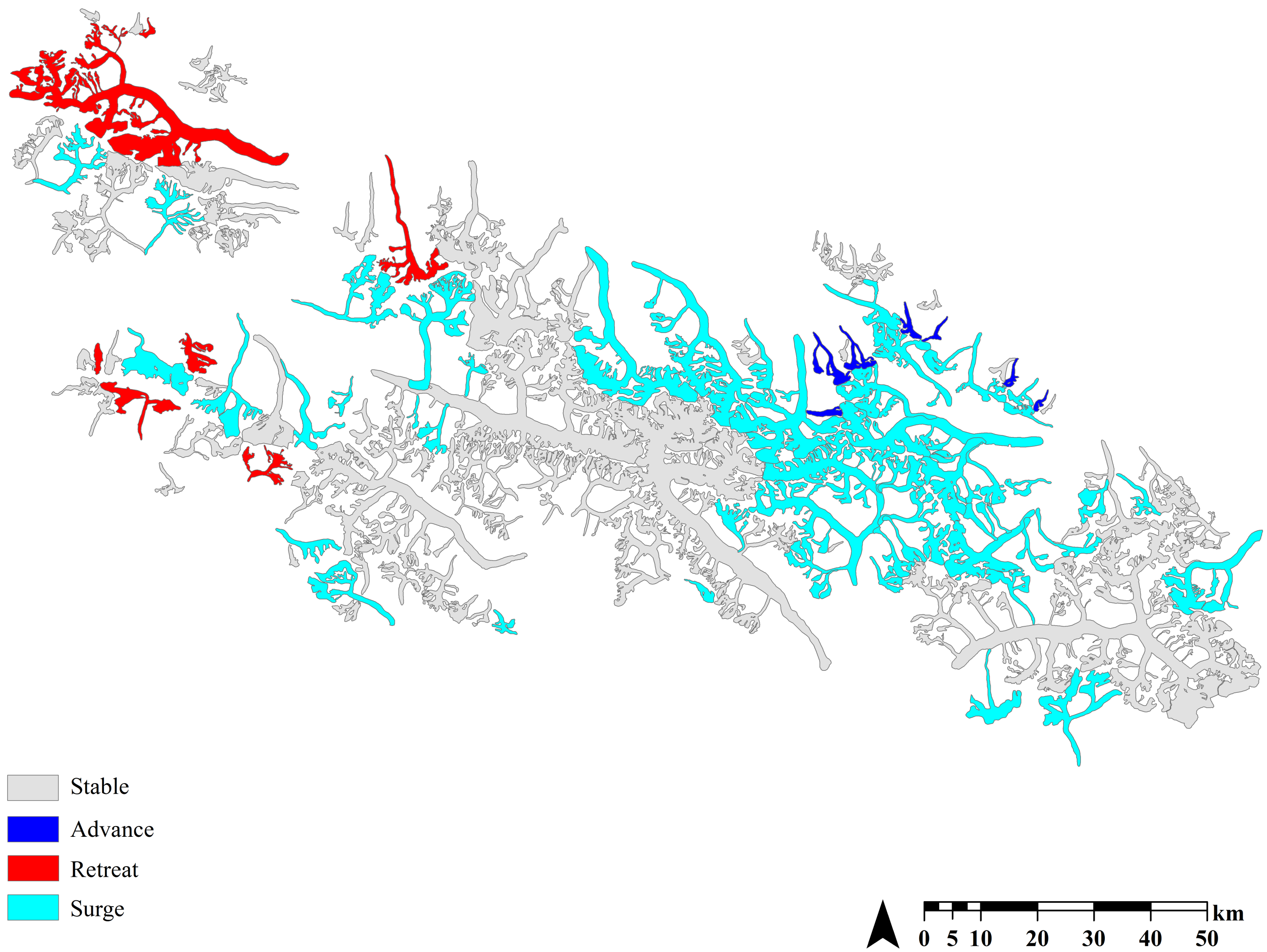

Figure 4.6: The selected glaciers as identified by Rankl et al. (2014)

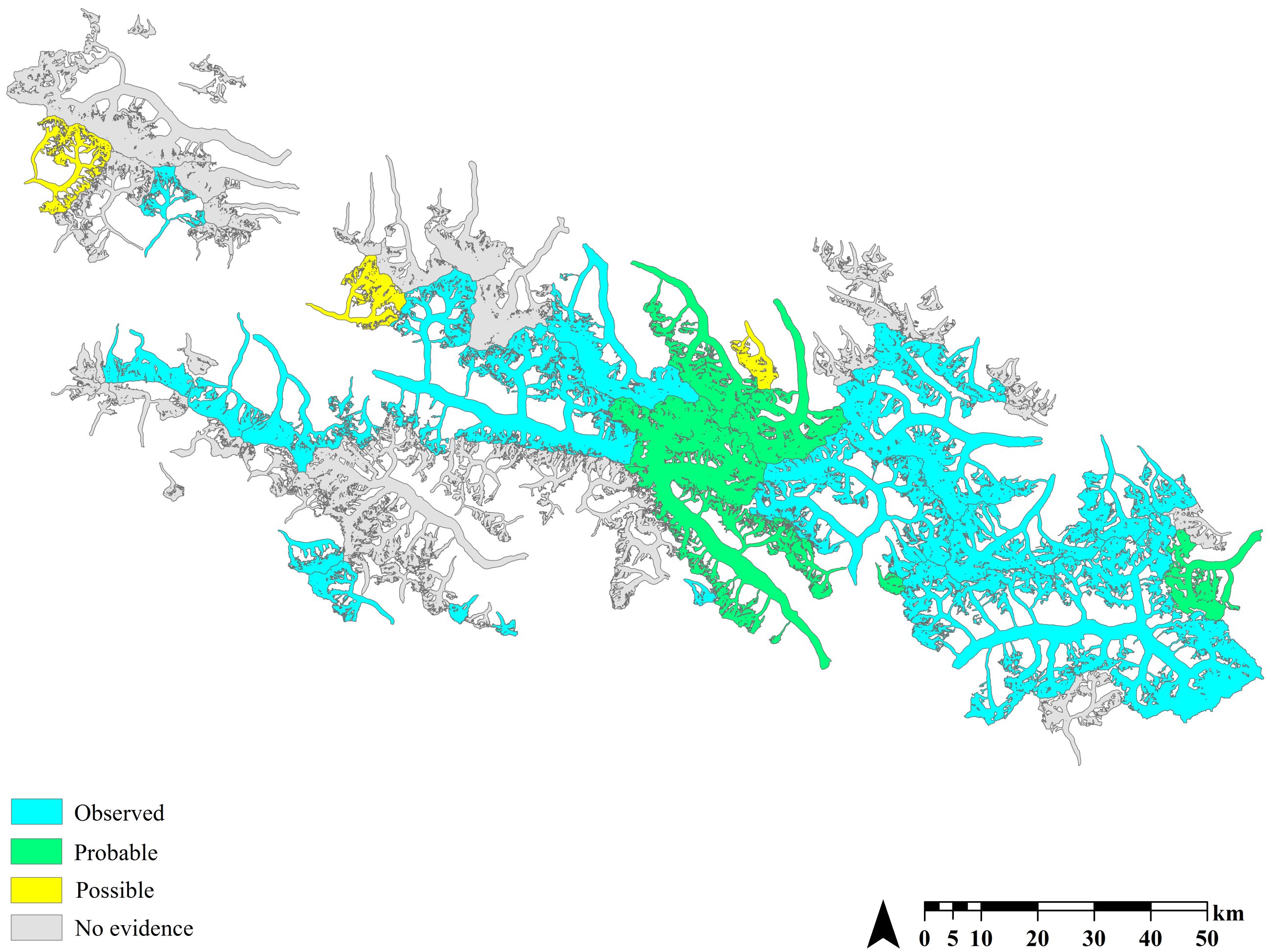

Figure 4.7: The selected glaciers as identified by Sevestre and Benn (2015).

havior in the main glaciers where they connect (Bhambri et al., 2017). Thus, the main glaciers with surge type tributaries are considered as surge type for this analysis. Furthermore, we are exploring the characteristics of the whole glacier, and also of the catchment of the glacier. Thus, a catchment with surge type tributary glaciers is showing that the area has conditions favorable to producing surge type glaciers.

4.4.2 Advancing and retreating glaciers

The study area is dominated by surge type glaciers so there is no large enough sample of advancing and retreating glaciers to perform statistical analysis. However, a qualitative analysis and discussion of advancing versus retreating glaciers is offered. Identifying advancing and retreating glaciers is always a function of the time period studied and the method utilized. Thus, a glacier can easily be identified as exhibiting different dynamics through different studies. An example of this is the Momhil glacier (RGI60-14.03405), which is identified as advancing by Rankl et al. (2014), surge type by Bhambri et al. (2017), and no observable surge type behavior by Sevestre and Benn (2015).

Since quantifying glacier retreat and advance rates was not the purpose of this study, we use the existing glacier databases of the Karakoram mountain range to identify which glaciers are surge type, and which glaciers are advancing or retreating. Rankl et al. (2014) used Landsat data from 1976 to 2012 as well as SAR (synthetic aperture radar) data and identified stable, advancing, retreating, and surge type glaciers in the Karakoram mountain range, and her database was utilized to identify the advancing and retreating glaciers. The two types of glaciers are qualitatively analyzed in terms of their location, size, orientation, terrain slope, and radiation exposure.

4.4.3 Glacier and catchment geomorphic characterization

Glacial erosional processes, climate and tectonics are imprinted on the topography (Figure 4.9). Thus, topographic attributes are related to system dynamics. A list of glacier-

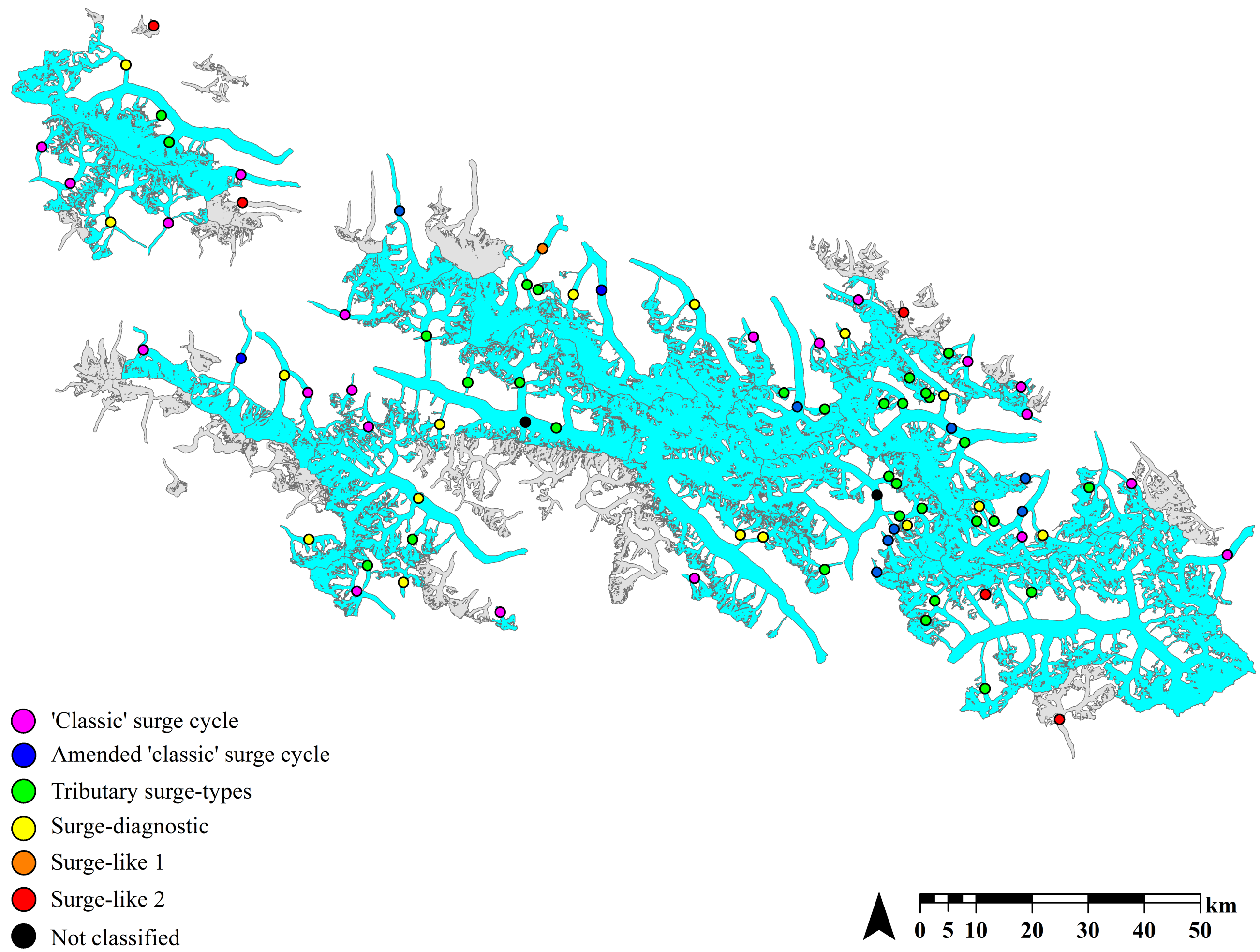

Figure 4.8: The selected glaciers as identified by Bhambri et al. (2017).

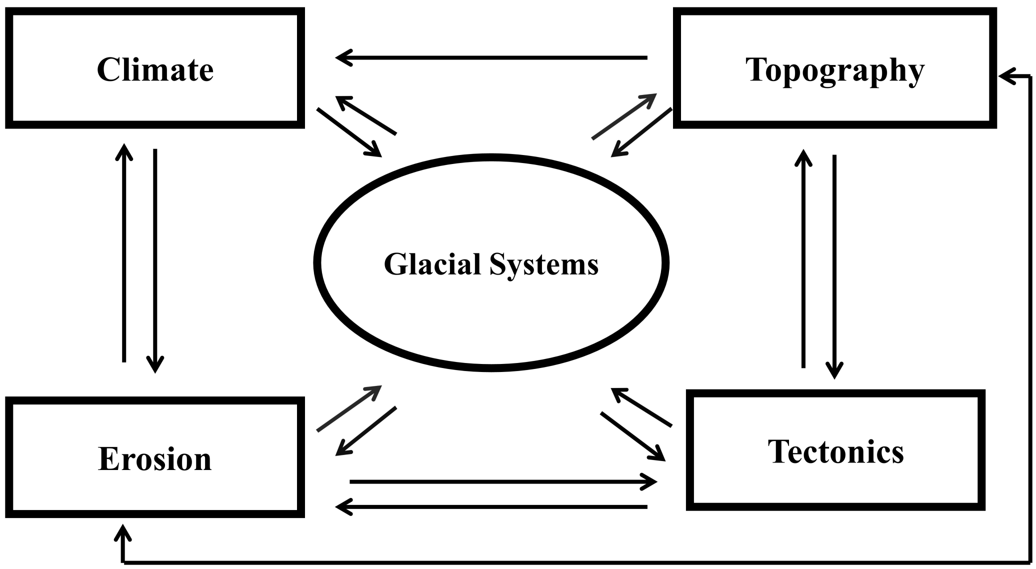

Figure 4.9: System dynamics.

scale and catchment-scale geomorphic characteristics is compiled in Table 4.7, and some of these variables have already been related to surge type versus non-surge type glaciers (Jiskoot et al., 1998, 2000; Barrand and Murray, 2006; Sevestre and Benn, 2015). This study utilized terrain and slope averaged over the glacier centerline, as well as over the whole glacier. Also unique to this study is the inclusion of catchment-scale geomorphic variables.

Glacier centerlines (Figure 4.10) were derived through the Open Global Glacier Model (OGGM) v1.0, an exciting glaciological collaboration (Maussion et al., 2018a,b). OGGM includes the centerline detection algorithm of Kienholz et al. (2014). The glacier-scale variable 'branchiness index', which is the number of glacier branches detected by the algorithm, is also derived through this algorithm. This variable is important as it indicates the level of glacier complexity, and has been previously used in analysis of surge type glaciers by Sevestre and Benn (2015).

In addition to these geomorphic variables, there is also a database of debris cover dis-

Table 4.7: Geomorphic parameters

Glacier-scale	Catchment-scale
Altitude of terminus (km)	Catchment planimetric area (km^2)
Minimum altitude (km)	Catchment surface area (km^2)
Maximum altitude (km)	Catchment relief (km)
Relief (km)	Catchment hypsometric interval
Mean altitude (km)	Catchment skyview averaged over total area
Planimetric area (km^2)	Catchment perimeter (km)
Surface area (km^2)	Catchment shape index (x 10^5)
Slope averaged along centerline (degrees)	
Slope averaged over glacier area (degrees)	
Cosine and sine of aspect averaged along centerline	
Cosine and sine of aspect averaged for total area	
Hypsometric interval	
Length (km)	
Branchiness index	
Perimeter (km)	
Shape index (x 10^4)	

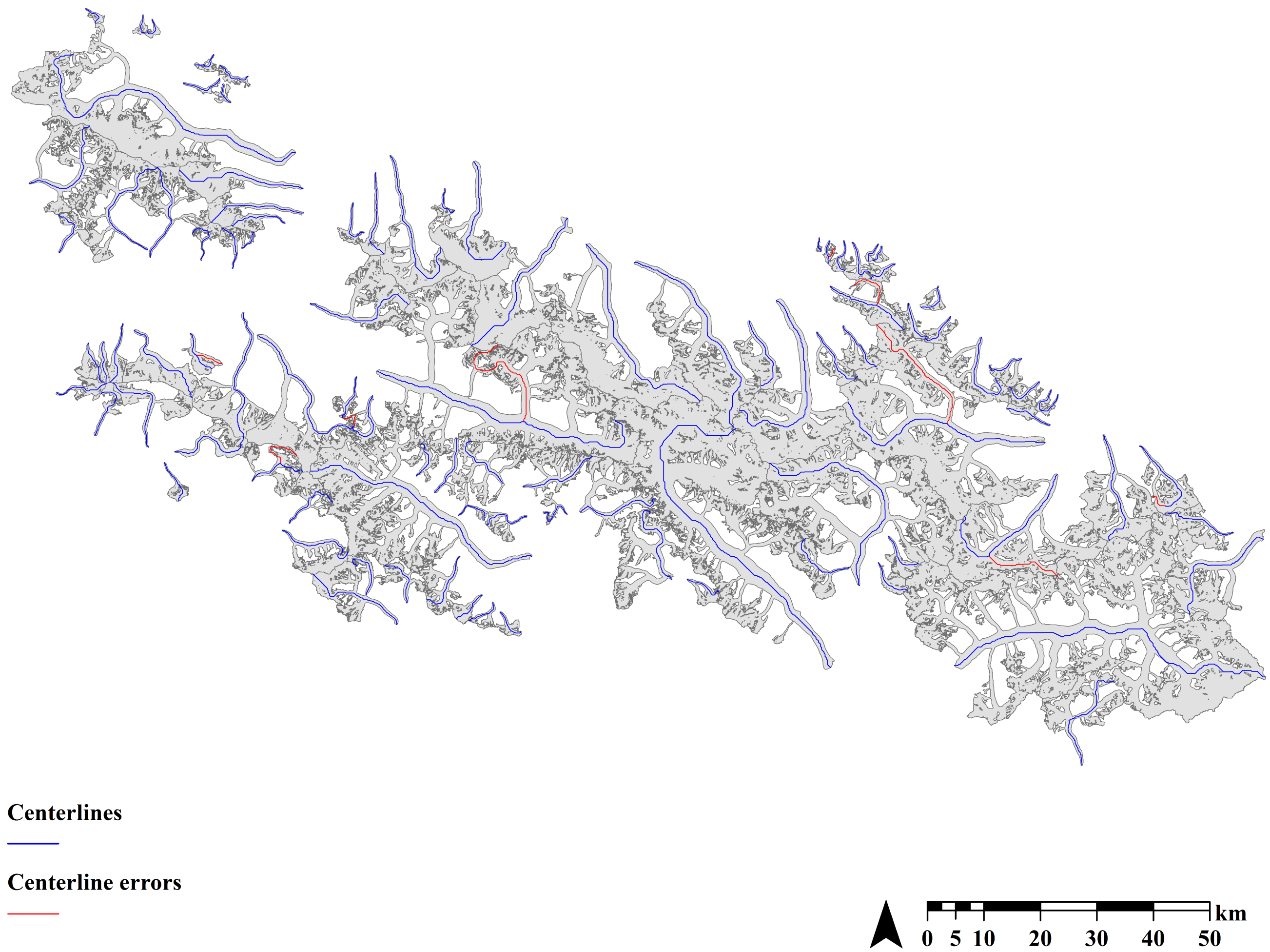

Figure 4.10: Glacier centerlines as identified by OGGM (Maussion et al., 2018a,b). Red lines show centerlines which were corrected.

Table 4.8: Solar radiation simulations data summary.

Day	Month	Start time	End time	Number of grids
1	May	5:00	19:00	55
11	May	4:45	19:00	56
21	May	4:45	19.15	57
31	May	4:30	19.15	68
10	June	4:30	19:30	59
20	June	4:30	19:30	59
30	June	4:30	19:30	59
10	July	4:45	19:30	58
20	July	4:45	19.15	57
30	July	5:00	19.15	56
9	August	5:00	19:00	53
19	August	5.15	18:45	53
29	August	5.15	18:45	53
8	September	5:30	18:30	51
18	September	5:30	18.15	50
28	September	5:45	18:00	48

tribution over the Karakoram glaciers. Mölg et al. (2018) utilized ASTER GDEM Version 2, Landsat TM and Landsat ETM + data, and coherence images derived from ALOS-1 PALSAR-1 to delineate debris cover (Figure 4.11).

4.5 Solar radiation characterization

The developed solar radiation model was used to produce simulations over the 2016 ablation season from May 1^{st} to September 28^{th}. Simulations were performed for every 10th day and with a 15 minute time step (Table 4.8). The first and last grids are at the time step when first and last irradiance is present on the landscape. Topographic effects on the diurnal solar irradiance were characterize through the kurtosis of the daily solar radiation curves over the ablation season. Seasonal topographic effects were characterized by analyzing the average surface solar irradiance over the ablation season below the equilibrium line altitude (ELA).

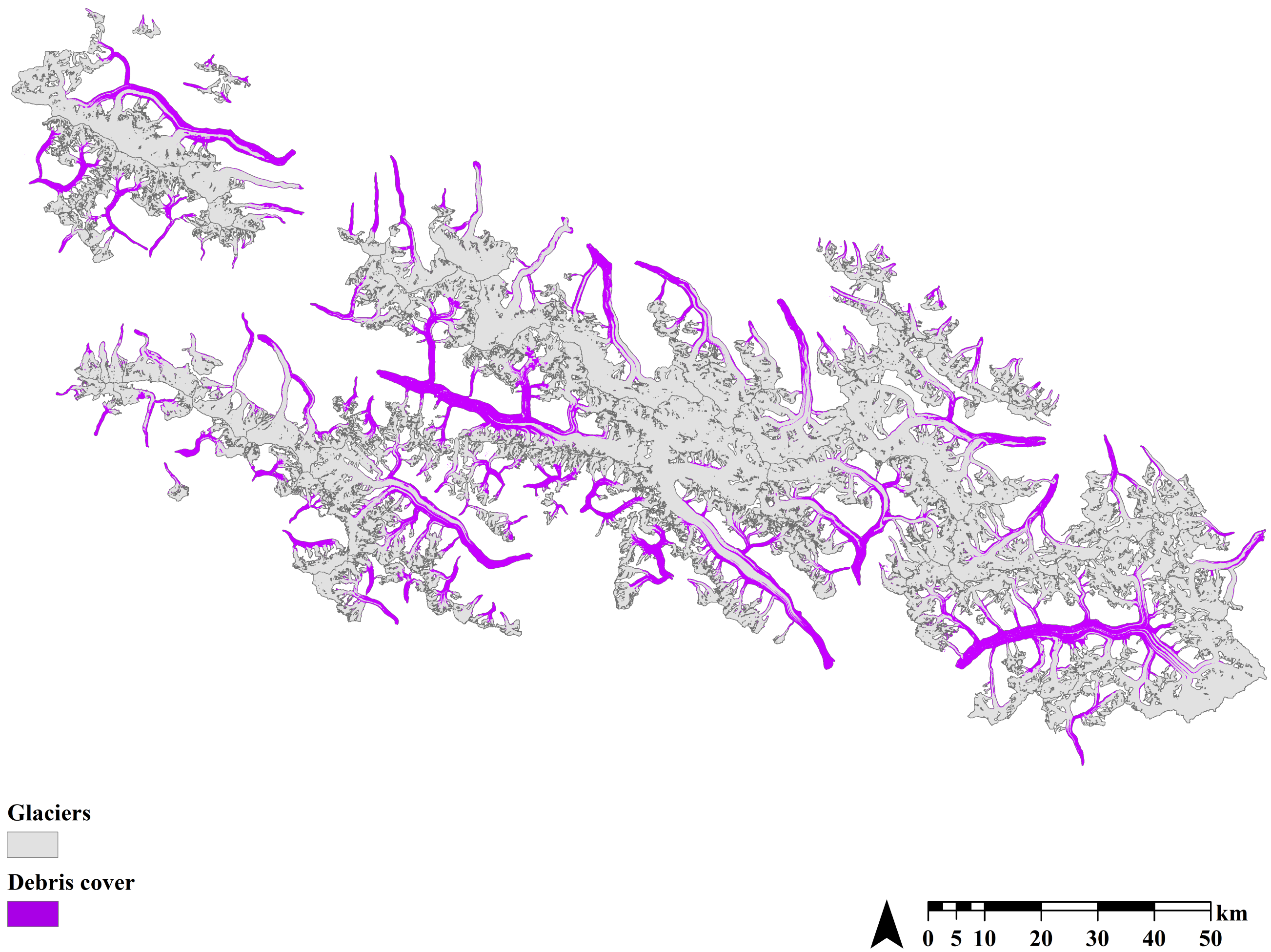

Figure 4.11: Debris cover on the selected glaciers as identified by Mölg et al. (2018).

4.5.1 Kurtosis of diurnal surface irradiance

Topographic effect is pronounced in the morning and evenings due to the large relief in the Karakoram mountain range (Figure 4.12). The kurtosis time-series over the ablation season of the diurnal solar irradiance for each pixel was used as an indication of the cast-shadow influence on surface irradiance (Figure 4.13). The kurtosis of the diurnal direct solar irradiance reveals greater influence of the regional relief given a lower kurtosis value, and vice versa. Kurtosis is a measure of the 'peakedness' (the width of the peak) of a frequency distribution, and thus lower kurtosis means greater topographic influence as the tails of the graph are 'clipped' due to morning and/or evening shadowing.

An unsupervised 2 x 3 self-organizing map was then used to identify the dominant ablation season patterns of kurtosis. Self-organizing maps are a type of an artificial neural network that produces topologically-ordered maps of dominant patterns or modes representing the input data (Kohonen, 1990). During the learning process, a winner that most closely marches the input sample is identified, but modification is performed within a radius of the winning neuron decreasing from it. A review of the technique with an emphasis on its use in remote sensing is available by Filippi et al. (2010).

Plots (Figure 4.14) and a map (Figure 4.15) present this unique information in a way that can be easily understood. Nodes (or patterns) 1, 4 and 6 show low kurtosis throughout the ablation season. These areas, in narrow valleys and adjacent to valley walls, were combined (presented as red in Figure 4.16). Nodes 3 and 5, on the other hand, show high kurtosis, with these representing mostly the valley floors of large glaciers (presented as yellow in Figure 4.16). Note that the kurtosis of node 5 falls drastically at the end of the ablation season due to seasonal topographic effect. Node two was discarded as there is no spatial pattern to it and it appears as intermediate between the other two categories.

The area of combined nodes 3 and 5 and the area of combined nodes 1,4 and 6 were

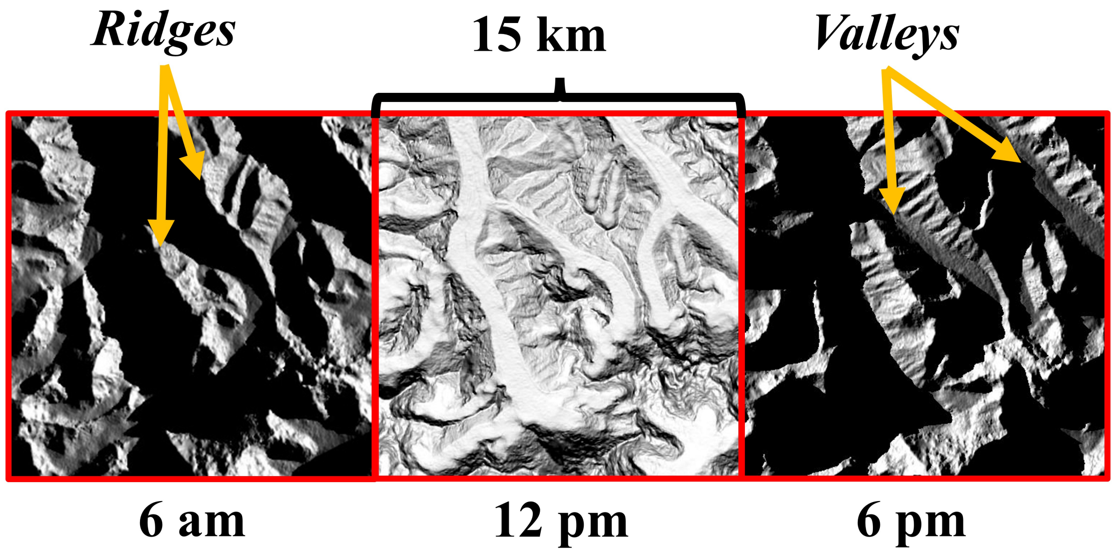

Figure 4.12: Diurnal direct irradiance cast-shadow influence.

computed for each glacier, then an index of the ratio of the two areas was calculated. This ratio was used as a characterization of the diurnal topographic effect for each glacier. A higher value of the ratio indicates a glacier affected less by the topography than a glacier with a lower value of the ratio. Note that pixels of node 2 were discarded as 'unclassified' due to the randomness of the spatial pattern of the node.

4.5.2 Ablation-season surface irradiance

Each set of daily surface irradiance was integrated for the day and averaged over the ablation season (Figures 4.17, 4.18, 4.19). Altitudinal curves of solar irradiance were computed for each glacier. The accumulation areas of the glaciers are above the freezing line, thus surface irradiance at the higher portions of the glaciers is not important for glacier melt. There are several estimates of the Equilibrium Line Altitude (ELA) for the Karakoram and we chose 5050 m computed by Shrestha et al. (2015) and also utilized by Baig et al. (2018). Surface solar irradiance was averaged below that altitude. A t-test was performed to test if

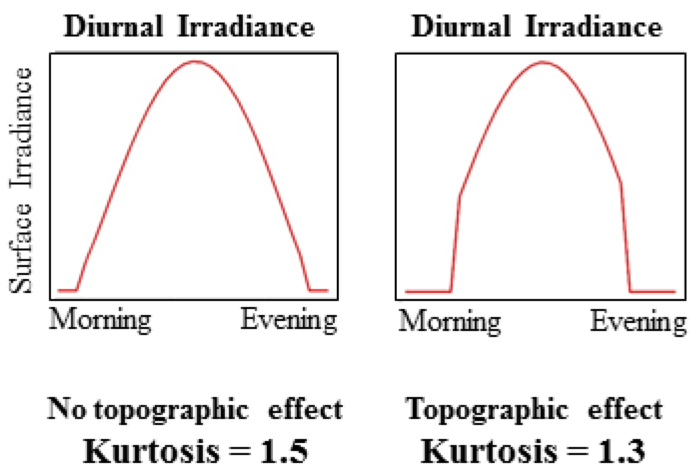

Figure 4.13: Diurnal irradiance patterns. This figures demonstrates the concept of kurtosis as a characterization of topographic influence on surface solar irradiance.

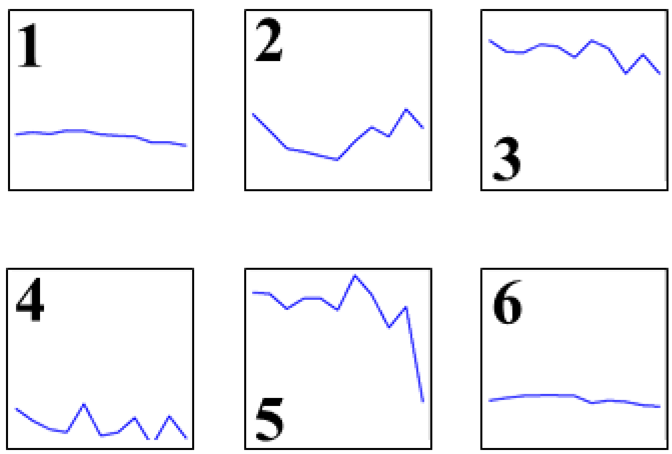

Figure 4.14: Dominant kurtosis patterns identified by a 2 x 3 self-organizing map.

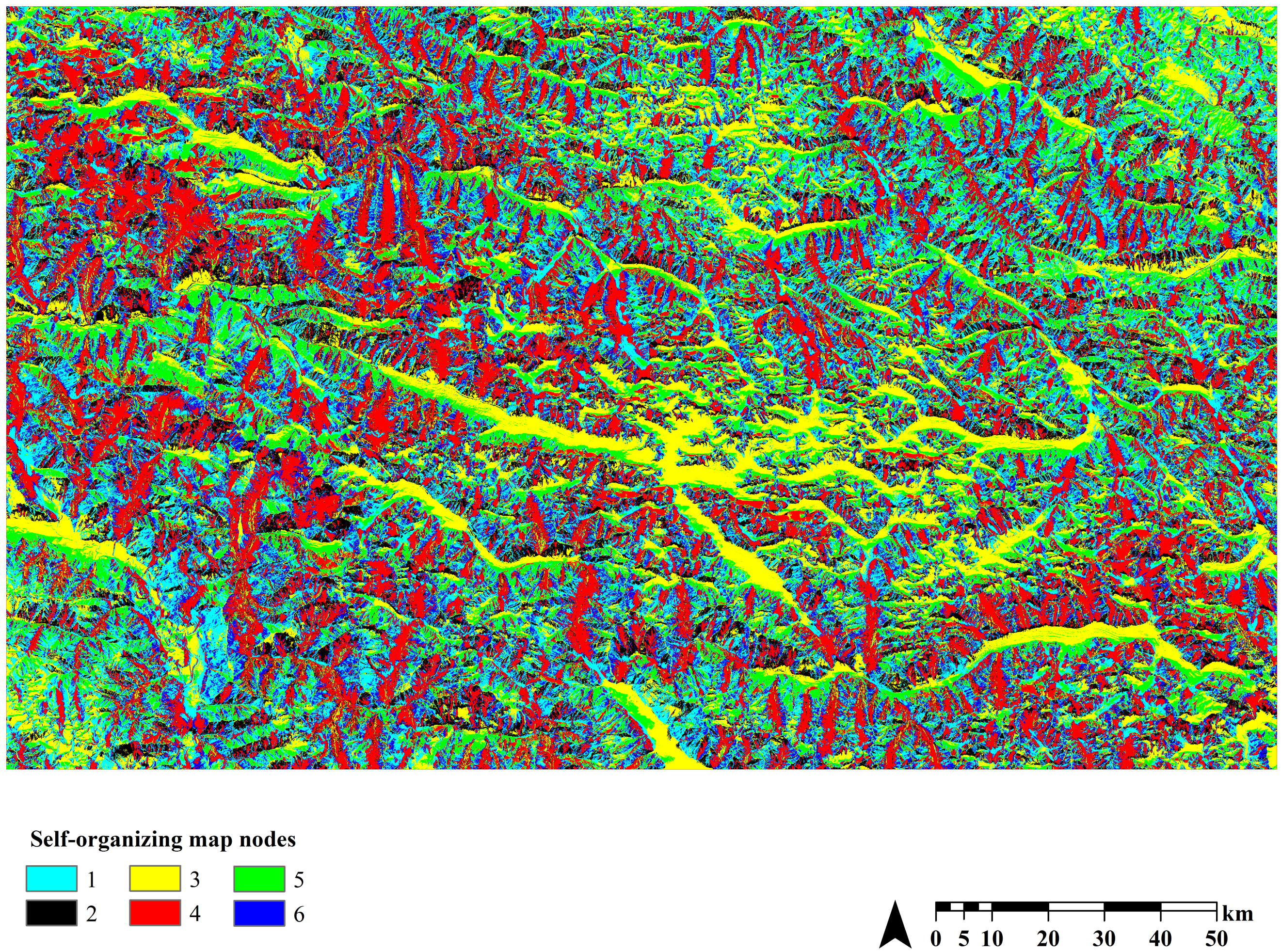

Figure 4.15: A map of the six dominant kurtosis patterns identified by the 2 x 3 self-organizing map.

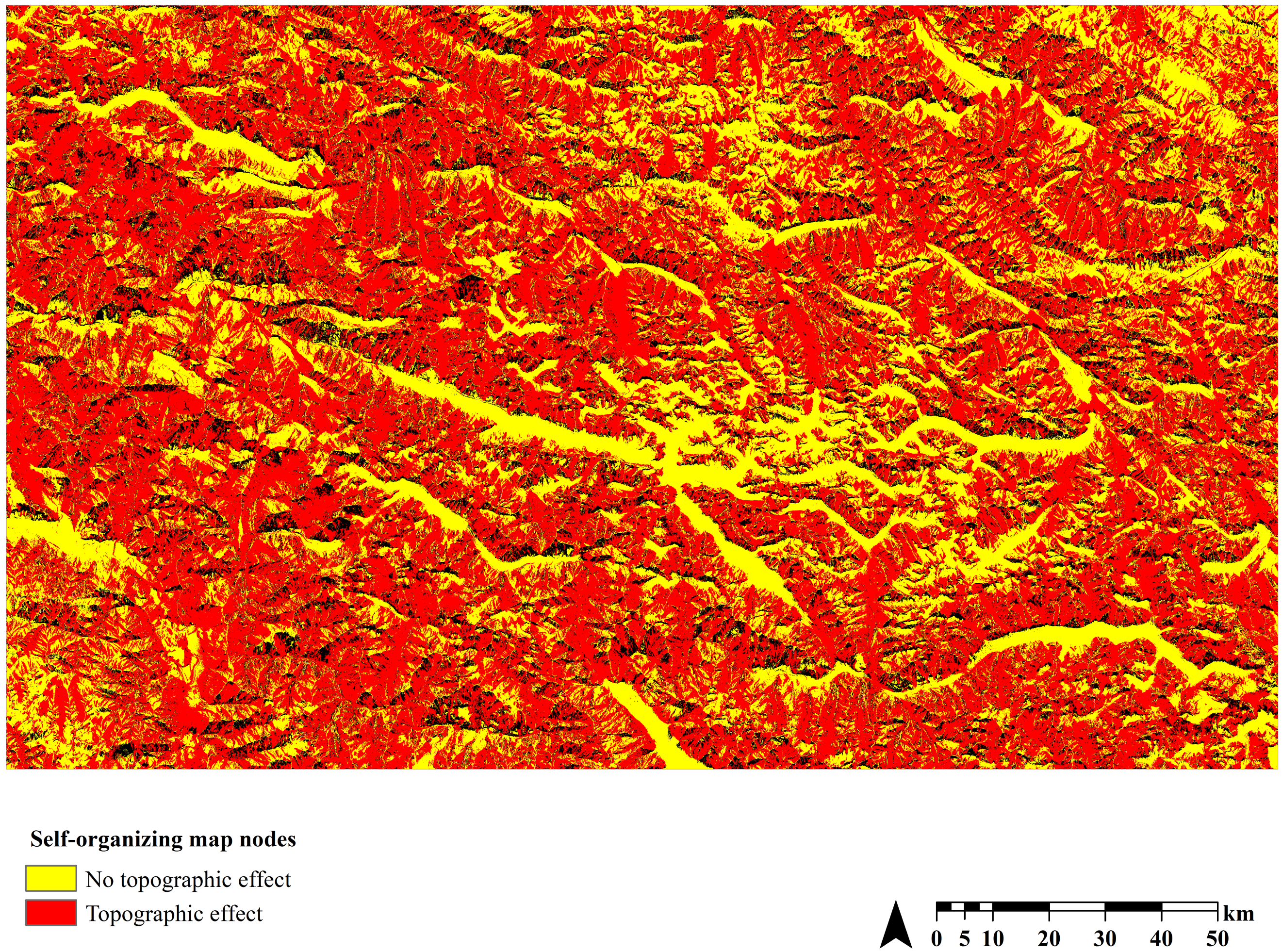

Figure 4.16: A map of combined kurtosis patterns.

the means of the surface irradiance for different groups of glaciers is statistically different.

4.6 Logistic regression analysis of glacier state

Logistic regression (logit regression) has previously been used to study environmental controls on surge type glaciers (Jiskoot et al., 1998, 2000; Barrand and Murray, 2006). Logistic regression estimates what the probabilities are for a binary or a multivariate response based on any number of predictor variables. In this study, a logistic regression with each characterization variable was performed, and the variables with significant coefficients are accepted as a statistically significant control on the probability of surge type glacier. Each significant variable is discussed in the context of process and form, as well as its relationship to glacier dynamics.

Logistic regression is a type of a generalized linear model that utilizes a logit function and categorical outcome variables. The categorical variable could be binary or with three or more values (Dayton, 1992; Meyers et al., 2016). The model does not predict the outcome but instead models the probabilities of an outcome. And specifically, the model estimates the logarithm of the odds (or log-odds) for the outcome being 1 or 0.

The equation of the model is as follow:

$$logit(p) = \beta_0 + \beta_1 * predictor \tag{4.91}$$

The odds ratio is derived by taking the exponent of the coefficient of the predictor variable. Odds ratio greater than one indicates that there is a positive relationship between predictor and outcome, and odds ration less than one indicates a negative relationship. Standard p-value threshold of 0.05 is used to determine if a model is significant or not.

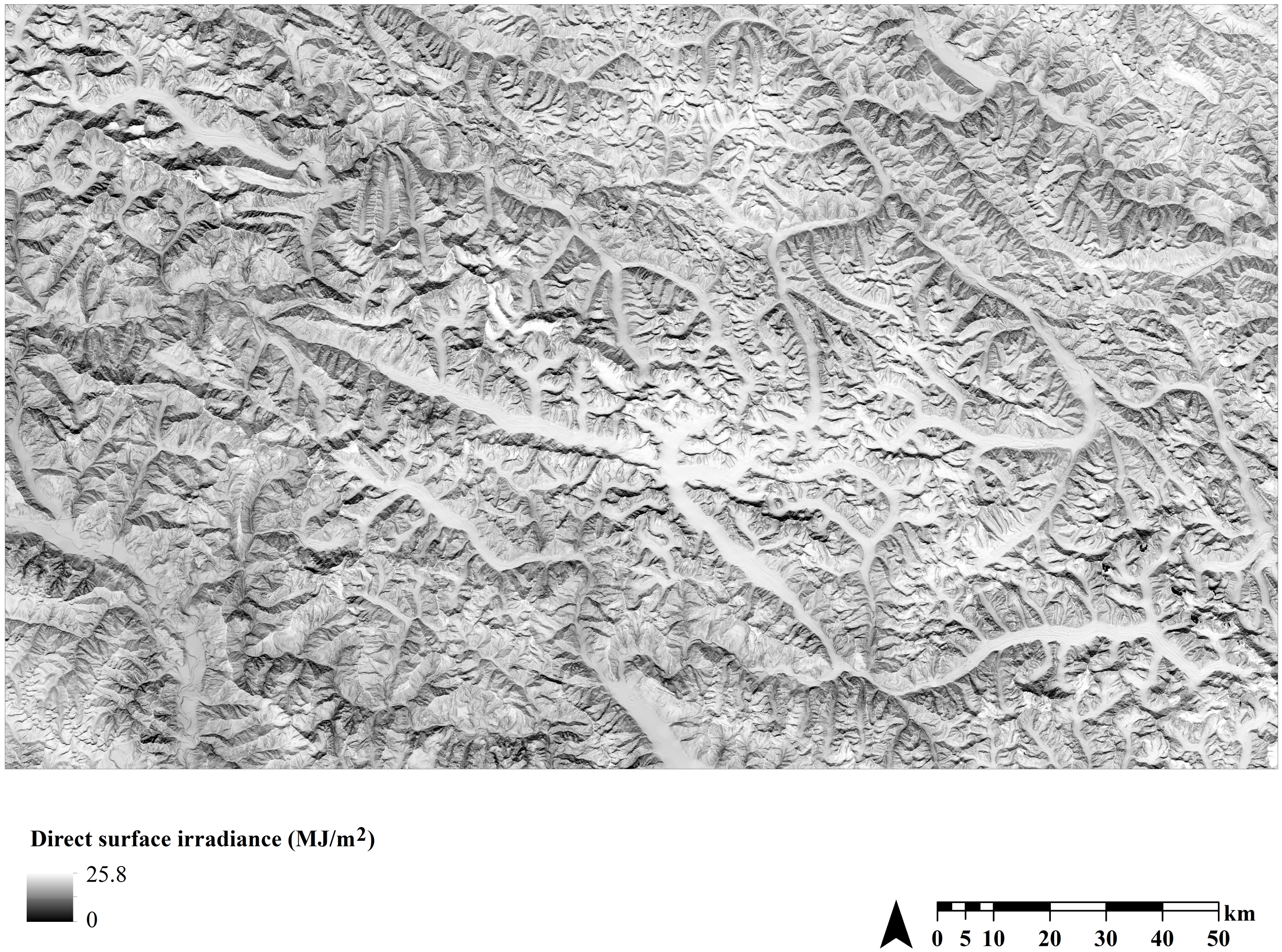

Figure 4.17: Direct surface irradiance averaged over the ablation season.

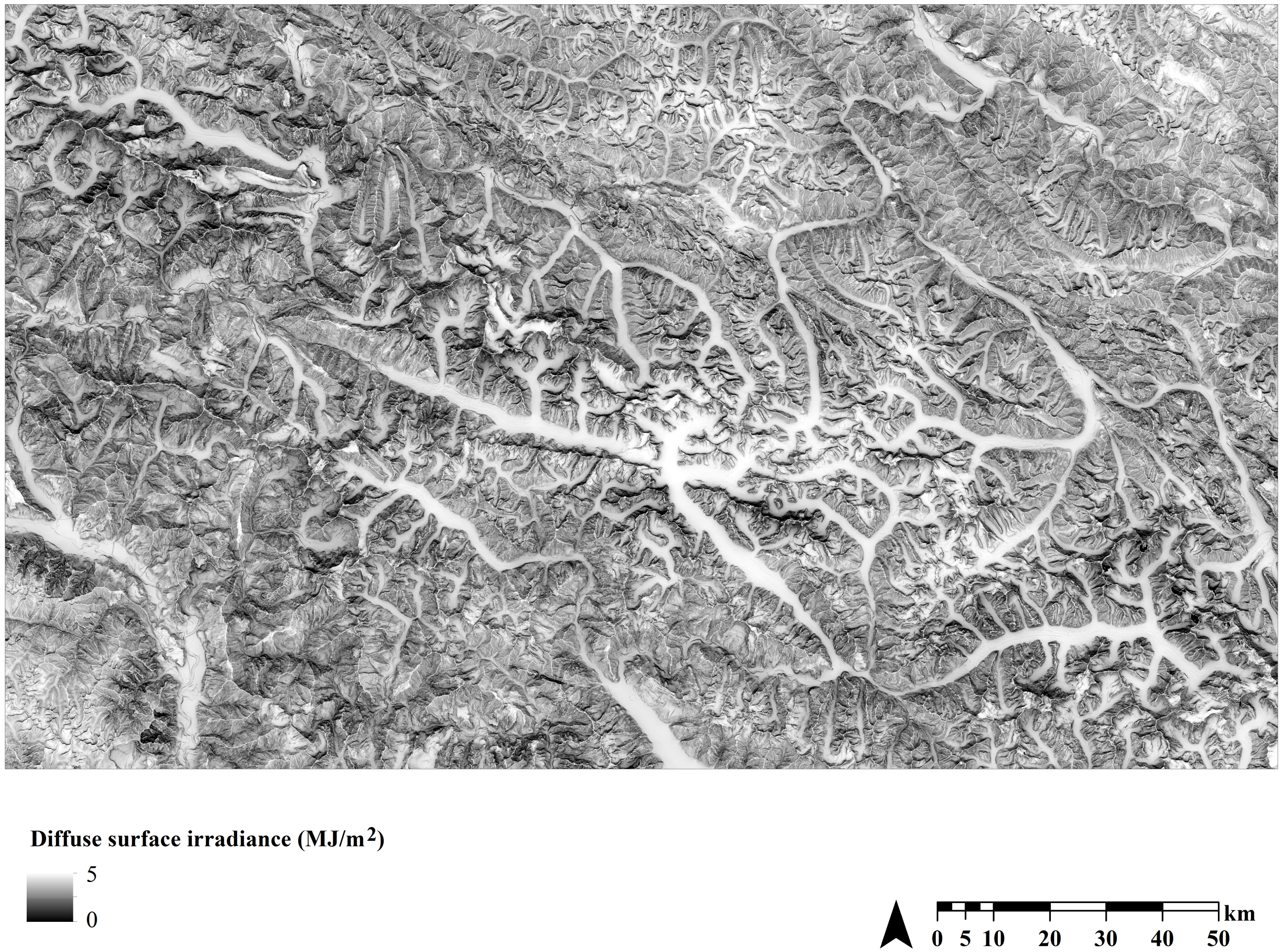

Figure 4.18: Diffuse surface irradiance averaged over the ablation season.

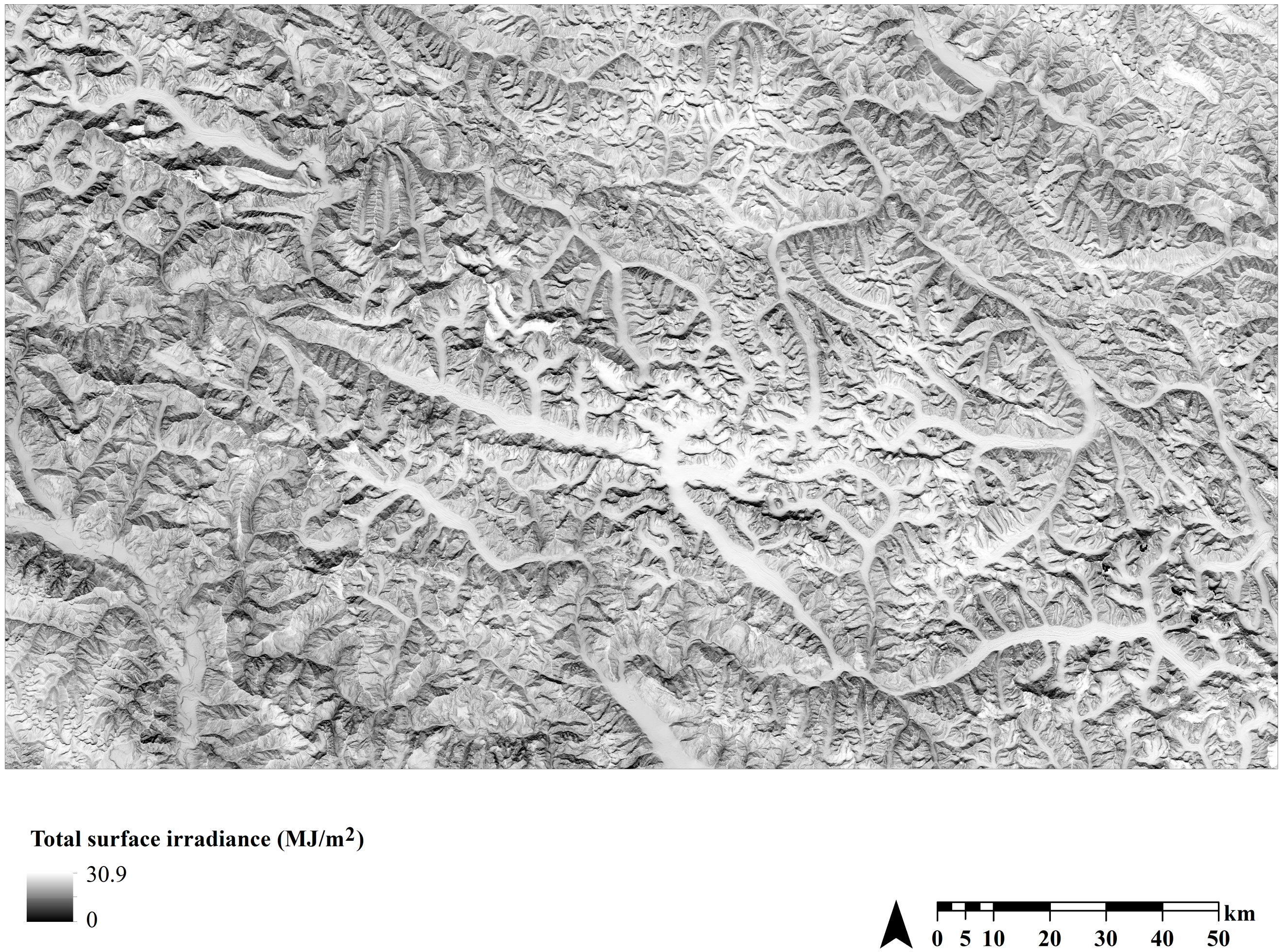

Figure 4.19: Total surface irradiance averaged over the ablation season.

5. RESULTS

5.1 Solar radiation modeling: point validation

The most important evaluation of solar radiation models is comparison to measurements. The measured solar radiation at NREL stations provides the means to evaluate the models; however, only for flat terrain conditions. With this stipulation, the relationship between measured and simulated solar radiation are presented.

The total and direct components of simulated solar radiation by STSRM and QGIS are similarly related to the respective measured components. The simulations of both models account for 98% of the total measured irradiance and 96% of the direct measured irradiance with a relatively low RMSE of 1.2 MJ/m^2 and 1.6 MJ/m^2 for total and direct irradiance, respectively (Table 5.1). Graphs of the measured and simulated irradiance show that STSRM simulations slightly underestimate the measured solar irradiance (Figure 5.1). The ArcGIS simulations, however, show very similar explained variance to the other two models, but also a very high RMSE of 7.8 MJ/m^2 and 8.6 MJ/m^2 for total and direct irradiance, respectively.

Table 5.1: Relation between solar radiation measurements and simulations.

Model	Solar Radiation Component	R^2	RMSE
STSRM	Total	0.988	1.27
ArcGIS	Total	0.976	7.82
QGIS	Total	0.987	1.16
STSRM	Direct	0.963	1.67
ArcGIS	Direct	0.949	8.59
QGIS	Direct	0.956	1.68
STSRM	Diffuse	0.612	0.65
ArcGIS	Diffuse	0.511	1.12
QGIS	Diffuse	0.586	1.23

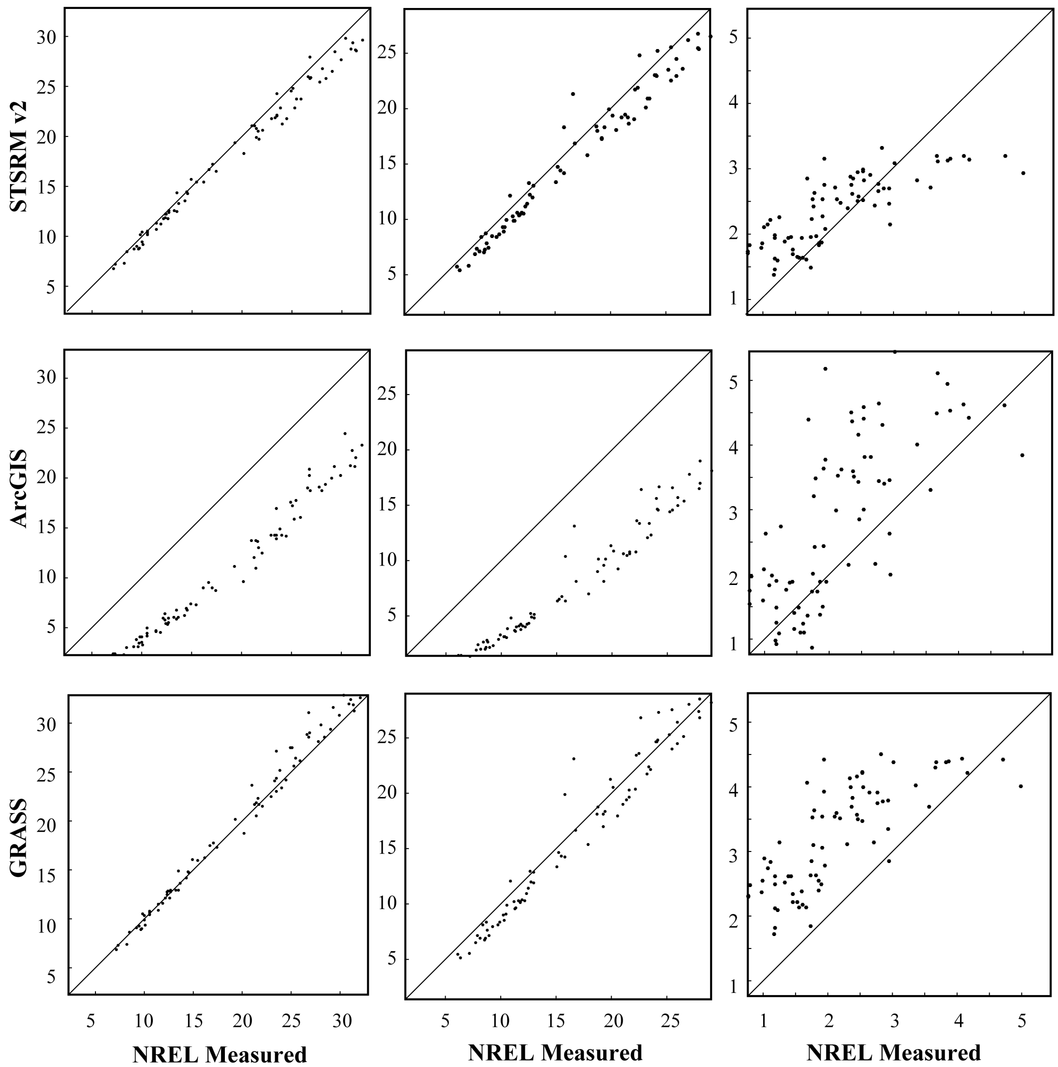

Figure 5.1: Correlations between measured and simulated solar radiation.

All three GIS-based solar radiation models underperform with respect to diffuse solar irradiance which is expected as the diffuse irradiance is affected by variations in atmospheric conditions such as water vapor and aerosols. For these configurations of the three GIS-based solar radiation models, STSRM performs slightly better than the other two models with explained variance of 61 % and RMSE of 0.65 MJ/m^2. It should be noted that STSRM performs better for lower values of diffuse irradiance than for higher values (Figure 5.1).

5.2 Solar radiation modeling: comparison to other models

Maps of total, direct, and diffuse solar radiation simulations through the three models are presented in Figure 5.2. These maps illustrate that the three models produced simulations with different magnitude, but also with different spatial patterns. For STSRM the magnitude of the simulations is important, atmopsheric attenuation is varied as a function of altitude and solar zenith angle (Table 4.6), with the exception of aerosol attenuation for which we implemented the Ångstrøm turbidity formula (Ångström, 1930; Muhammad Iqbal, 1983). Thus the atmospheric attenuation (except for aerosols) is controlled by the location of the study and the time of year.

In contrast, the solar radiation models within ArcGIS and QGIS are easily adjusted to produce different magnitudes of solar radiation by varying the transmissivity (ArcGIS) or the Linke turbidity coeffiecient (QGIS) parameters used to simulate different overall cloud cover (ArcGIS) or different atmospheric (QGIS) conditions. Still, by examining the solar radiation simulations maps (Figure 5.2) and histograms of the simulated solar radiation components (not shown), we see that, for the set of solar radiation parameters and the specified study area and date, QGIS produces the highest magnitude of direct irradiance, with STSRM being a close second. Since, we do not have measurements over this study area and for the spatial resolution of the input DEM (30 m), we can only compare the

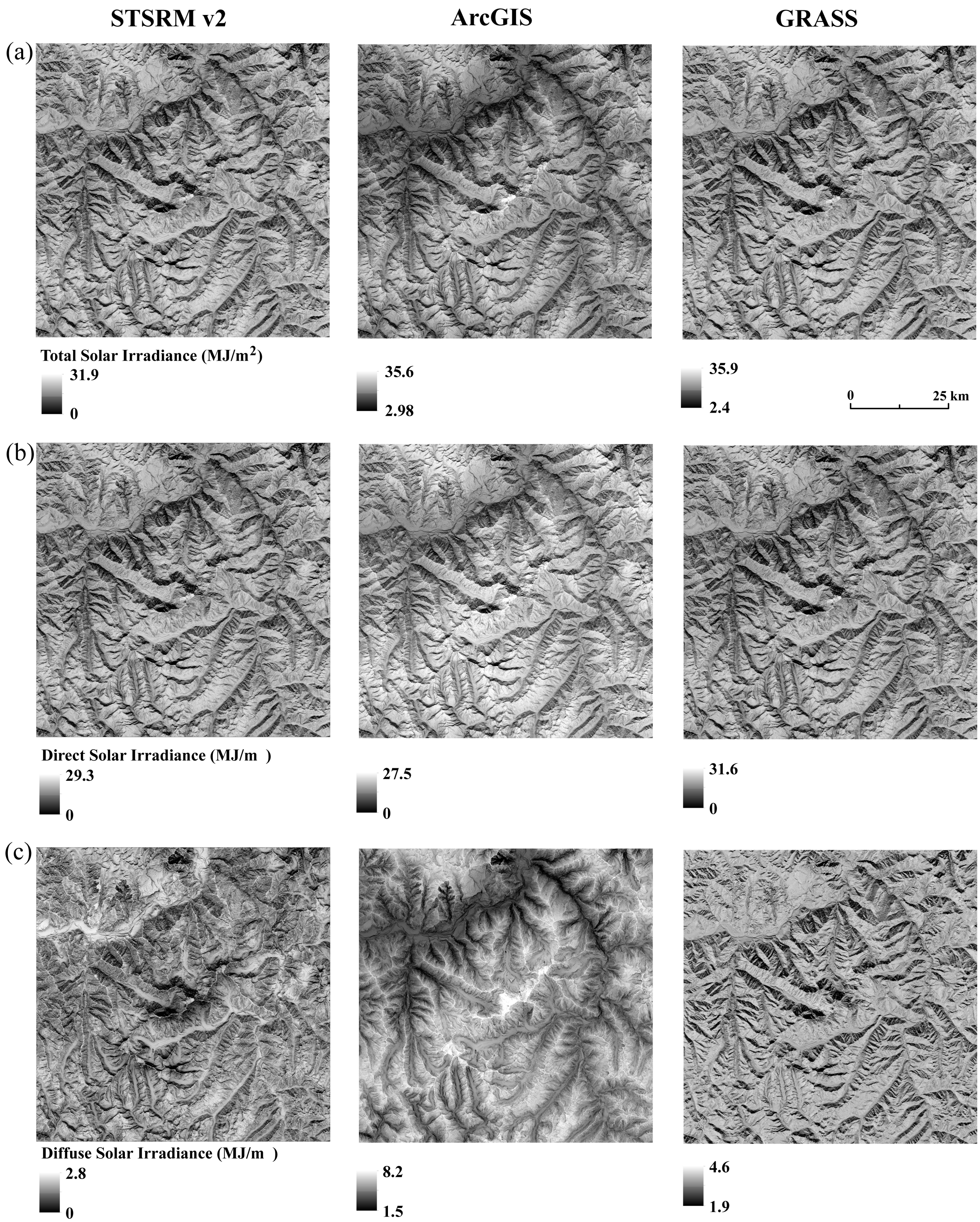

Figure 5.2: Solar radiation simulations.

simulations from the three solar radiation models, but without assessing which of the three is more accurate.

In terms of diffuse irradiance, ArcGIS produces the simulations with highest magnitude (average of 4.9 MJ/m), QGIS - second (average of 3.9 MJ/m), and STSRM - third (average of 2.1 MJ/m). It should also be noted that the values of direct and diffuse irradiance simulated by QGIS are skewed to the left (negative skew), which means that the model produces solar radiation values concentrated towards higher solar irradiance. The direct solar irradiance of STSRM is also skewed to the left but not as much as that of QGIS.

Further insight into the similarities and differences between the solar radiation simulations of the three models is explored through difference maps (Figure 5.3) and - correlations with terrain parameters - in particular elevation, terrain slope, sine and cosine of terrain aspect, skyview factor, and cosine of the incidence angle (Tables 5.2 and 5.3). The greatest correlation is in the difference between STSRM and ArcGIS of diffuse irradiance (80% explained variability); similarly, the difference between ArcGIS and QGIS is also well correlated with elevation (57% explained variability). This shows that, in terms of diffuse irradiance, STSRM and QGIS incorporate elevation similarly within calculations of diffuse irradiance, but both models differ from ArcGIS in this respect. On the other hand, the difference of diffuse irradiance between STSRM and QGIS relates most to the skyview factor (explained variability of 39%), but also to terrain slope and the cosine of terrain aspect with explained variability of 23% and 21%, respectively. Likewise, the differences of direct irradiance between STSRM and ArcGIS, and between QGIS and ArcGIS, are similarly related to elevation and to the cosine of the incidence angle, with explained variance between 33% and 22% (Tables 5.2 and 5.3).

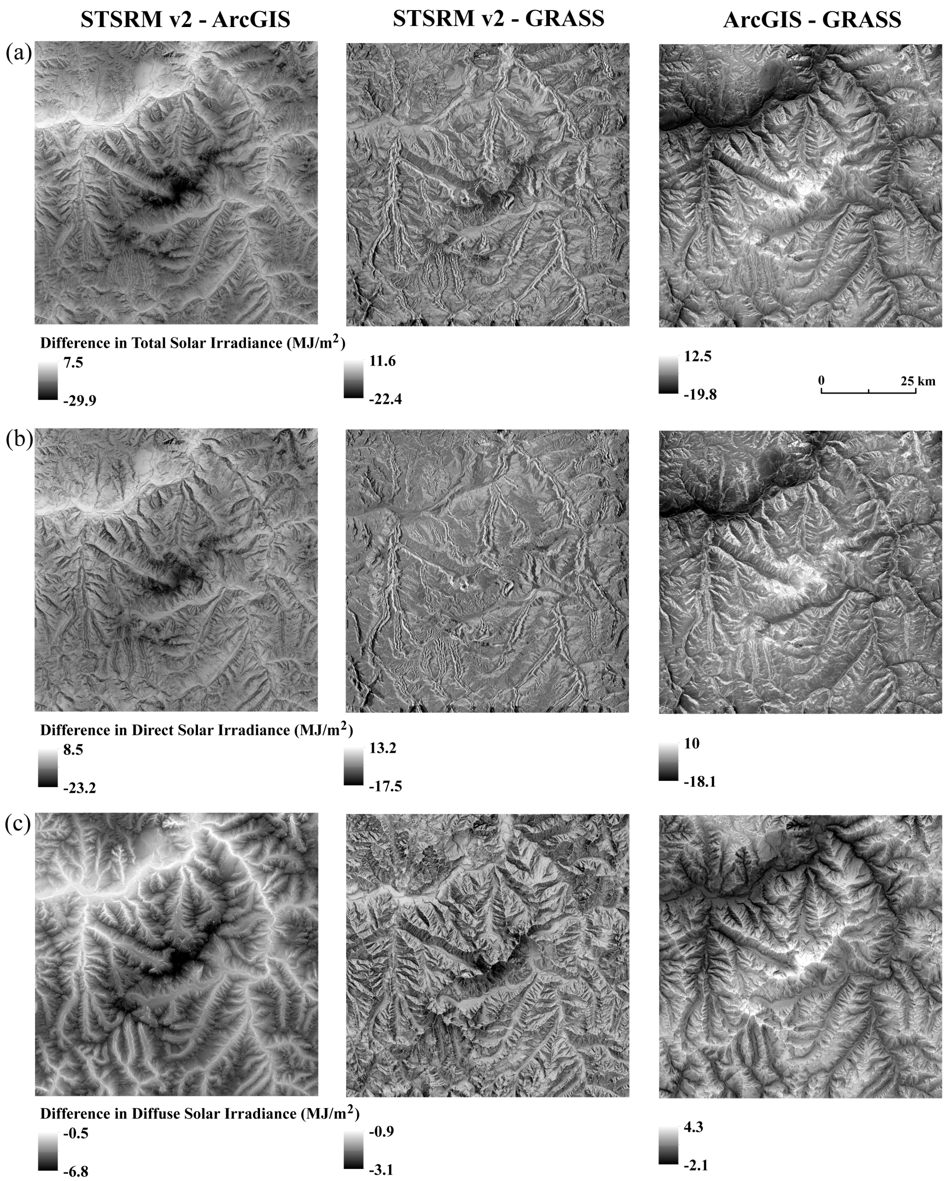

Figure 5.3: Differences in solar radiation simulations.

Table 5.2: Relation between direct solar irradiance differences and terrain parameters. These correlations are significant.

Independent Variable	Dependent Variable	R^2	removed outliers
Cosine of incidence angle	ArcGIS and QGIS	0.326	11
Elevation	**STSRM and ArcGIS**	**0.299**	**2**
Cosine of incidence angle	**STSRM and ArcGIS**	**0.232**	**2**
Elevation	ArcGIS and QGIS	0.227	11
Terrain slope	ArcGIS and QGIS	0.156	11
Skyview	ArcGIS and QGIS	0.149	11
Skyview	**STSRM and ArcGIS**	**0.142**	**2**
Cosine of terrain aspect	ArcGIS and QGIS	0.142	11
Terrain slope	**STSRM and ArcGIS**	**0.107**	**2**
Cosine of terrain aspect	**STSRM and ArcGIS**	**0.099**	**2**
Cosine of incidence angle	*STSRM and QGIS*	*0.093*	*9*

Table 5.3: Relation between diffuse solar irradiance differences and terrain parameters. These correlations are significant.

Independent Variable	Dependent Variable	R^2	removed outliers
Elevation	**STSRM and ArcGIS**	**0.814**	**4**
Elevation	ArcGIS and QGIS	0.565	1
Skyview	*STSRM and QGIS*	*0.386*	*4*
Terrain slope	*STSRM and QGIS*	*0.231*	*4*
Cosine of terrain aspect	*STSRM and QGIS*	*0.207*	*4*
Skyview	ArcGIS and QGIS	0.175	1
Cosine of terrain aspect	ArcGIS and QGIS	0.109	1

Table 5.4: Results for all significant models.

Variable	% not surge type	% surge type	B	Exp(B)	P-value
Maximum altitude (km)	71.4	53.7	1.131	3.098	0
Relief (km)	73.2	48.8	0.514	1.672	0.002
Planimetric area (km^2)	92.9	61	0.04	1.041	0
Surface area (km^2)	92.9	61	0.033	1.034	0
Slope averaged along centerline (degrees)	78.6	65.9	-0.314	0.73	0
Slope averaged over glacier area (degrees)	71.4	39	-0.11	0.896	0.02
Length (km)	85.7	65.9	0.178	1.195	0
Branchiness index	87.5	31.7	0.328	1.388	0.002
Perimeter (km)	87.5	56.1	0.01	1.011	0
Shape index (x 10^4)	76.8	63.4	-0.059	0.943	0
Catchment planimetric area (km^2)	89.3	58.5	0.01	1.01	0
Catchment surface area (km^2)	85.7	58.5	0.01	1.01	0
Catchment relief (km)	78.6	39	0.356	1.428	0.036
Catchment perimeter (km)	89.3	63.4	0.047	1.048	0
Catchment shape index (x 10^5)	75	65.9	-0.038	0.963	0
Debris covered area km^2	91.1	46.3	0.133	1.142	0.001
Kurtosis ratio	85.7	29.3	0.642	1.901	0.038
Average total irradiance (MJ/m^2)	75	53.7	0.389	1.476	0.006

5.3 Surge type glacier characterization

Logistic regression results for all significant variables and a list of the non significant variables are presented in Figures 5.4 and 5.5. To assist with the interpretation of these results, maps of each variable and the probability of surge type glacier or no-surge type glacier are presented (Figures 5.6 through Figure 5.23) . These results will be discussed in the next chapter, but a brief summary follows.

Table 5.4 presents results of logistic regression with a single variable on the response

Table 5.5: List of all insignificant models.

Variable
Altitude of terminus
Minimum altitude
Mean altitude
Hypsometric interval
Cosine of aspect averaged along centerline
Sine of aspect averaged along centerline
Cosine of aspect averaged for total area
Sine of aspect averaged for total area
Catchment hypsometric interval
Catchment skyview averaged over total area
Debris cover as a percent over total glacier area

of a surge type glacier (1) or not a surge type glacier (0). These results were obtained using IBM SPSS Statistics. Reported are the coefficient (B) of the logistic regression equation in log-odds unit. There is only one coefficient reported, as only one independent variable at a time was analyzed. Also reported are the odds ratios ($Exp(B)$) of the derived coefficients, and the probability value or asymptotic significance (p-value) of the coefficients. P-value is reported to three decimal places, so a p-value of 0 is a p-value smaller than 0.001.

The table also reports the percentage of glaciers predicted correctly as surge type or non-surge type, given the estimated logistic regression for each independent variable. Note that the equation coefficients were calculated based on the whole dataset, and the whole dataset is also used to calculate these percentages. Still, the probability of a glacier being classified as one or the other type is important, because it shows how typical a glacier is for its category. In other words, the probability of a glacier being classified as one type or the other is an indication of the interactions between each independent variable as well as glacier dynamics. Maps showing these probabilities along with the values of the independent variable are presented in Figures 5.6 through Figure 5.23.

The results show that the geomorphic variables that increase the probability of a glacier being a surge type are maximum altitude of the glacier, the glacier and catchment relief, the glacier and catchment planimetric and surface area, glacier and catchment perimeter, glacier length and branchiness index. Geomorphic variables that decrease this probability are slope averaged along the glacier centerline or over the total area of the glacier, and the shape index of glacier and catchment. A note in the discussion on the use of the parametrization of shape index requires additional look at this variable and maps of shape index for glaciers (Figure 5.4) and catchment (Figure 5.5) are presented.

The percent of glacier covered by debris was not a significant independent variable through logistic regression on this set of surge type versus non-surge type glaciers. The total area of debris cover was significant, and it increases the probability of a glacier being a surge type similar to glacier planimetric and surface area.

With respect to the total irradiance and kurtosis ratio, both variables increase the probability of a glacier being a surge type. Increasing the amount of solar radiation received during the ablation season also increases the probability of a glacier being of surge type. In terms of the kurtosis ratio, increasing the topographic effect decreases the probability of surging. This is because increasing the kurtosis ratio means a decrease in topographic influence, and the logistic regression indicates that increasing the kurtosis ratio leads to an increase in the probability of a glacier being surge type. Thus both surface irradiance independent variables indicate that the greater the amount of solar radiation, the greater the probability of a glacier being surge type.

5.4 Advancing and retreating glacier characterization

The Karakoram glaciers database of Rankl et al. (2014) is utilized in this study to distinguish advancing and retreating glaciers (Figures 4.6 and 5.24) . There are seven glaciers identified as advancing and six identified as retreating within the glaciers selected for this study (Figure 5.24). Note that there is a seventh advancing glacier which is excluded as it

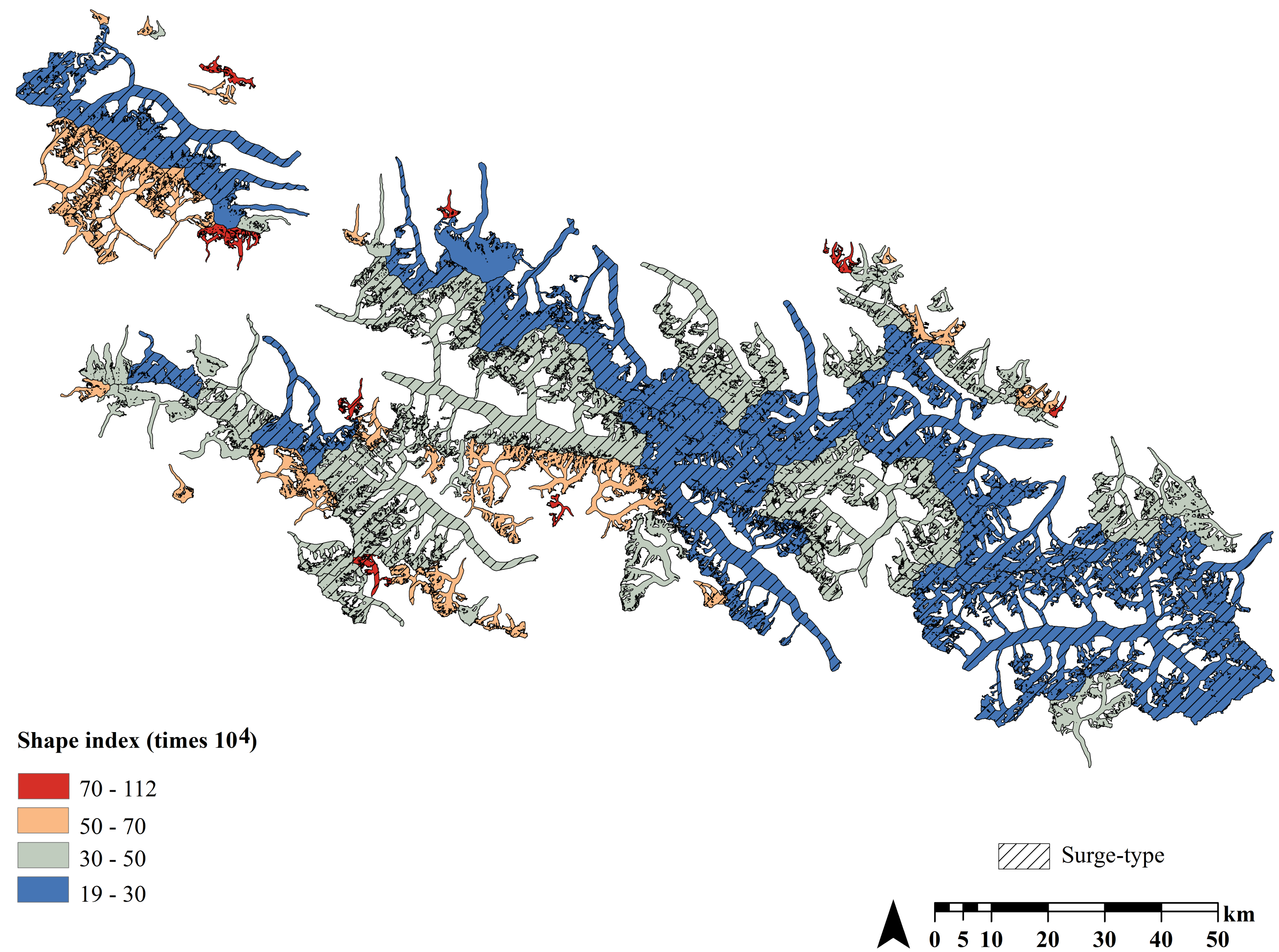

Figure 5.4: Map of shape index of glaciers.

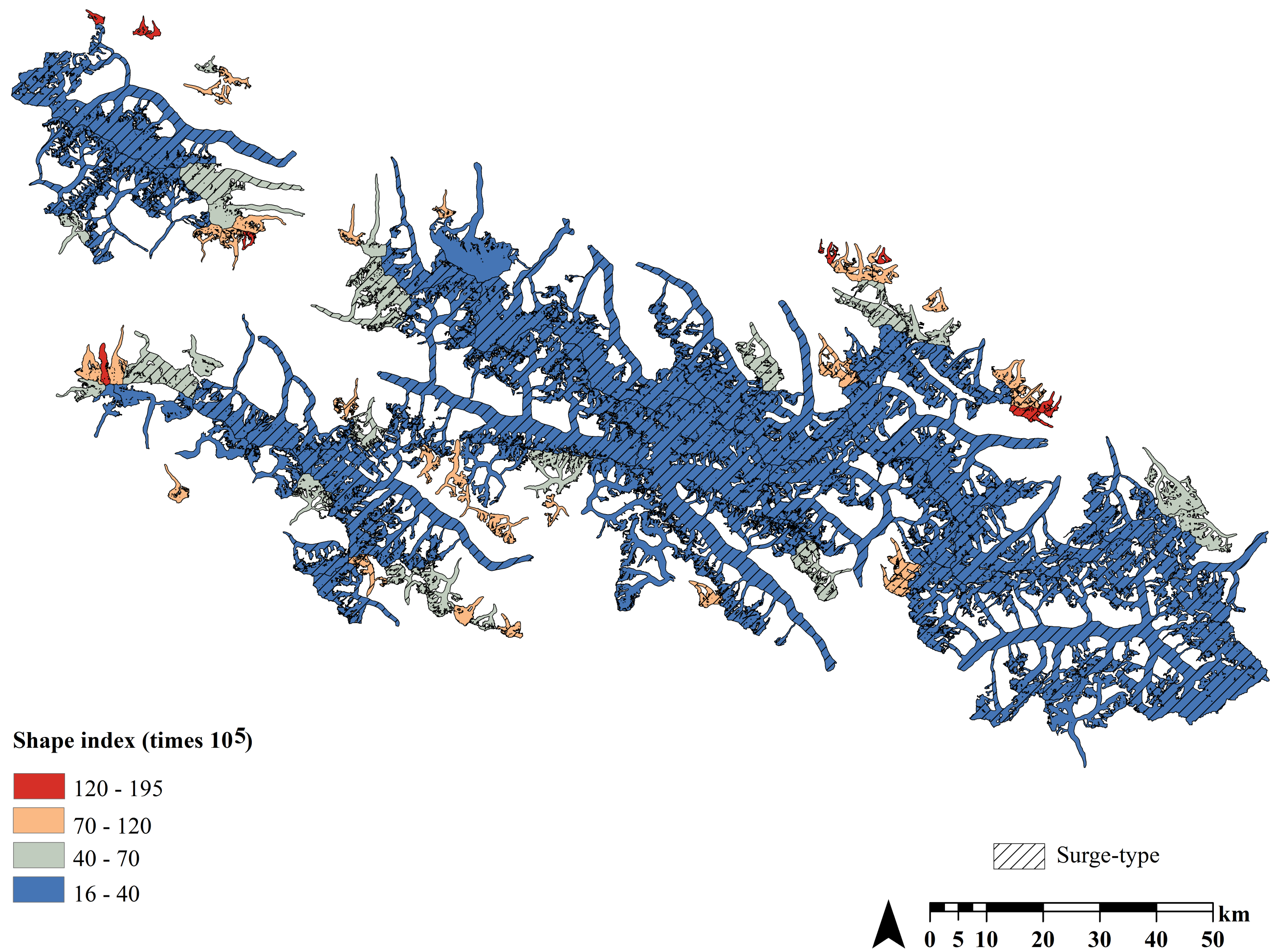

Figure 5.5: Map of shape index of catchments.

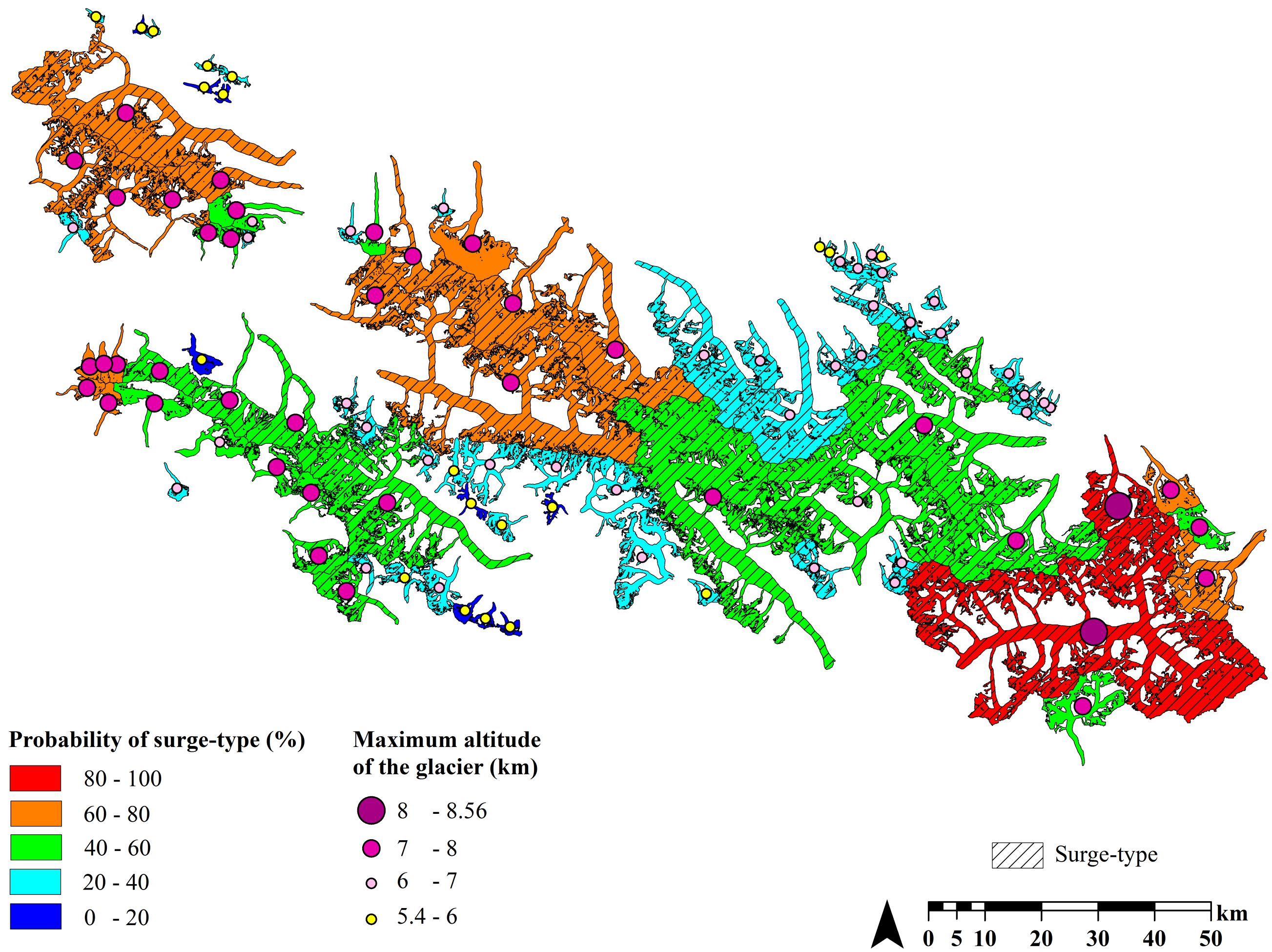

Figure 5.6: Results for maximum altitude of glaciers.

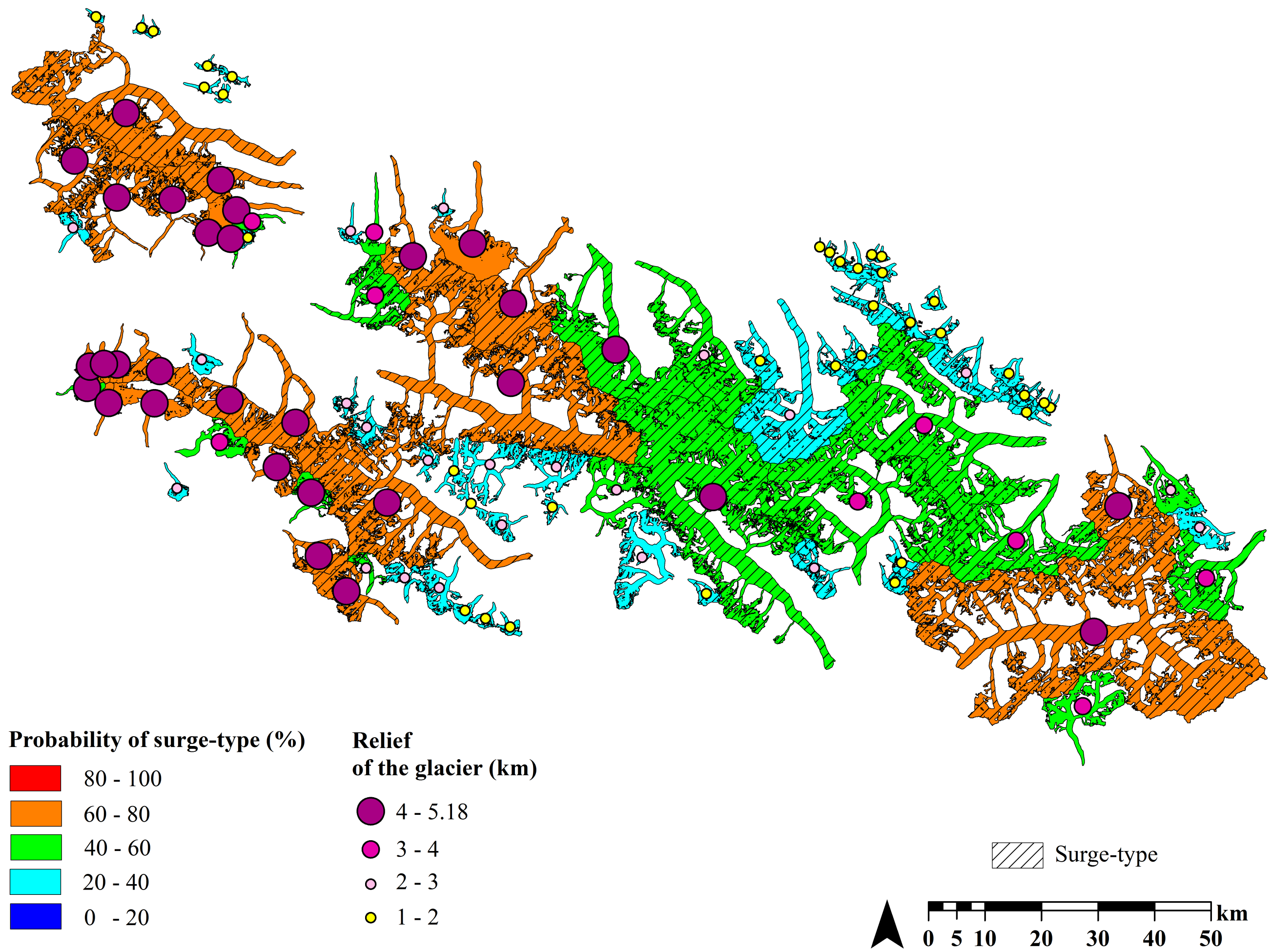

Figure 5.7: Results for relief of glaciers.

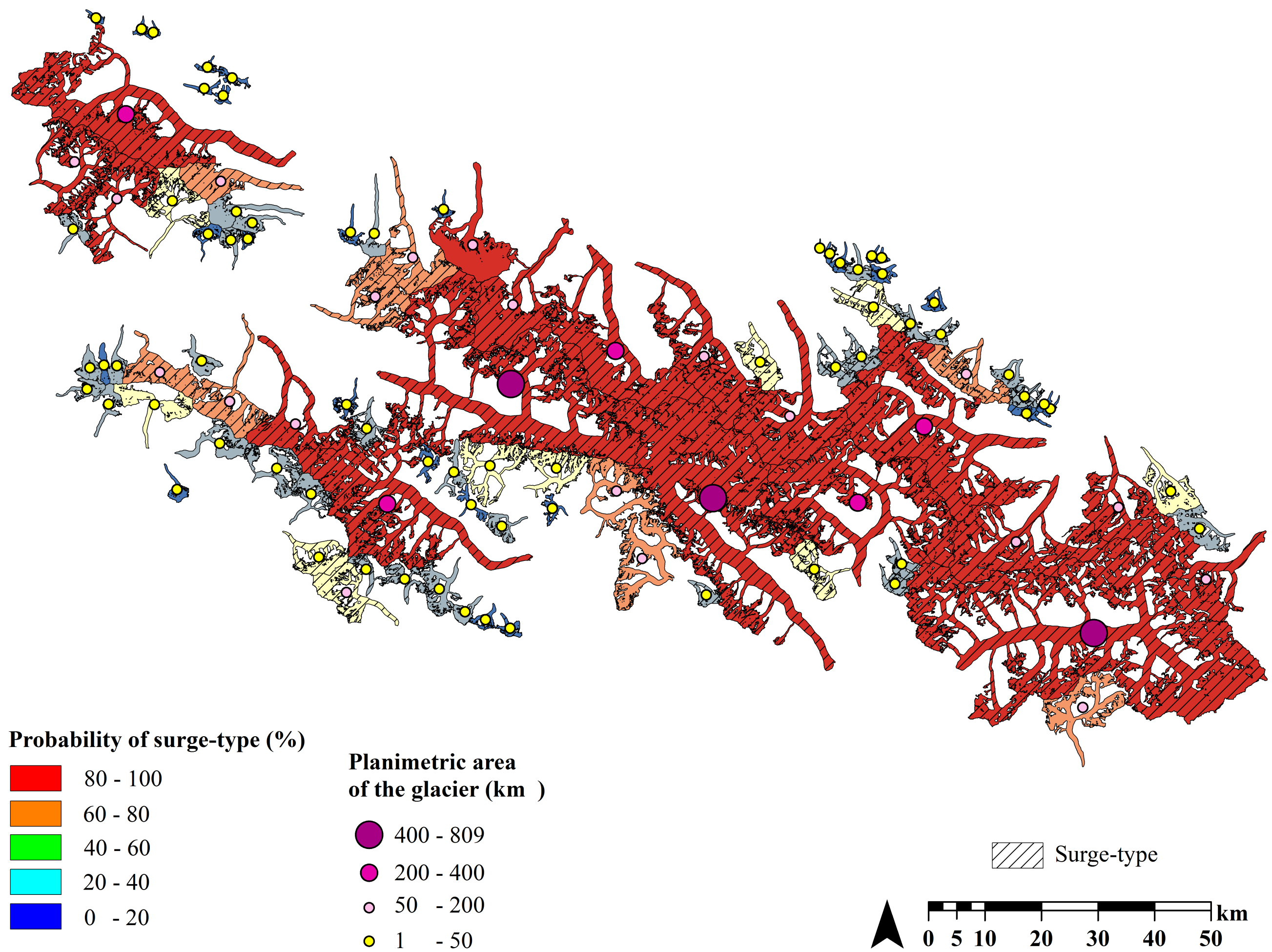

Figure 5.8: Results for planimetric area of glaciers.

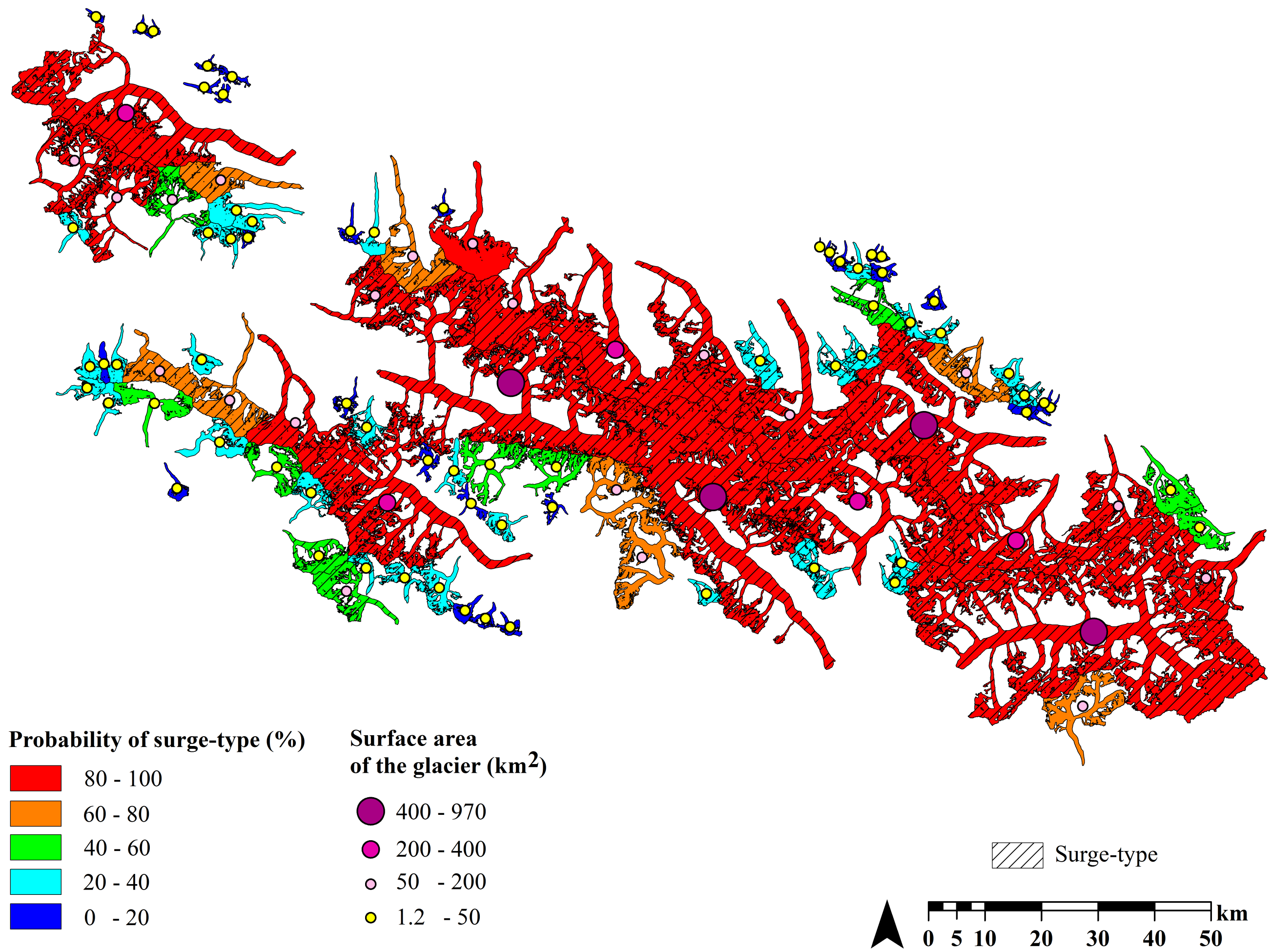

Figure 5.9: Results for surface area of glaciers.

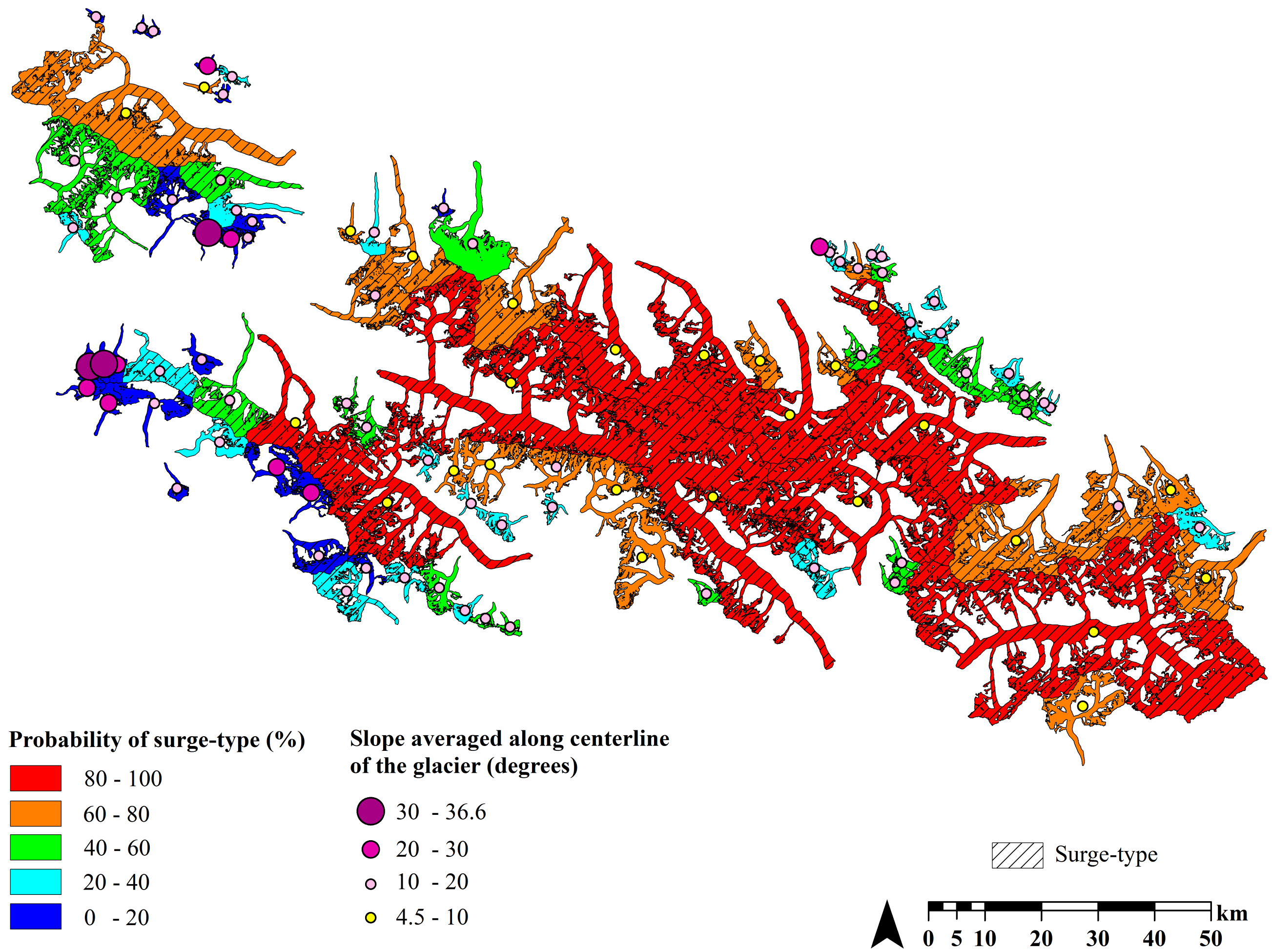

Figure 5.10: Results for slope averaged along the centerline of glaciers.

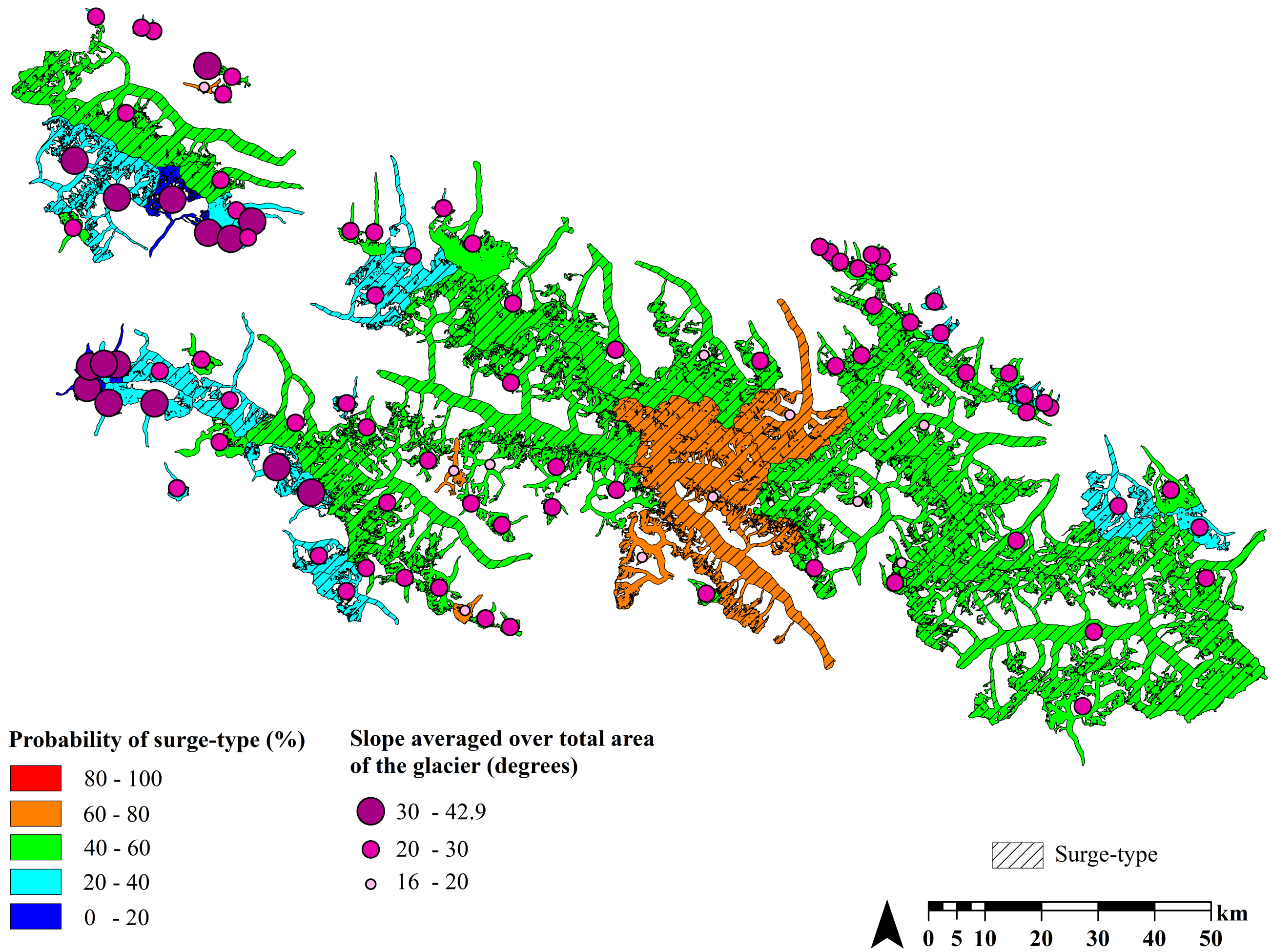

Figure 5.11: Results for slope averaged over the area of glaciers.

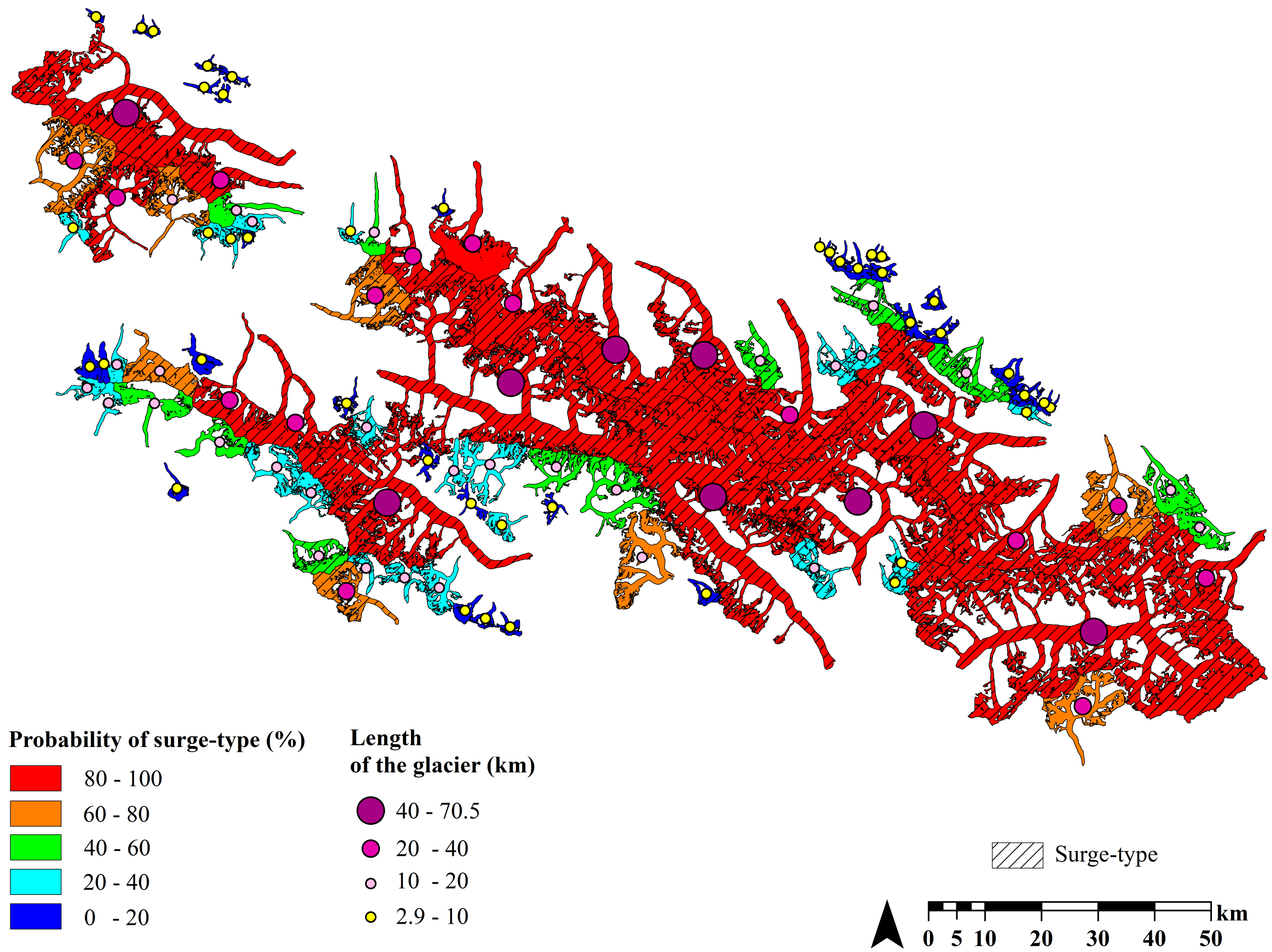

Figure 5.12: Results for length of glaciers.

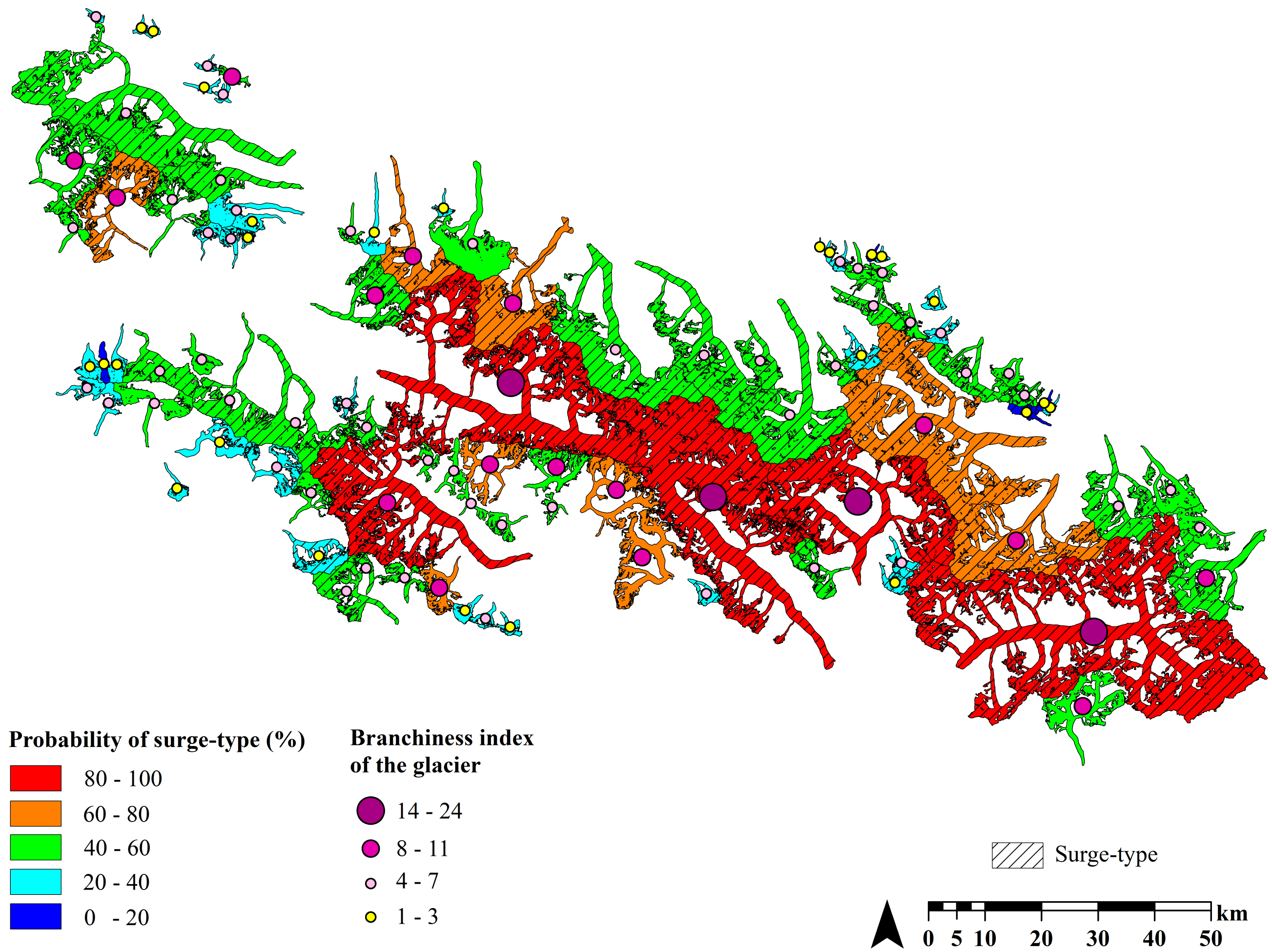

Figure 5.13: Results for branchiness index of glaciers.

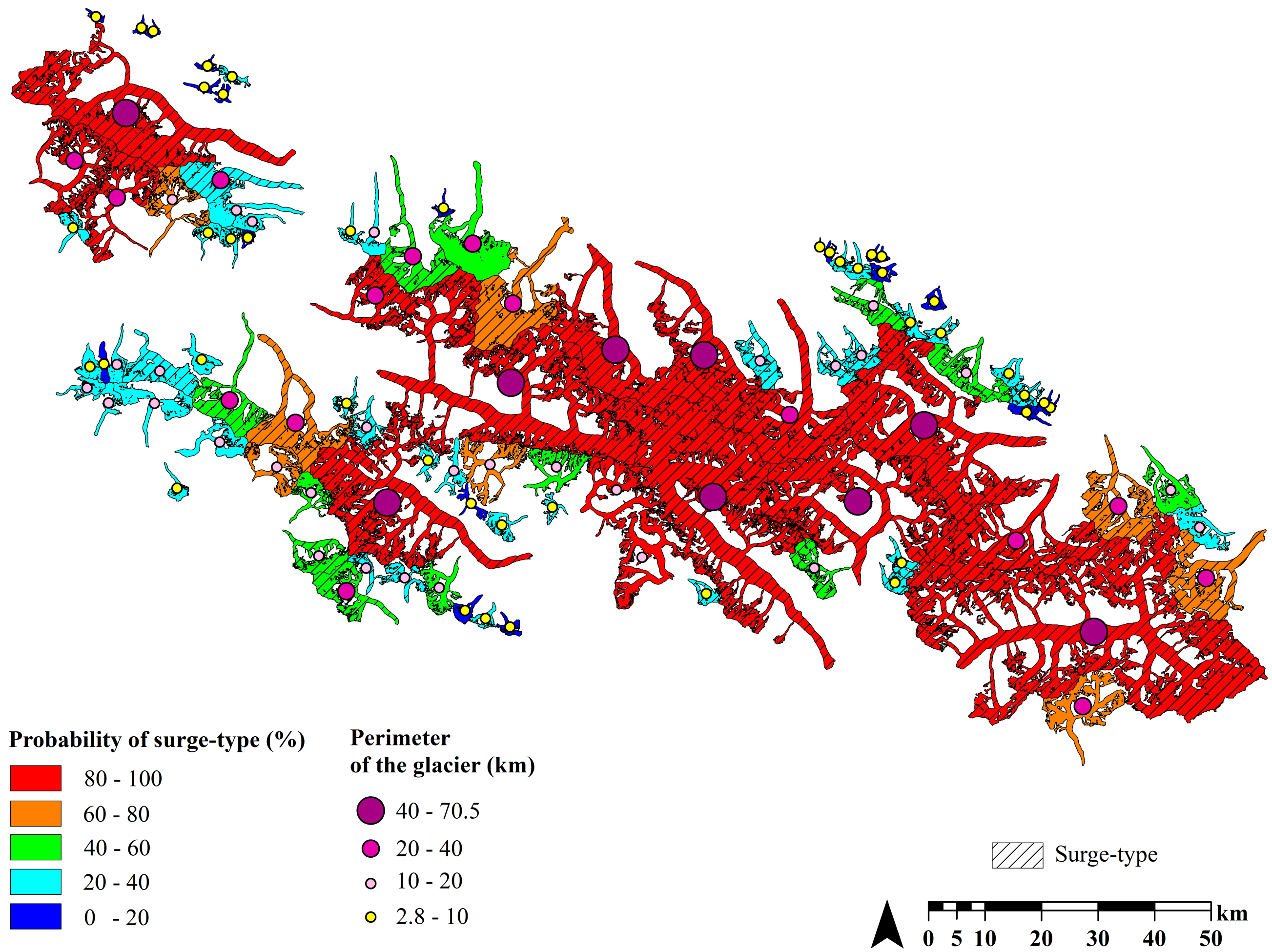

Figure 5.14: Results for perimeter of glaciers.

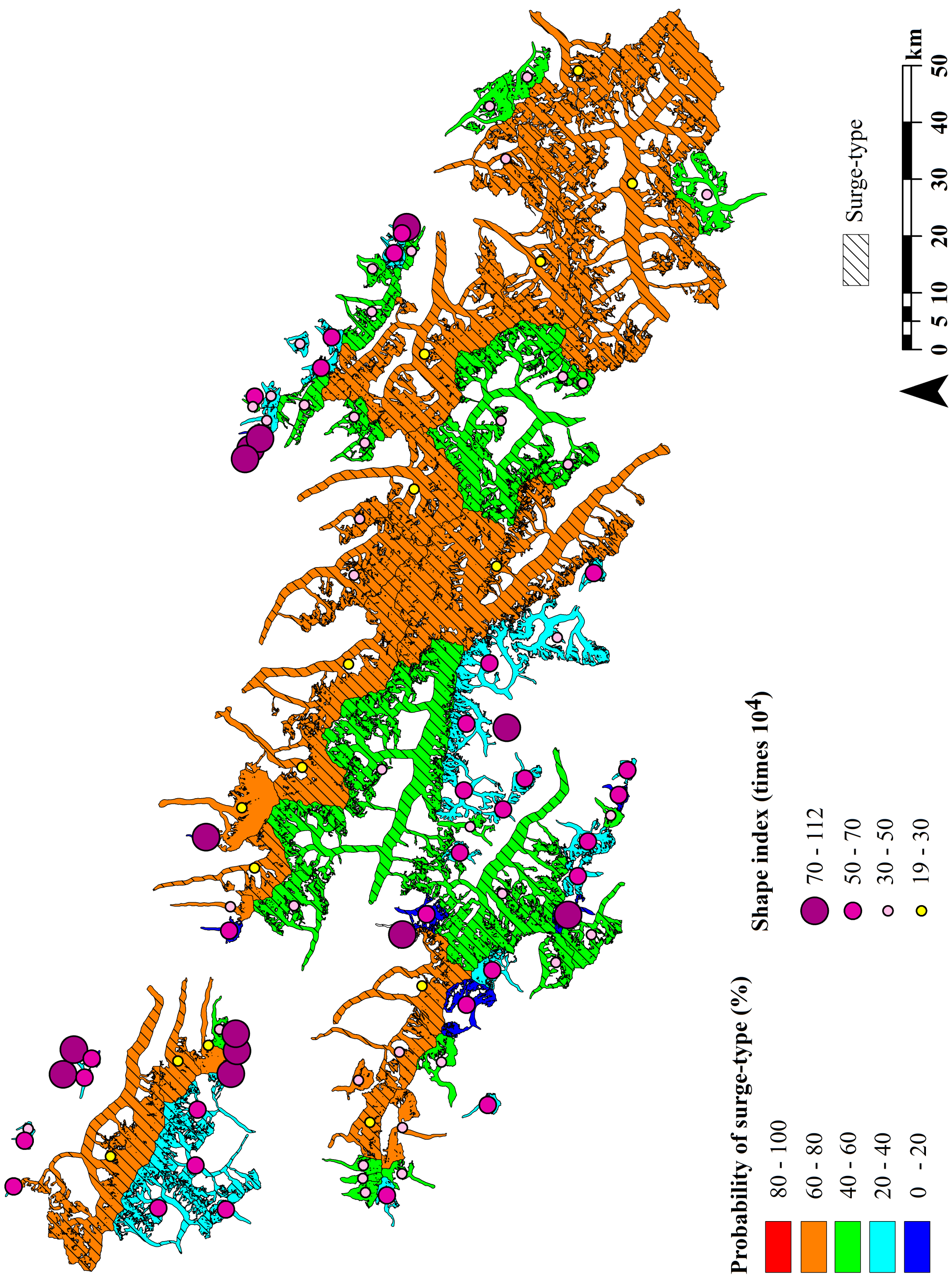

Figure 5.15: Results for shape index of glaciers.

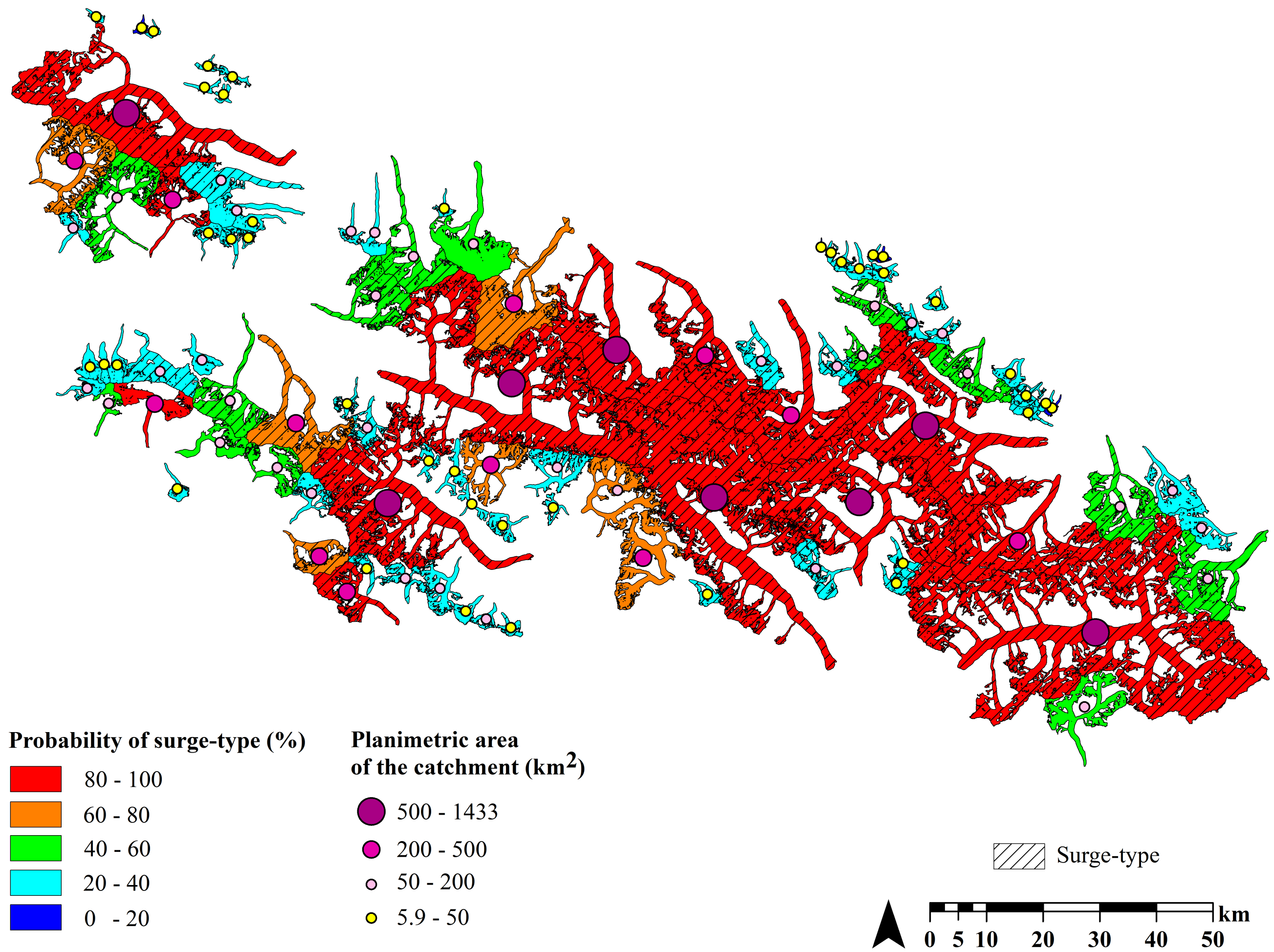

Figure 5.16: Results for planimetric area of catchments.

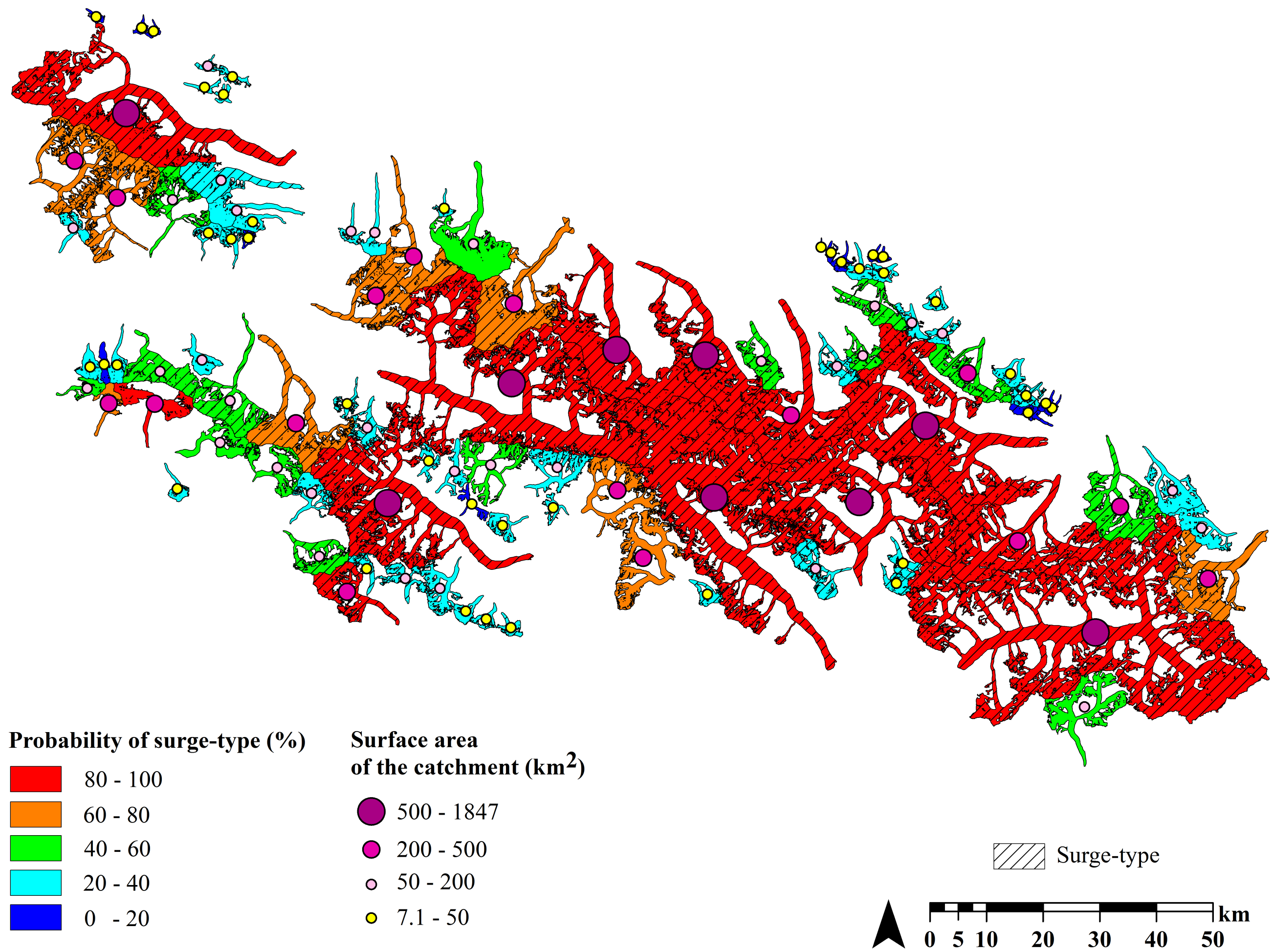

Figure 5.17: Results for surface area of catchments.

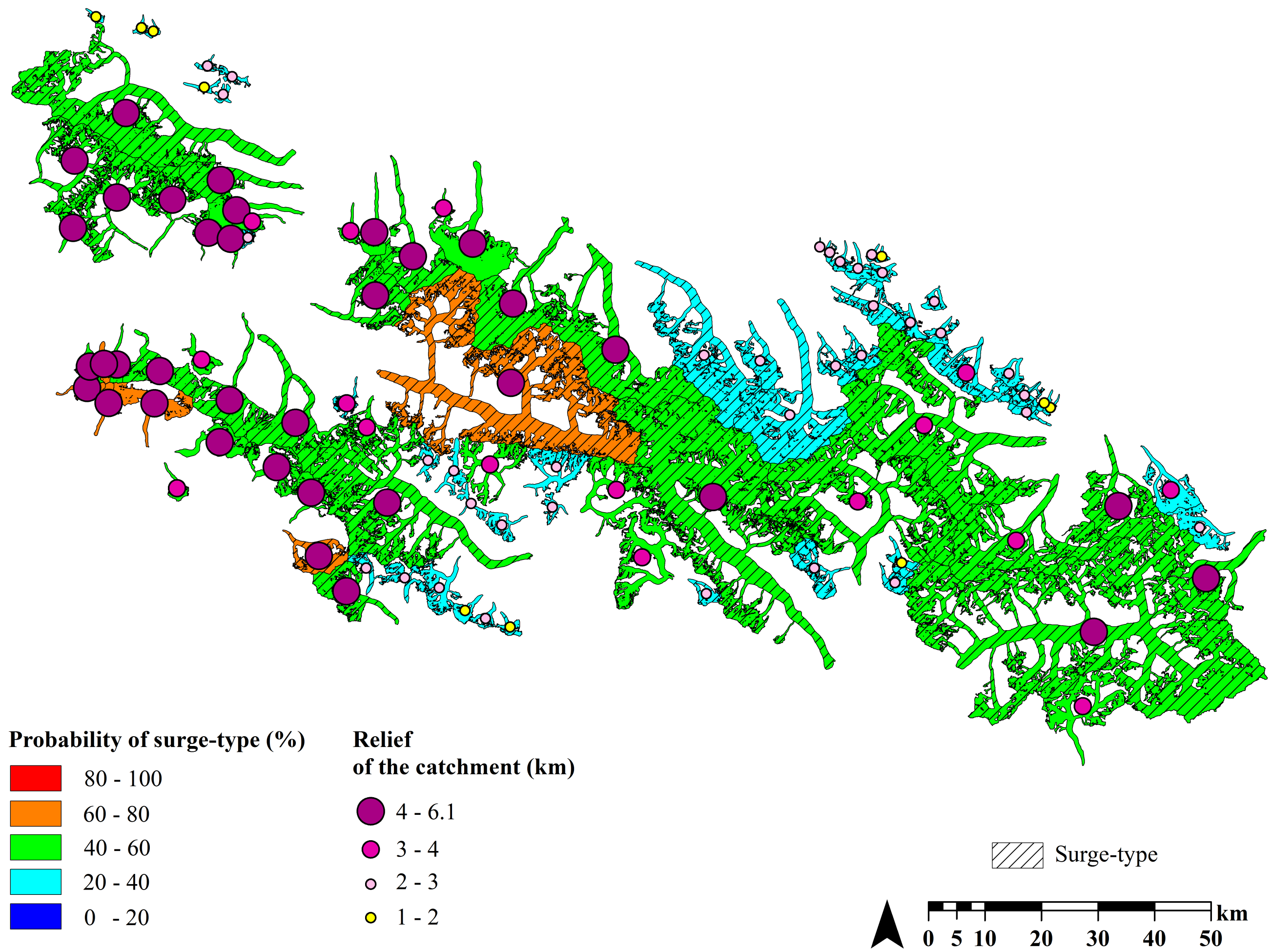

Figure 5.18: Results for relief of catchments.

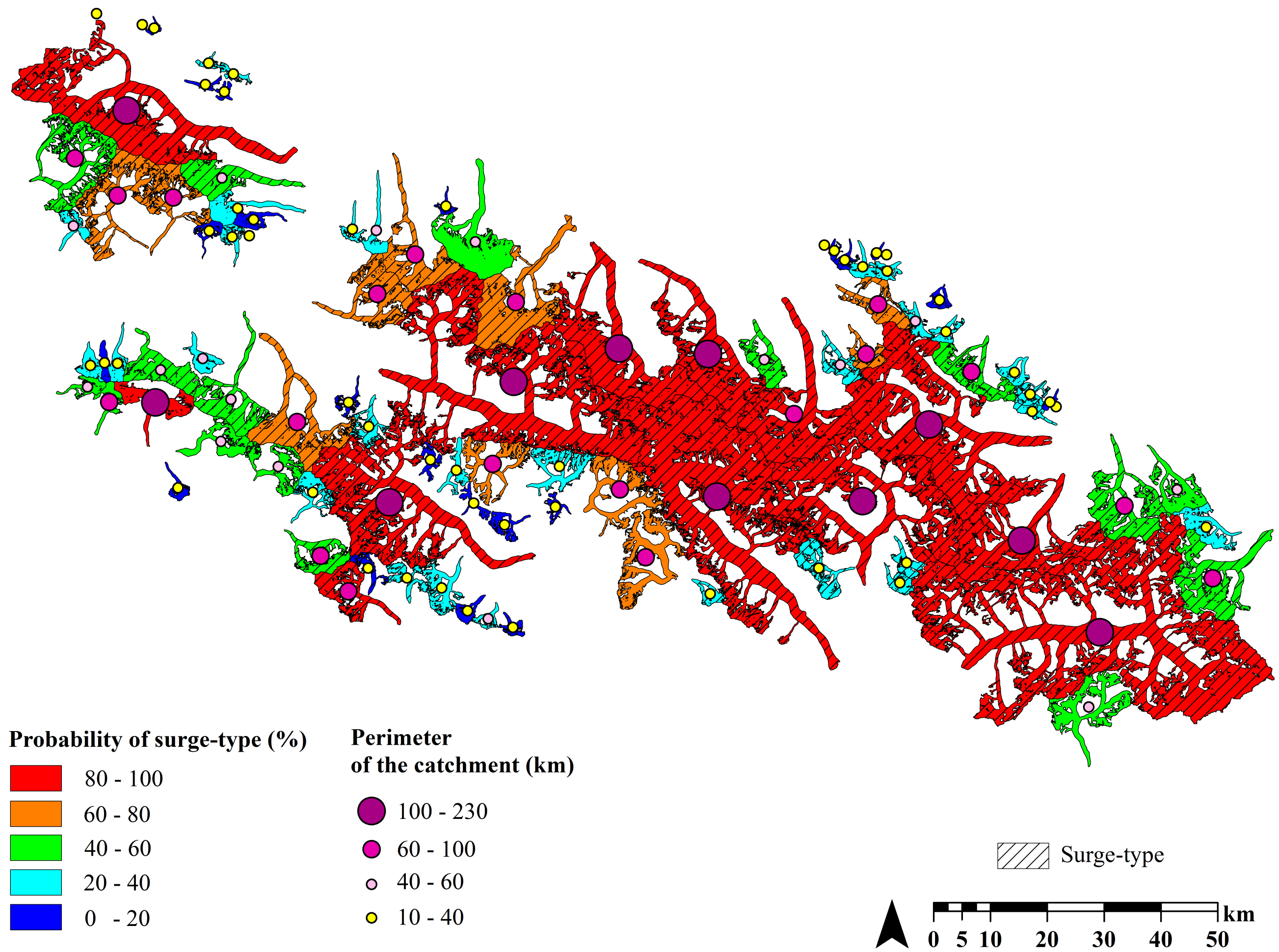

Figure 5.19: Results for perimeter of catchments.

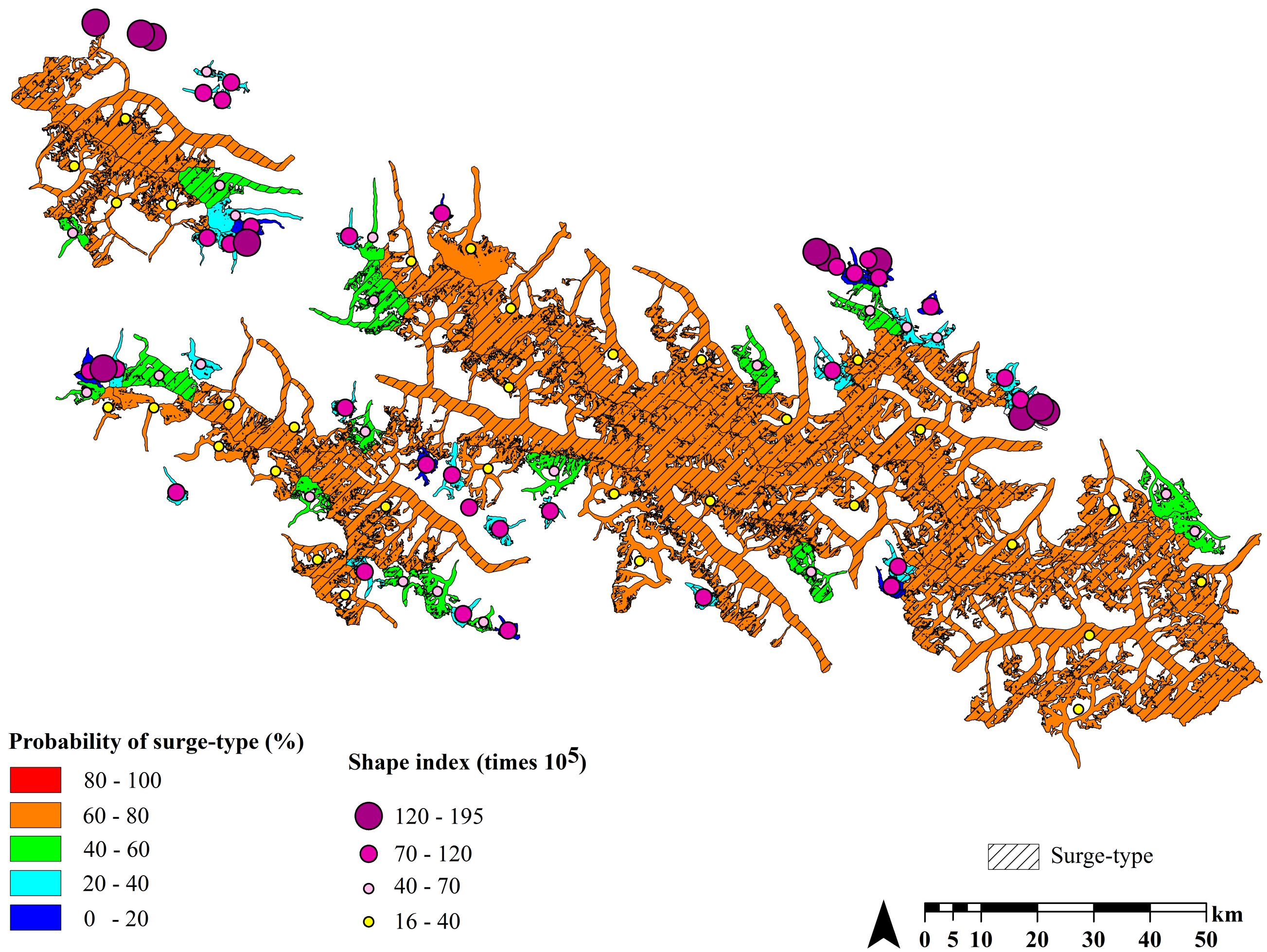

Figure 5.20: Results for shape index of catchments.

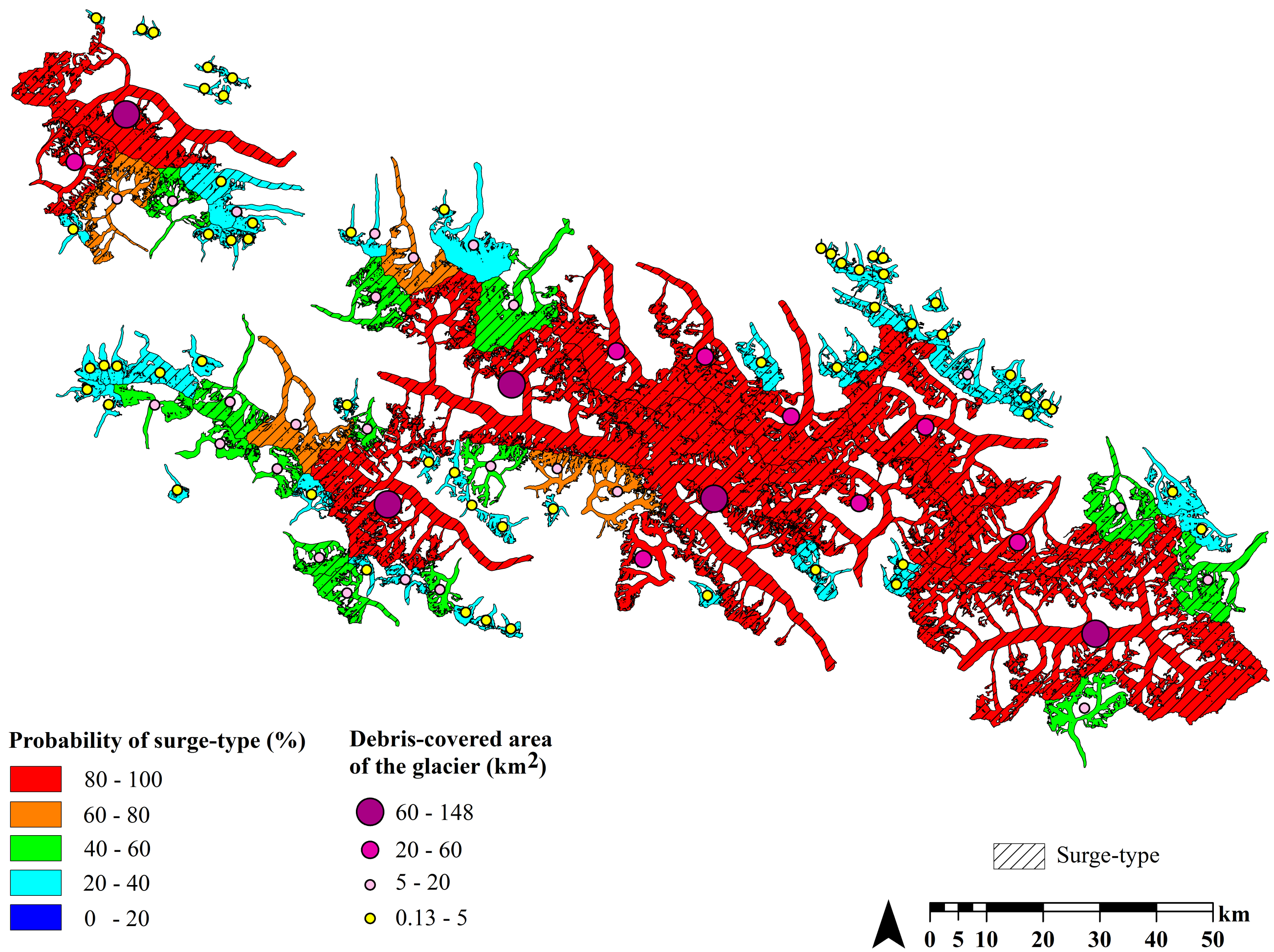

Figure 5.21: Results for debris cover area of glaciers.

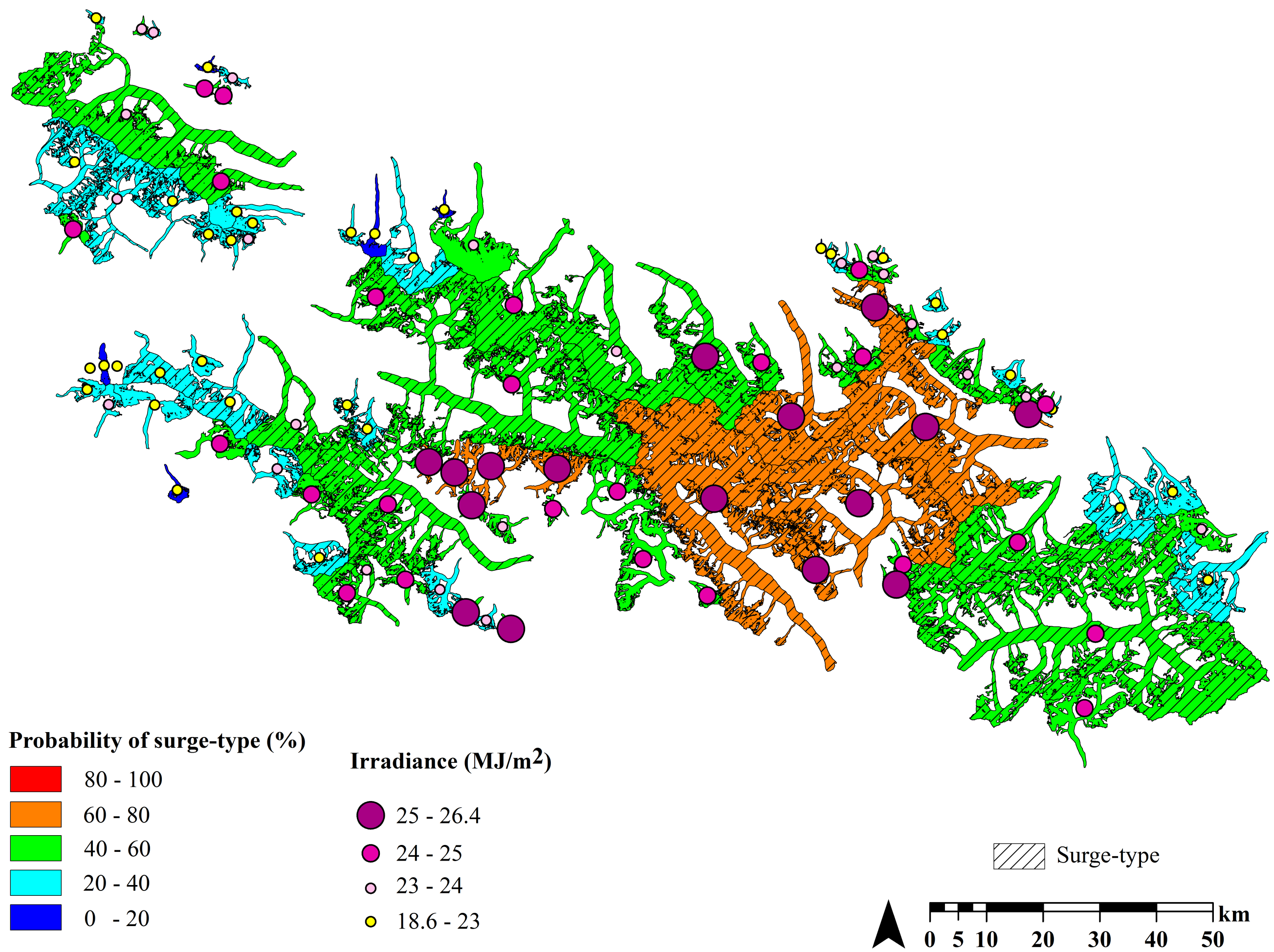

Figure 5.22: Results for average total irradiance over glaciers.

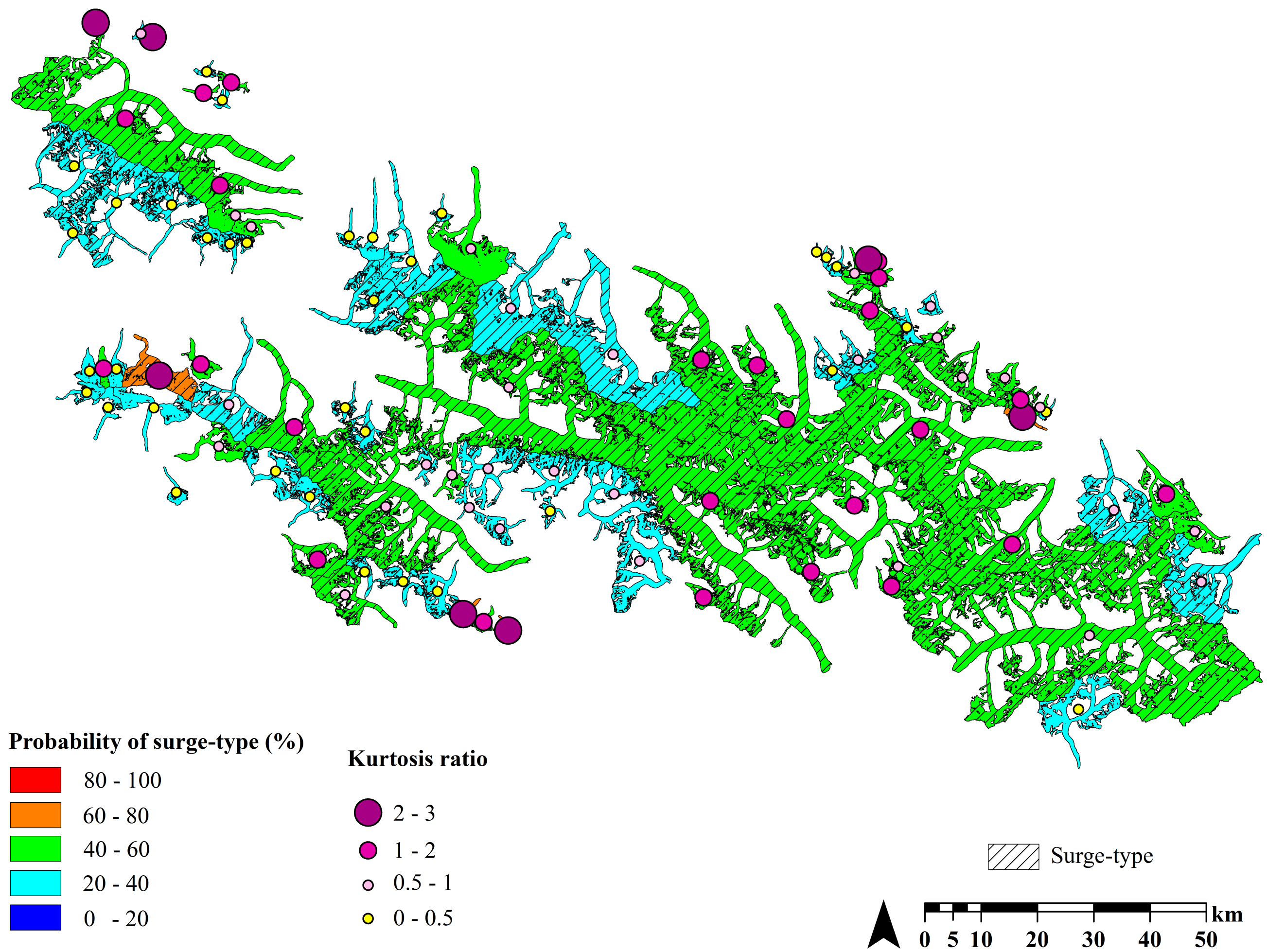

Figure 5.23: Results for kurtosis ratio over glaciers.

is a relatively small tributary of the Braldu glacier.

The map shows a clear locational difference between the two glacier categories. The retreating glaciers are located in the northeast of the study area, while the advancing glaciers are in the west. The advancing glaciers are small with an average area of 8 km^2, and the retreating are larger with an average area excluding Batura glacier as an outlier of 19.9 km^2. Batura itself is one of the largest glaciers on Earth with an area of 262 km^2 using the the shapefile in the Rankl et al. (2014) database.

All advancing glaciers are oriented north or slightly northeast/northwest. The sample of retreating glaciers does not exhibit a particular orientation, with glaciers being oriented in all directions. With respect to terrain slope, retreating glaciers are steeper with average slope of 22.8 degrees, while advancing glaciers are an average slope of 18.6 degrees (note that the slope difference is small).

There is little difference in the total irradiance received during the ablation season, with advancing glaciers averaging 23.9 MJ/m^2 and retreating glaciers averaging 23.5 MJ/m^2 total surface irradiance. However, there is a noticeable difference in the kurtosis ratio between the two glacier categories. Advancing glaciers have an average kurtosis ratio of 0.6 while retreating glaciers have a kurtosis ratio of 1.1, indicating much greater topographic influence on the surface irradiance of advancing glaciers than on retreating glaciers.

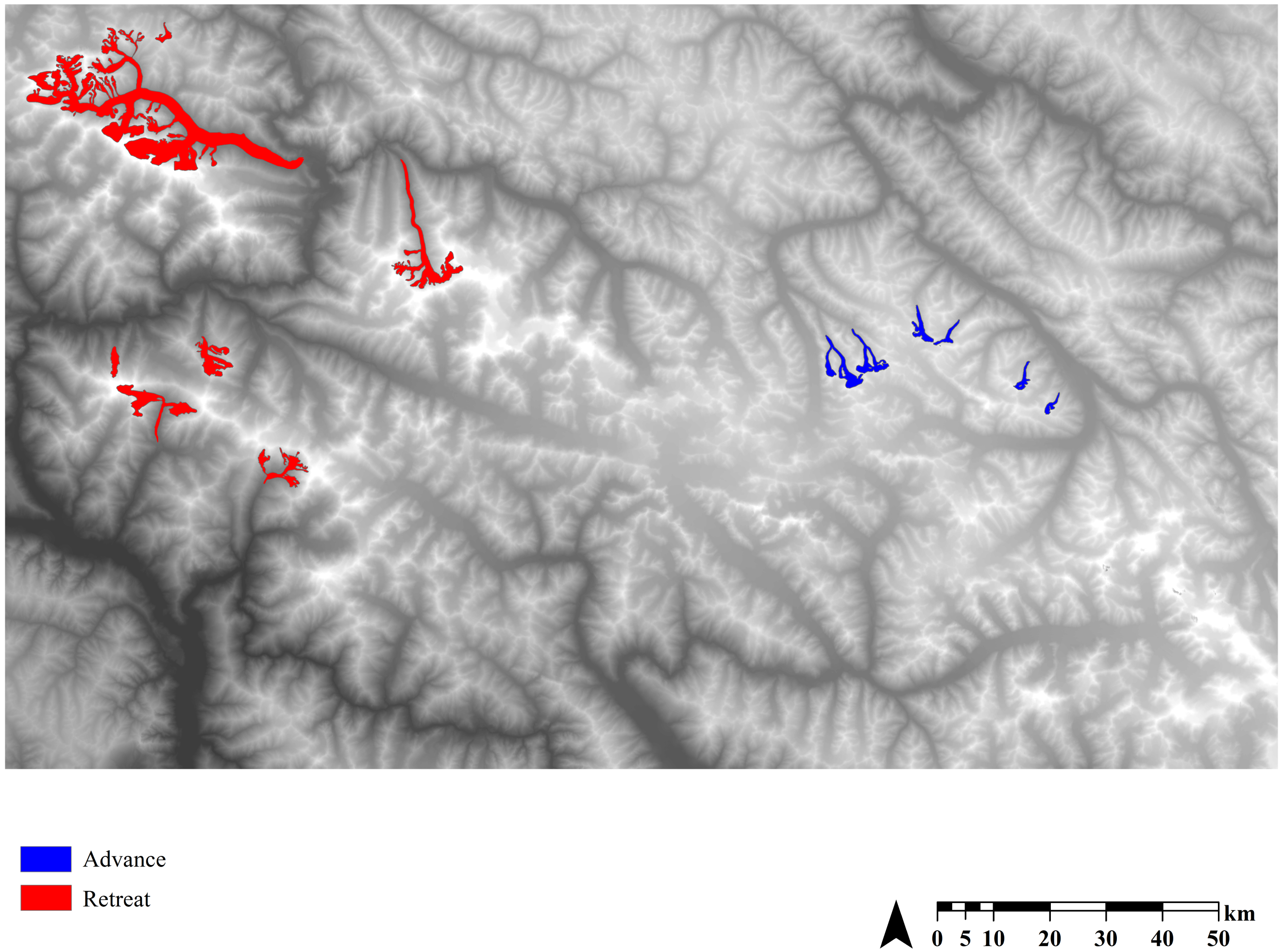

Figure 5.24: Advancing and retreating glaciers as identified by Rankl et al. (2014).

6. DISCUSSION

6.1 Solar radiation modeling

The difference between measured and simulated solar irradiance may be explained through the heterogeneity of daily atmospheric conditions not incorporated in STSRM or the other two GIS-based solar radiation models incorporated in the ArcGIS and QGIS software packages. The new model uses standard atmospheric profiles, and any daily variations in atmospheric constituents, such as water vapor or ozone, are not accounted for. Even so, the simulated total and direct solar irradiance closely matches the observations. Given the selection of days with no or with minimal cloud cover, the correspondence between these is expected and confirms our selection of model parametrization schemes.

Diffuse irradiance is difficult to model because of its strong dependence on local atmospheric conditions. Any deviation from the standard atmospheric profiles implemented by the model in terms of higher or lower abundance of atmospheric constituents leads to differences in measured diffuse irradiance. As illustrated by the diffuse irradiance scatter plot (Figure 4.2), the amount of diffuse solar irradiance is overestimated at lower irradiance values and underestimated at high irradiance values, indicating the expected deviation from standard atmospheric conditions.

With respect to comparison to the solar radiation models within ArcGIS and QGIS, the results show that STSRM and the solar radiation model within GRASS produce simulations with similar spatial patterns for direct irradiance and, to a lesser extent, similar diffuse irradiance, with the differences most likely related to the incorporation of skyview factor in STSRM. At the same time, differences for both direct and diffuse irradiance between STSRM and ArcGIS, and QGIS and ArcGIS, have a distinct spatial pattern and relate to elevation and cosine of incidence angle and elevation, respectively.

The validation performed did not include any information pertaining to topographic effects on surface solar irradiance. The stations utilized for the point validation are all purposefully located so that any topographic effects are minimal, which is a common practice for solar radiation measurement stations. Further validation of the model is required to truly assess its performance in topographically complex terrain. Still, the model is deemed fit for applying to the Karakoram Himalaya study area because of the parametrization utilized accounting for topographic influences (Figure 4.1).

6.2 Surge type glacier characterization

In the following discussion the analyzed variables and the results from the logistic regression analysis of surge type versus non-surge type glaciers are related to system dynamics (Tables 5.4 and 5.5, and Figure 4.9). The results of this study are also discussed in the context of previous glaciological research.

6.2.1 Glacier size

A series of independent variables related to glacier size indicates that larger glaciers are more likely to be of surge type (Figures 5.8, 5.9, 5.16, 5.17). This result is aligned with previous investigations of surge type glacier controls. Barrand and Murray (2006) investigated a suite of geomorphic variables over a set of Karakoram glaciers and found that the median glacier area of surge type glaciers is close to two and a half larger than the median area of non-surge type glaciers (164 km^2 as compared to 68 km^2). Sevestre and Benn (2015) analyzed a global set of glaciers and also found a statistically significant difference between the area of surge type versus non-surge type glaciers collocated in the same geographic region. Pertaining to this study is the finding that the smallest difference in size between the two groups is actually in High Mountain Asia and the Caucasus.

Larger glaciers and larger catchments are related to high magnitude erosional processes. As a positive feedback, glaciers with larger accumulation areas are also intercepting larger amounts of snowfall. This supports the view that surge type glaciers contain more ice, and therefore exhibit more favorable conditions for forming a reservoir area. Also related to surge type behavior is that increased ice thickness also increases the basal ice temperature due to increased pressure, and thus is more favorable to thermal surge initiation (Bennett and Glasser, 2011).

Our study distinguished between planimetric and surface area. The difference between planimetric and surface area within the context of system dynamics is that surface area is more directly related to erosional processes. However, our statistical analysis produced very similar coefficients for the relation between the two types of area representations, on one hand, and the probability of a glacier being of surge type, on the other.

Note that other glacier variables are also related to area, and their significance to surge type probability may be solely due to that. These are glacier perimeter, length, and the total area of a glacier that is covered by debris. Note that, debris cover as a percentage of total glacier area is not a significant variable. However, a characterization of the thickness and constituents of the debris cover may offer insights into the effects of debris cover on the probability of a glacier being of surge type.

6.2.2 Glacier length

Glacier length was found as a distinguishing characteristic of surge type versus non-surge type glaciers by this and by previous studies. Surge type glaciers tend to be longer. A detailed discussion about the relationship between glacier surge type behavior and length is available by Jiskoot et al. (2000) who offer three possible explanations of this phenomena. One is simply the relationship between glacier size and glacier length. Another is that the larger stress gradient in a longer glacier creates more favorable conditions for the development of a trigger zone within the glacier for starting a surge cycle. And a third explanation offered by Jiskoot et al. (2000) is that longer glaciers more easily produce fine-grained sedimentary rocks at the bed, and thus are developing a larger till layer which is in turn related to ice flow instability.

Cuffey and Paterson (2010) provide a summary of surge type glaciers locations with the observation that most surge type glaciers occur in either tectonically active mountain ranges such as the Karakoram mountain range, or in geologic regions with weak bedrock. A deformable bed is thus suggested as a possible condition for inducing surge type behavior in glaciers. If so, this supports the concept of longer glaciers producing a larger till layer, and thus being more favorable to surging.

6.2.3 Glacier complexity

Flow obstruction as a surge mechanism is explored through analysis of glacier complexity (Jiskoot et al., 2003). Independent variables in our analysis that pertain to glacier complexity are branchiness index, and shape index of the glacier and the catchment. Previous work determined a positive relation between high glacier complexity and probability of surge type glaciers (Jiskoot et al., 2003; Barrand and Murray, 2006). Branchiness index as a single input independent variable to logistic regression is significant, and a larger branchiness index increases the probability of a glacier being of surge type. Thus, this finding is aligned with previous work and supports the conclusion that complex glaciers are more favorable to being of surge type due to, for example, greater flow obstruction.

Shape index results for both glaciers and catchments, on the other hand, are significant but show unexpected relation - that lower shape index leads to greater probability of surging. The shape index for this study was computed as the ratio between perimeter and planimetric area, and thus lower shape index was expected to indicate less complex glaciers and catchment. We examined maps of shape index for glaciers (Figure 5.4) and catchment (Figure 5.5). Obvious is that this parameterization of shape index is related to glacier size, with smaller glaciers and catchments exhibiting larger shape index. Thus, our results utilizing this parameterization for shape index are just another confirmation that larger glaciers are more prone to surging. Future work will include more sophisticated parameterization of shape index.

6.2.4 Terrain slope

Most previous studies show that lower terrain slope is more favorable to surge type behavior. It is generally accepted that steeper glaciers flow fast enough to prevent them from the ice mass build up required for a surge cycle (Cuffey and Paterson, 2010). Our results confirm this concept as both slope variables are inversely related to the probability of a glacier being surge type meaning that surge type glaciers occupy flatter terrain than non-surge type glaciers.

6.2.5 Glacier elevation properties

We considered the following elevation properties of a glacier: minimum and maximum altitude, relief, mean altitude, and hypsometric integral. Hypsometric integral (Bishop et al., 2002) of the catchment was also utilized as an independent variable. Of these, the variables with significant coefficients are only maximum altitude and relief.

It is known from climatological and glaciological studies of high tropical mountains, that the precipitation maximum is actually at mid elevations (Mölg et al., 2009). The altitudinal precipitation maximum is not studied for the Karakoram mountain range, especially due to the extreme location, and thus the lack of precipitation measurements at high elevations (Palazzi et al., 2013). A surge cycle requires mass accumulation (Hamilton and Dowdeswell, 1996), so greater mass loadings over surge type glaciers is expected. However, the elevation location of the precipitation maximum in the Karakoram mountain range should be further investigated before maximum altitude could be related to surge type glacier dynamics through the concept of mass loadings.

Another possible explanation of the positive relation between maximum elevation and probability of surging, is the concept of differential denudation and uplift (Bishop and Shroder, 2000). Since surge type glaciers produce more erosion, then greater uplift may be occurring over these highly eroded valleys. This is further supported by the relation between glacier size and erosion rates, with larger glaciers producing greater erosion. But a more simple interpretation is that both the maximum altitude and the relief are related to the size and length of the glaciers, as glaciers originating at higher elevations will be longer when terminating at the same altitude as glacier that originate at lower altitude.

6.2.6 Glacier surface irradiance characteristics

This research established a positive relationship between ablation-season surface irradiance and the probability of a glacier being of surge type. Our research also demonstrated that glaciers that are more exposed (less shielded by the terrain) are more likely to be of surge type. This is the first time that surface irradiance characteristics of surge type versus non-surge type glaciers are compared. Note that cloud cover is not considered in this study, but instead surface irradiance during an idealized cloud-free ablation season is used as an approximation. In summary, our findings indicate that enhanced ablation leads to greater probability of a glacier being of surge type. This indicates greater availability of meltwater and greater basal sliding for surge type glaciers (Cuffey and Paterson, 2010).

6.3 Advancing and retreating glacier characterization

Only a small sample of seven retreating and six advancing glaciers is available for a qualitative analysis. All of the advancing glaciers are oriented towards the North or Northeast/Northwest (polewards for Asia) and such an orientation is usually related to lesser amounts of solar irradiance received. However, the difference between the mean surface irradiance during the ablation season for the two glacier categories is very small. At the same time, advancing glaciers are more shielded by the topography given their low diurnal-irradiance kurtosis ratio.

It may be the case that the difference in averaged total surface irradiance over the ablation season between advancing and retreating glaciers is not captured by this glacier sample. However, the difference in kurtosis ratio is remarkable, 0.6 for advancing, and 1.1 for retreating glaciers. As it is expected that advancing glaciers are more shielded by the topography, this result serves as a validation of the kurtosis ratio as an indicator of topographic shielding. However, the glacier sample is not large enough to conclude about probability of advancing versus retreating glaciers as related to geomorphic or surface irradiance characteristics.

7. CONCLUSIONS

The number of GIS-based solar radiation models is limited. Thus, the newly developed solar radiation model is uniquely positioned to improve upon solar radiation models easily accessible within a GIS system. STSRM is developed to better represents solar surface irradiance over complex topography. This permits us to examine the complexities of mountain geodynamics and multiscale topographic effects in a highly glaciated region of the Karakoram mountain range.

As the complexity of the solar radiation model increased due to simulation accuracy enhancements, its computation complexity, both in terms of different arithmetic computations and the required computing cycles, also increased. Therefore, model parallelization was necessary to produce the required simulations.

STSRM was applied to simulate the surface solar irradiance during the ablation season over a portion of the Karakoram mountain range in Pakistan. This unique region is heavily glaciated, and includes a great number of surging glaciers, plus a smaller number of advancing and retreating glaciers. Our research confirmed previous work on the relationship between geomorphic characteristics of the terrain and probability of glaciers being surge type or not. In particular, glacier size, length, complexity, maximum altitude and relief are positively related to the probability of a glacier being of surge-type, while the terrain slope of glaciers is negatively related.

This study is the first time that the effects of the topography on glacier ablation are quantified using glacier surge type as a proxy of glacier dynamics. Even though we only considered clear-sky conditions, we are confident that the results show how glaciers with different surface irradiance characteristics exhibit different dynamics. Less shielded glaciers with greater amount of surface solar irradiance during the ablation season are more prone to surging, offering further confirmation that glacial melt and basal sliding are components of glacier surge mechanisms.

This research is inconclusive about the characterization of advancing versus retreating glaciers because of the small sample. In summary, advancing and retreating glaciers are spatially clustered - advancing to the North of the Biafo and Hispar glacier complex, and retreating glaciers are within the Batura glacier complex. Advancing glaciers are oriented polewards and are a lot more shielded by the terrain than the retreating glaciers.

Demonstrated is also a new concept in quantifying the topographic effect on surface irradiance. The kurtosis of daily surface irradiance curves for each location on the terrain is utilized as an indicator of the topographic effect for that day. In this work, this information is summarized into typical kurtosis patterns over the ablation season as a ratio. Future work will further explore this concept, and aim at developing new approaches for topographic characterization of surface irradiance in complex terrain.

REFERENCES

Ahmad, I., Ambreen, R., Sun, Z., and Deng, W. (2015). Winter-spring precipitation variability in Pakistan. *American Journal of Climate Change*, 4(01):115.

Ahmad, M. J. and Tiwari, G. (2010). Solar radiation models - A review. *International Journal of Energy and Environment*, 1(3):513–532.

Akhtar, M., Ahmad, N., and Booij, M. J. (2008). The impact of climate change on the water resources of Hindukush-Karakorum-Himalaya region under different glacier coverage scenarios. *Journal of Hydrology*, 355(1-4):148–163.

Ångström, A. (1930). On the atmospheric transmission of Sun radiation. II. *Geografiska Annaler*, pages 130–159.

Annamalai, H. and Sperber, K. R. (2016). South asian summer monsoon variability in a changing climate. In de Carvalho, V. L. M. and Jones, C., editors, *The Monsoons and Climate Change: Observations and Modeling*, pages 25–46. Springer International Publishing, Cham.

Anthwal, A., Joshi, V., Sharma, A., and Anthwal, S. (2006). Retreat of Himalayan glaciers - Indicator of climate change. *Nature and Science*, 4(4):53–59.

ArcGIS (2016). ArcGIS Resource Center: Desktop 10.3. `http://resources.arcgis.com/en/home/`. Last checked on February 1, 2016.

Archer, D. R. and Fowler, H. J. (2004). Spatial and temporal variations in precipitation in the Upper Indus Basin, global teleconnections and hydrological implications. *Hydrology and Earth System Sciences*, 8(1):47–61.

Arendt, A., T., Bolch, J., Cogley, A., et al. (2012). Randolph Glacier Inventory - A Dataset of Global Glacier Outlines: Version 3.2. Technical report, Global Land Ice Measurements from Space, Boulder Colorado, USA.

Ashraf, A., Naz, R., and Roohi, R. (2012). Glacial lake outburst flood hazards in Hindukush, Karakoram and Himalayan Ranges of Pakistan: Implications and risk analysis. *Geomatics Natural Hazards & Risk*, 3(2):113–132.

Baig, S. U., Tahir, A. A., Din, A., and Khan, H. (2018). Hypsometric properties of mountain landscape of Hunza River Basin of the Karakoram Himalaya. *Journal of Mountain Science*, 15(9):1881–1891.

Barrand, N. E. and Murray, T. (2006). Multivariate controls on the incidence of glacier surging in the Karakoram Himalaya. *Arctic, Antarctic, and Alpine Research*, 38(4):489–498.

Basnett, S., Kulkarni, A. V., and Bolch, T. (2013). The influence of debris cover and glacial lakes on the recession of glaciers in Sikkim Himalaya, India. *Journal of Glaciology*, 59(218):1035–1046.

Beniston, M. (2003). Climatic change in mountain regions: A review of possible impacts. *Climatic Change*, 59(1-2):5–31.

Benn, D. I., Bolch, T., Hands, K., Gulley, J., Luckman, A., Nicholson, L. I., Quincey, D., Thompson, S., Toumi, R., and Wiseman, S. (2012). Response of debris-covered glaciers in the Mount Everest region to recent warming, and implications for outburst flood hazards. *Earth-Science Reviews*, 114(1-2):156–174.

Benn, D. I. and Owen, L. A. (1998). The role of the Indian summer monsoon and the mid-latitude westerlies in Himalayan glaciation: Review and speculative discussion. *Journal of the Geological Society*, 155(2):353–363.

Bennett, M. M. and Glasser, N. F. (2011). *Glacial geology: Ice sheets and landforms*. John Wiley & Sons, Chichester.

Berger, A. and Loutre, M. F. (1991). Insolation values for the climate of the last 10 million years. *Quaternary Science Reviews*, 10(4):297–317.

Berger, A. L. (1978a). Long-term variations of caloric insolation resulting from the Earth's orbital elements. *Quaternary Researc*, 9(2):139 – 167.

Berger, A. L. (1978b). Long-term variations of daily insolation and quaternary climatic changes. *Journal of the Atmospheric Sciences*, 35(12).

Berk, A., Anderson, G. P., Bernstein, L. S., Acharya, P. K., Dothe, H., Matthew, M. W., Adler-Golden, S. M., Chetwynd, J. J. H., Richtsmeier, S. C., Pukall, B., Allred, C. L., Jeong, L. S., and Hoke, M. L. (1999). MODTRAN4 radiative transfer modeling for atmospheric correction. In *Optical Spectroscopic Techniques and Instrumentation for Atmospheric and Space Research III*, volume 3756 of *SPIE*, pages 348–353.

Berk, A., Conforti, P., Kennett, R., Perkins, T., Hawes, F., and van den Bosch, J. (2014). MODTRAN® 6: A major upgrade of the MODTRAN® radiative transfer code. In *Hyperspectral Image and Signal Processing: Evolution in Remote Sensing (WHISPERS), 2014 6th Workshop on*, pages 1–4. IEEE.

Berk, A. and Hawes, F. (2017). Validation of MODTRAN® 6 and its line-by-line algorithm. *Journal of Quantitative Spectroscopy and Radiative Transfer*, 203:542–556.

Bhambri, R., Hewitt, K., Kawishwar, P., and Pratap, B. (2017). Surge-type and surge-modified glaciers in the Karakoram. *Scientific Reports*, 7(1):15391.

Bhardwaj, A., Joshi, P. K., Snehmani, Singh, M. K., Sam, L., and Gupta, R. D. (2014). Mapping debris-covered glaciers and identifying factors affecting the accuracy. *Cold Regions Science and Technology*, 106-107(0):161–174.

Bhutiyani, M. R., Kale, V. S., and Pawar, N. J. (2010). Climate change and the precipitation variations in the northwestern Himalaya: 1866-2006. *International Journal of Climatology*, 30(4):535–548.

Bird, R. E. and Riordan, C. (1986). Simple solar spectral model for direct and diffuse irradiance on horizontal and tilted planes at the Earth's surface for cloudless atmospheres. *Journal of Climate and Applied Meteorology*, 25(1):87–97.

Bishop, M. and Shroder, J. F. (2004). *Geographic information science and mountain geo-*

morphology. Springer, Verlag.

Bishop, M. P., Bush, A. B. G., Copland, L., Kamp, U., Owen, L. A., Seong, Y. B., and Shroder, John F., J. (2010). Climate change and mountain topographic evolution in the Central Karakoram, Pakistan. *Annals of the Association of American Geographers*, 100(4):772–793.

Bishop, M. P. and Colby, J. D. (2011). Topographic normalization of multispectral satellite imagery. In Singh, V. P., Singh, P., and Haritashya, U. K., editors, *Encyclopedia of Snow, Ice and Glaciers*, pages 1187–1196. Springer, Dordrecht.

Bishop, M. P. and Dobreva, I. D. (2016). Geomorphometry and mountain geodynamics: Issues of scale and complexity. In *Integrating Scale in Remote Sensing and GIS*, pages 189–228. CRC Press.

Bishop, M. P., Dobreva, I. D., and Houser, C. (2015). *Geospatial science and technology for understanding the complexities of the Critical Zone*, pages 523–561. Elsevier, Amsterdam.

Bishop, M. P., Jr., J. F. S., Ali, G., Bush, A. B. G., Haritashya, U. K., Roohi, R., Sarikaya, M. A., and Weihs, B. J. (2014). Remote sensing of glaciers in Afghanistan and Pakistan. In Kargel, J., Leonard, G., Bishop, M., KKääbb, A., and Raup, B., editors, *Global Land Ice Measurements from Space*. Springer.

Bishop, M. P. and Shroder, J. F. (2000). Remote sensing and geomorphometric assessment of topographic complexity and erosion dynamics in the Nanga Parbat massif. 170(1):181–200.

Bishop, M. P., Shroder, J. F., and Ward, J. L. (1995). SPOT multispectral analysis for producing supraglacial debris-load estimates for Batura glacier, Pakistan. *Geocarto International*, 10(4):81–90.

Bishop, M. P., Shroder Jr, J. F., Bonk, R., and Olsenholler, J. (2002). Geomorphic change in high mountains: A western Himalayan perspective. *Global and Planetary Change*, 32(4):311–329.

Blanco-Muriel, M., Alarcón-Padilla, D. C., López-Moratalla, T., and Lara-Coira, M. (2001). Computing the solar vector. *Solar Energy*, 70(5):431 – 441.

Bolch, T., Kulkarni, A., Kääb, A., Huggel, C., Paul, F., Cogley, J. G., Frey, H., Kargel, J. S., Fujita, K., Scheel, M., Bajracharya, S., and Stoffel, M. (2012). The state and fate of Himalayan glaciers. *Science*, 336(6079):310–314.

Bolch, T., Pieczonka, T., Mukherjee, K., and Shea, J. (2017). Brief communication: Glaciers in the Hunza catchment (Karakoram) have been nearly in balance since the 1970s. *The Cryosphere*, 11(1):531.

Bouwer, L. M. (2011). Have disaster losses increased due to anthropogenic climate change? *Bulletin of the American Meteorological Society*, 92(1):39–46.

Brown, R. D. and Robinson, D. A. (2011). Northern Hemisphere spring snow cover variability and change over 1922-2010 including an assessment of uncertainty. *The Cryosphere*, 5(1):219–229.

Buri, P., Pellicciotti, F., Steiner, J. F., Miles, E. S., and Immerzeel, W. W. (2016). A grid-based model of backwasting of supraglacial ice cliffs on debris-covered glaciers. *Annals of Glaciology*, 57(71):199–211.

Bush, A. B., Prentice, M. L., Bishop, M. P., and Shroder Jr, J. F. (2004). Modeling global and regional climate systems: Climate forcing and topography. In *Geographic information science and mountain geomorphology*, pages 403–424.

Bush, A. B. G. (2001). Pacific sea surface temperature forcing dominates orbital forcing of the early Holocene monsoon. *Quaternary Research*, 55(1):25–32.

Bush, A. B. G. (2007). Extratropical Influences on the El Niño-Southern Oscillation through the Late Quaternary. *Journal of Climate*, 20(5):788–800.

Cannon, F., Carvalho, L. M., Jones, C., and Bookhagen, B. (2015a). Multi-annual variations in winter westerly disturbance activity affecting the Himalaya. *Climate Dynamics*, 44(1-2):441–455.

Cannon, F., Carvalho, L. M., Jones, C., and Norris, J. (2015b). Winter westerly disturbance dynamics and precipitation in the western Himalaya and Karakoram: A wave-tracking approach. *Theoretical and Applied Climatology*, pages 1–18.

Carenzo, M., Pellicciotti, F., Mabillard, J., Reid, T., and Brock, B. W. (2016). An enhanced temperature index model for debris-covered glaciers accounting for thickness effect. *Advances in Water Resources*, 94:457–469.

Carmona, F., Rivas, R., and Caselles, V. (2015). Development of a general model to estimate the instantaneous, daily, and daytime net radiation with satellite data on clear-sky days. *Remote Sensing of Environment*, 171:1–13.

Casey, K. and Kääb, A. (2012). Estimation of supraglacial dust and debris geochemical composition via satellite reflectance and emissivity. *Remote Sensing*, 4(9).

Casey, K. A., Kääb, A., and Benn, D. I. (2012). Geochemical characterization of supraglacial debris via in situ and optical remote sensing methods: A case study in Khumbu Himalaya, Nepal. *The Cryosphere*, 6(1):85–100.

Chaâbane, M., Masmoudi, M., and Medhioub, K. (2004). Determination of Linke turbidity factor from solar radiation measurement in northern Tunisia. *Renewable Energy*, 29(13):2065–2076.

Church, J. A. and White, N. J. (2011). Sea-level rise from the late 19th to the early 21st century. *Surveys in Geophysics*, 32(4-5):585–602.

Ciscar, J.-C., Iglesias, A., Feyen, L., Szabó, L., Van Regemorter, D., Amelung, B., Nicholls, R., Watkiss, P., Christensen, O. B., Dankers, R., Garrote, L., Goodess, C. M., Hunt, A., Moreno, A., Richards, J., and Soria, A. (2011). Physical and economic consequences of climate change in Europe. *Proceedings of the National Academy of Sciences*, 108(7):2678–2683.

Clauser, C. (2006). The Earth's thermal regime. In Heinloth, K., editor, *Renewable Energy*, volume 3C of *Landolt-Börnstein - Group VIII Advanced Materials and Technologies*, book section 17, pages 493–548. Springer Berlin Heidelberg.

Clift, P. D. and Plumb, R. A. (2008). *The Asian monsoon: causes, history and effects*, volume 270. Cambridge University Press Cambridge.

Collier, E., Maussion, F., Nicholson, L. I., Mölg, T., Immerzeel, W. W., and Bush, A. B. G. (2015). Impact of debris cover on glacier ablation and atmosphere-glacier feedbacks in the Karakoram. *The Cryosphere*, 9(4):1617–1632.

Collier, E., Mölg, T., Maussion, F., Scherer, D., Mayer, C., and Bush, A. B. G. (2013). High-resolution interactive modelling of the mountain glacier-atmosphere interface: An application over the Karakoram. *Cryosphere*, 7(3):779–795.

Collier, E., Nicholson, L., Brock, B., Maussion, F., Essery, R., and Bush, A. (2014). Representing moisture fluxes and phase changes in glacier debris cover using a reservoir approach. *The Cryosphere*, 8(4):1429–1444.

Comiso, J. C., Parkinson, C. L., Gersten, R., and Stock, L. (2008). Accelerated decline in the Arctic sea ice cover. *Geophysical Research Letters*, 35(1):L01703.

Consortium, R. et al. (2017). Randolph Glacier Inventory–A Dataset of Global Glacier Outlines: Version 6.0: Technical Report, Global Land Ice Measurements from Space, Colorado, USA. *Digital Media. https://doi. org/10.7265*, (5).

Copland, L., Pope, S., Bishop, M. P., Shroder, J. F., Clendon, P., Bush, A., Kamp, U., Seong, Y. B., and Owen, L. A. (2009). Glacier velocities across the central Karakoram. *Annals of Glaciology*, 50(52):41–49.

Cuffey, K. and Paterson, W. S. B. (2010). *Physics of Glaciers*. Academic Press.

Dayton, C. M. (1992). Logistic regression analysis. *Stat*, pages 474–574.

Diaz, H. F. and Markgraf, V. (2000). *El Niño and the Southern Oscillation: multiscale variability and global and regional impacts*. Cambridge University Press.

Dimri, A., Yasunari, T., Wiltshire, A., Kumar, P., Mathison, C., Ridley, J., and Jacob, D.

(2013). Application of regional climate models to the Indian winter monsoon over the western Himalayas. *Science of The Total Environment*, 468-469:S36 – S47.

Dimri, A. P. (2013). Relationship between ENSO phases with Northwest India winter precipitation. *International Journal of Climatology*, 33(8):1917–1923.

DMA (1987). Supplement to the Department of Defense World Geodetic System 1984, Part I, Methods, Techniques, and Data used in WGS 84 Development. Technical Report TR8350.2-A, Deffense Mapping Agency.

DMA (1991). Department of Defense World Geodetic System 1984, Its Definition and Relationships With Local Geodetic Systems". Technical Report TR8350.2 2nd ed., Deffense Mapping Agency.

DMA (1992). Methods for Calculating Solar Position and Day Length including Computer Programs and Subroutines. Technical Report Resource Management Technical Report No. 137, Land Management, Western Australian Department of Agriculture.

Dobreva, I., Bishop, M., and Bush, A. (2017). Climate-glacier dynamics and topographic forcing in the Karakoram Himalaya: Concepts, issues and research directions. *Water*, 9(6):405.

Dozier, J. and Frew, J. (1990). Rapid calculation of terrain parameters for radiation modeling from digital elevation data. *IEEE Transactions on Geoscience and Remote Sensing*, 28(5):963–969.

Dunse, T., Schellenberger, T., Hagen, J. O., Kääb, A., Schuler, T. V., and Reijmer, C. H. (2015). Glacier-surge mechanisms promoted by a hydro-thermodynamic feedback to summer melt. *The Cryosphere*, 9(1):197–215.

Dyurgerov, M. B. and Meier, M. F. (2005). Glaciers and the changing Earth system: A 2004 snapshot. Technical report.

Egholm, D. L., Knudsen, M. F., Clark, C. D., and Lesemann, J. E. (2011). Modeling the flow of glaciers in steep terrains: The integrated second-order shallow ice approximation (iSOSIA). *Journal of Geophysical Research: Earth Surface*, 116(F2).

Filippi, A., Dobreva, I., Klein, A. G., and Jensen, J. R. (2010). Self-organizing map-based applications in remote sensing. In *Self-Organizing Maps*. InTech.

Filippi, L., Palazzi, E., von Hardenberg, J., and Provenzale, A. (2014). Multidecadal Variations in the Relationship between the NAO and Winter Precipitation in the Hindu Kush-Karakoram. *Journal of Climate*, 27(20):7890–7902.

Forsythe, N., Blenkinsop, S., and Fowler, H. (2015). Exploring objective climate classification for the Himalayan arc and adjacent regions using gridded data sources. *Earth System Dynamics*, 6(1):311.

Fowler, H. J. and Archer, D. R. (2006). Conflicting signals of climatic change in the Upper Indus Basin. *Journal of Climate*, 19(17):4276–4293.

Fu, P. (2000). *A geometric solar radiation model with applications in landscape ecology*. PhD dissertation.

Fu, P. and Rich, P. M. (2002). A geometric solar radiation model with applications in agriculture and forestry. *Computers and Electronics in Agriculture*, 37(1-3):25–35.

Gadgil, S., Vinayachandran, P. N., Francis, P. A., and Gadgil, S. (2004). Extremes of the Indian summer monsoon rainfall, ENSO and equatorial Indian Ocean oscillation. *Geophysical Research Letters*, 31(12):L12213.

Gardelle, J., Berthier, E., and Arnaud, Y. (2012). Slight mass gain of Karakoram glaciers in the early twenty-first century. *Nature Geosci*, 5(5):322–325.

Gardelle, J., Berthier, E., Arnaud, Y., and Kääb, A. (2013). Region-wide glacier mass balances over the Pamir-Karakoram-Himalaya during 1999-2011. *The Cryosphere*, 7(4):1263–1286.

Gardner, A. S., Moholdt, G., Cogley, J. G., Wouters, B., Arendt, A. A., Wahr, J., Berthier, E., Hock, R., Pfeffer, W. T., Kaser, G., Ligtenberg, S. R. M., Bolch, T., Sharp, M. J., Hagen, J. O., van den Broeke, M. R., and Paul, F. (2013). A reconciled estimate of glacier contributions to sea level rise: 2003 to 2009. *Science*, 340(6134):852–857.

Ghosh, S., Pandey, A. C., and Nathawat, M. S. (2014). Mapping of debris-covered glaciers in parts of the Greater Himalaya Range, Ladakh, western Himalaya, using remote sensing and GIS. *Journal of Applied Remote Sensing*, 8:18.

Gill, E. C., Rajagopalan, B., and Molnar, P. (2015). Subseasonal variations in spatial signatures of ENSO on the Indian summer monsoon from 1901 to 2009. *Journal of Geophysical Research: Atmospheres*, 120(16):2015JD023184.

Grau, E., Gastellu-Etchegorry, and Jean-Philippe (2013). Radiative transfer modeling in the Earth-Atmosphere system with DART model. *Remote Sensing of Environment*, 139(0):149–170.

Gueymard, C. (1995). SMARTS2, a simple model of the atmospheric radiative transfer of sunshine: Algorithms and performance assessment. Technical Report FSEC-PF-270-95, Florida Solar Energy Center.

Gueymard, C. (2005). SMARTS2, a simple model of the atmospheric radiative transfer of sunshine: Algorithms and performance assessment. Technical Report FSEC-PF-270-95, Florida Solar Energy Center.

Hamilton, G. S. and Dowdeswell, J. A. (1996). Controls on glacier surging in Svalbard. *Journal of Glaciology*, 42(140):157âĂŞ168.

Han, H., Wang, J., Wei, J., and Liu, S. (2010). Backwasting rate on debris-covered Koxkar glacier, Tuomuer mountain, China. *Journal of Glaciology*, 56(196):287–296.

Hanna, E., Navarro, F. J., Pattyn, F., Domingues, C. M., Fettweis, X., Ivins, E. R., Nicholls, R. J., Ritz, C., Smith, B., Tulaczyk, S., Whitehouse, P. L., and Zwally, H. J. (2013). Ice-sheet mass balance and climate change. *Nature*, 498(7452):51–59.

Haritashya, U., Kargel, J., Shugar, D., Leonard, G., Strattman, K., Watson, C., Shean, D., Harrison, S., Mandli, K., and Regmi, D. (2018). Evolution and controls of large glacial lakes in the Nepal Himalaya. *Remote Sensing*, 10(5):798.

Harman, J. R. (1991). *Synoptic climatology of the westerlies: process and patterns*. Association of American Geographers.

Harrison, S., Kargel, J. S., Huggel, C., Reynolds, J., Shugar, D. H., Betts, R. A., Emmer, A., Glasser, N., Haritashya, U. K., Klimes, J., et al. (2018). Climate change and the global pattern of moraine-dammed glacial lake outburst floods.

Helmer, M. and Hilhorst, D. (2006). Natural disasters and climate change. *Disasters*, 30(1):1–4.

Hewitt, K. (2005). The Karakoram anomaly? Glacier expansion and the 'elevation effect,' Karakoram Himalaya. *Mountain Research and Development*, 25(4):332–340.

Hewitt, K. (2011). Glacier change, concentration, and elevation effects in the Karakoram Himalaya, Upper Indus Basin. *Mountain Research and Development*, 31(3):188–200. Hewitt, Kenneth.

Hewitt, K. (2014). *Glaciers of the Karakoram Himalaya: Glacial Environments, Processes, Hazards and Resourcess*. Springer, Dordrecht.

Hofierka, J. and Šurí, M. (2002). The solar radiation model for Open source GIS: implementation and applications. In *International GRASS users conference*.

Hofmann-Wellenhof, B. and Moritz, H. (2006). *Physical Geodesy*. Springer-Verlag Wien, 2nd edition.

Huggett, R. and Cheesman, J. (2002). *Topography and the Environment*. Pearson, 1 edition.

Immerzeel, W. W., van Beek, L. P. H., and Bierkens, M. F. P. (2010). Climate change will affect the Asian Water Towers. *Science*, 328(5984):1382–1385.

Ivanova, S. M. (2013). Estimation of background diffuse irradiance on orthogonal surfaces under partially obstructed anisotropic sky. Part I - Vertical surfaces. *Solar Energy*, 95:376–391.

Jacob, T., Wahr, J., Pfeffer, W. T., and Swenson, S. (2012). Recent contributions of glaciers and ice caps to sea level rise. *Nature*, 482(7386):514–518.

Jacobson, M. Z. (2005). *Fundamentals of Atmospheric Modeling*. Cambridge University Press.

Janes, T. J. and Bush, A. B. G. (2012). The role of atmospheric dynamics and climate change on the possible fate of glaciers in the Karakoram. *Journal of Climate*, 25(23):8308–8327.

Jiskoot, H. (2011). Glacier surging. In Singh, V. P., Singh, P., and Haritashya, U. K., editors, *Encyclopedia of Snow, Ice and Glaciers*, pages 415–428. Springer Netherlands, Dordrecht.

Jiskoot, H., Boyle, P., and Murray, T. (1998). The incidence of glacier surging in Svalbard: evidence from multivariate statistics. *Computers & Geosciences*, 24(4):387–399.

Jiskoot, H., Murray, T., and Boyle, P. (2000). Controls on the distribution of surge-type glaciers in Svalbard. *Journal of Glaciology*, 46(154):412–422.

Jiskoot, H., Murray, T., and Luckman, A. (2003). Surge potential and drainage-basin characteristics in East Greenland. *Annals of Glaciology*, 36:142–148.

Juen, M., Mayer, C., Lambrecht, A., Han, H., and Liu, S. (2014). Impact of varying debris cover thickness on ablation: A case study for Koxkar Glacier in the Tien Shan. *The Cryosphere*, 8(2):377.

Kääb, A., Berthier, E., Nuth, C., Gardelle, J., and Arnaud, Y. (2012). Contrasting patterns of early twenty-first-century glacier mass change in the Himalayas. *Nature*, 488(7412):495–498.

Kääb, A., Treichler, D., Nuth, C., and Berthier, E. (2015). Brief communication: Contending estimates of 2003-2008 glacier mass balance over the Pamir-Karakoram-Himalaya. *The Cryosphere*, 9(2):557–564.

Kääb, A., Wessels, R., Haeberli, W., Huggel, C., Kargel, J. S., and Khalsa, S. J. S. (2003). Rapid ASTER imaging facilitates timely assessment of glacier hazards and disasters. *EOS, Transactions American Geophysical Union*, 84(13):117–121.

Kargel, J., Leonard, G., Shugar, D., Haritashya, U., Bevington, A., Fielding, E., Fujita, K., Geertsema, M., Miles, E., and Steiner, J. (2016). Geomorphic and geologic controls of geohazards induced by Nepal's 2015 Gorkha earthquake. *Science*, 351(6269):aac8353.

Kargel, J. S., Leonard, G. J., Bishop, M. P., Kääb, A., and Raup, B. H. (2014). *Global Land Ice Measurements from Space*. Springer-Verlag Berlin Heidelberg.

Kaser, G., Cogley, J. G., Dyurgerov, M. B., Meier, M. F., and Ohmura, A. (2006). Mass balance of glaciers and ice caps: Consensus estimates for 1961-2004. *Geophysical Research Letters*, 33(19):L19501.

Katiyar, A. K. and Pandey, C. K. (2013). A review of solar radiation models: Part I. *Journal of Renewable Energy*, 2013:11.

Khan, A., Naz, B. S., and Bowling, L. C. (2015). Separating snow, clean and debris covered ice in the Upper Indus Basin, Hindukush-Karakoram-Himalayas, using Landsat images between 1998 and 2002. *Journal of Hydrology*, 521:46–64.

Kienholz, C., Rich, J. L., Arendt, A. A., and Hock, R. (2014). A new method for deriving glacier centerlines applied to glaciers in Alaska and northwest Canada. *The Cryosphere*, 8(2):503–519.

Kirkbride, M. P. (1993). The temporal significance of transitions from melting to calving termini at glaciers in the central Southern Alps of New Zealand. *The Holocene*, 3(3):232–240.

Kniezys, F. X., Abreu, L. W., Anderson, G. P., Chetwynd, J. H., Shettle, E. P., Berk, A., Bernstein, L. S., Robertson, D. C., Acharya, P., Rothman, L. S., Selby, J. E. A., Gallery, W. O., and Clough, S. A. (1996). The MODTRAN 2/3 report and LOWTRAN 7 model. Technical report, Phillips Lab., Geophys. Directorate, PL/GPOS, Hanscom AFB, MA 01731, Contract F19628-91-C-0132,.

Kohonen, T. (1990). The self-organizing map. *Proceedings of the IEEE*, 78(9):1464–1480.

Kraaijenbrink, P. D. A., Shea, J. M., Pellicciotti, F., Jong, S. M. d., and Immerzeel, W. W.

(2016). Object-based analysis of unmanned aerial vehicle imagery to map and characterise surface features on a debris-covered glacier. *Remote Sensing of Environment*, 186:581–595.

Krishnamurthy, L. and Krishnamurthy, V. (2014). Influence of PDO on South Asian summer monsoon and monsoon-ENSO relation. *Climate Dynamics*, 42(9):2397–2410.

Krishnamurthy, V. and Kirtman, B. P. (2009). Relation between Indian Monsoon variability and SST. *Journal of Climate*, 22(17):4437–4458.

Kumar, K. K., Rajagopalan, B., and Cane, M. A. (1999). On the weakening relationship between the Indian monsoon and ENSO. *Science*, 284(5423):2156–2159.

Lang, T. J. and Barros, A. P. (2004). Winter storms in the central Himalayas. *Journal of the Meteorological Society of Japan*, 82(3):829–844.

Li, X.-F., Fowler, H. J., Forsythe, N., Blenkinsop, S., and Pritchard, D. (2018). The karakoram/western tibetan vortex: seasonal and year-to-year variability. *Climate Dynamics*, 51(9):3883–3906.

Li, X.-F., Fowler, H. J., Yu, J., Forsythe, N., Blenkinsop, S., and Pritchard, D. (2019). Thermodynamic controls of the western tibetan vortex on tibetan air temperature. *Climate Dynamics*, 53(7):4267–4290.

Louche, A., Peri, G., and Iqbal, M. (1986). An analysis of Linke turbidity factor. *Solar Energy*, 37(6):393–396.

Lv, M., Guo, H., Lu, X., Liu, G., Yan, S., Ruan, Z., Ding, Y., and Quincey, D. J. (2018). Characterising the behaviour of surge and non-surge type glaciers in the Kingata Mountains, Eastern Pamir, from 1999 to 2016. *The Cryosphere Discussions*, 2019:1–37.

Machguth, H. (2014). Atmospheric science: Glaciers between two drivers. *Nature Climate Change*, 4(1):12–13.

Maity, R. and Nagesh Kumar, D. (2006). Bayesian dynamic modeling for monthly Indian summer monsoon rainfall using El Niño-Southern Oscillation (ENSO) and Equatorial

Indian Ocean Oscillation (EQUINOO). *Journal of Geophysical Research: Atmospheres*, 111(D7):D07104.

Mantua, N. J., Hare, S. R., Zhang, Y., Wallace, J. M., and Francis, R. C. (1997). A Pacific Interdecadal Climate Oscillation with impacts on salmon production. *Bulletin of the American Meteorological Society*, 78(6):1069–1079.

Maussion, F., Butenko, A., Eis, J., Fourteau, K., Jarosch, A. H., Landmann, J., Oesterle, F., Recinos, B., Rothenpieler, T., Vlug, A., Wild, C. T., and Marzeion, B. (2018a). The Open Global Glacier Model (OGGM) v1.0. *Geoscientific Model Development Discussions*, 2018:1–33.

Maussion, F., Rothenpieler, T., Recinos, B., Vlug, A., Marzeion, B., Oesterle, F., Landmann, J., Jarosch, A., Eis, J., Butenko, A., and Smith, S. (2018b). OGGM/oggm: v1.0.0.

Mayer, C., Lambrecht, A., Belo, M., Smiraglia, C., and Diolaiuti, G. (2006). Glaciological characteristics of the ablation zone of Baltoro glacier, Karakoram, Pakistan. *Annals of Glaciology*, 43:123–131.

Mayer, C., Lambrecht, A., Oerter, H., Schwikowski, M., Vuillermoz, E., Frank, N., and Diolaiuti, G. (2014). Accumulation studies at a high elevation glacier site in Central Karakoram. *Advances in Meteorology*, page 12.

Mayewski, P. A. and Jeschke, P. A. (1979). Himalayan and Trans-Himalayan glacier fluctuations since AD 1812. *Arctic and Alpine Research*, 11(3):267–287.

McKenney, D. W. (1999). Calibration and sensitivity analysis of a spatially-distributed solar radiation model. *International Journal of Geographical Information Science*, 13(1):49–65.

Meharrar and Bachari (2014). Modelling of radiative transfer of natural surfaces in the solar radiation spectrum: Development of a satellite data simulator (SDDS). *International Journal of Remote Sensing*, 35(4):1199–1216.

Mészároš, I., Miklánek, P., and Parajka, J. (2002). Solar energy income modelling in mountainous areas. In Holko, L., Miklánek, P., Parajka, J., and Kostka, Z., editors, *ERB and NEFRIEND Proj.5 Conf. Interdisciplinary Approaches in Small Catchment Hydrology: Monitoring and Research*, pages 127–135.

Meyers, L. S., Gamst, G., and Guarino, A. J. (2016). *Applied multivariate research: Design and interpretation*. Sage publications.

Mihalcea, C., Mayer, C., Diolaiuti, G., D'Agata, C., Smiraglia, C., Lambrecht, A., Vuillermoz, E., and Tartari, G. (2008). Spatial distribution of debris thickness and melting from remote-sensing and meteorological data, at debris-covered Baltoro glacier, Karakoram, Pakistan. In Jacka, J., editor, *Annals of Glaciology, Vol 48*, volume 48 of *Annals of Glaciology*, pages 49–57.

Mihalcea, C., Mayer, C., Diolaiuti, G., Lambrecht, A., Smiraglia, C., and Tartari, G. (2006). Ice ablation and meteorolopical conditions on the debris-covered area of Baltoro glacier, Karakoram, Pakistan. In MosleyThompson, E. and Thompson, L. G., editors, *Annals of Glaciology, Vol 43, 2006*, volume 43 of *Annals of Glaciology*, pages 292–300.

Mölg, N., Bolch, T., Rastner, P., Strozzi, T., and Paul, F. (2018). A consistent glacier inventory for the Karakoram and Pamir regions derived from Landsat data: Distribution of debris cover and mapping challenges. *Earth System Science Data Discussions*, 2018:1–44.

Mölg, T., Chiang, J. C., Gohm, A., and Cullen, N. J. (2009). Temporal precipitation variability versus altitude on a tropical high mountain: Observations and mesoscale atmospheric modelling. *Quarterly Journal of the Royal Meteorological Society: A journal of the atmospheric sciences, applied meteorology and physical oceanography*, 135(643):1439–1455.

Mölg, T., Maussion, F., and Scherer, D. (2014). Mid-latitude westerlies as a driver of glacier variability in monsoonal High Asia. *Nature climate change*, 4(1):68–73.

Moritz, H. (1988). Geodetic reference system 1980. *Bulletin géodésique*, 62:348–358.

Muhammad Iqbal (1983). *Introduction to Solar Radiation*. Academic Press.

Mukul, M., Srivastava, V., Jade, S., and Mukul, M. (2017). Uncertainties in the Shuttle Radar Topography Mission (SRTM) heights: Insights from the Indian Himalaya and Peninsula. *Scientific Reports*, 7.

NASA (2018). Nasa astronomical unit. `https://cneos.jpl.nasa.gov/glossary/au.html/`.

Natural-Capital-Project (2018). Natural capital project. `https://naturalcapitalproject.stanford.edu/software/`.

Newman, M., Alexander, M. A., Ault, T. R., Cobb, K. M., Deser, C., Lorenzo, E. D., Mantua, N. J., Miller, A. J., Minobe, S., Nakamura, H., Schneider, N., Vimont, D. J., Phillips, A. S., Scott, J. D., and Smith, C. A. (2016). The Pacific Decadal Oscillation, revisited. *Journal of Climate*, 29(12):4399–4427.

NIMA (2000). Department of Defense World Geodetic System 1984, its definition and relationships with local geodetic systems. Technical Report TR8350.2 3rd ed., National Imagery and Mapping Agency.

Nuth, C. and Kääb, A. (2011). Co-registration and bias corrections of satellite elevation data sets for quantifying glacier thickness change. *The Cryosphere*, 5(1):271.

Palazzi, E., Hardenberg, J., and Provenzale, A. (2013). Precipitation in the Hindu-Kush Karakoram Himalaya: Observations and future scenarios. *Journal of Geophysical Research: Atmospheres*, 118(1):85–100.

Pant, G., Kumar, P. P., Revadekar, J. V., and Singh, N. (2018). Climate change impacts: Central Himalaya. In *Climate Change in the Himalayas*, pages 119–134. Springer.

Parmesan, C. (2006). Ecological and evolutionary responses to recent climate change. *Annual Review of Ecology, Evolution, and Systematics*, 37(1):637–669.

Patz, J. A., Campbell-Lendrum, D., Holloway, T., and Foley, J. A. (2005). Impact of regional climate change on human health. *Nature*, 438(7066):310–317.

Paul, F., Bolch, T., Kääb, A., Nagler, T., Nuth, C., Scharrer, K., Shepherd, A., Strozzi, T., Ticconi, F., Bhambri, R., Berthier, E., Bevan, S., Gourmelen, N., Heid, T., Jeong, S., Kunz, M., Lauknes, T. R., Luckman, A., Boncori, J. P. M., Moholdt, G., Muir, A., Neelmeijer, J., Rankl, M., VanLooy, J., and Van Niel, T. (2015). The glaciers climate change initiative: Methods for creating glacier area, elevation change and velocity products. *Remote Sensing of Environment*, 162:408–426.

Pendleton, S. L., Miller, G. H., Lifton, N., Lehman, S. J., Southon, J., Crump, S. E., and Anderson, R. S. (2019). Rapidly receding Arctic Canada glaciers revealing landscapes continuously ice-covered for more than 40,000 years. *Nature communications*, 10(1):445.

Pilkey, O. H. and Cooper, J. A. G. (2004). Society and sea level rise. *Science*, 303(5665):1781–1782.

Piri, J. and Kisi, O. (2015). Modelling solar radiation reached to the Earth using ANFIS, NN-ARX, and empirical models (Case studies: Zahedan and Bojnurd stations). *Journal of Atmospheric and Solar-Terrestrial Physics*, 123:39–47.

Postel, S. L. (2003). Securing water for people, crops, and ecosystems: new mindset and new priorities. In *Natural Resources Forum*, volume 27, pages 89–98. Wiley Online Library.

Pratt-Sitaula, B., Burbank, D. W., Heimsath, A. M., Humphrey, N. F., Oskin, M., and Putkonen, J. (2011). Topographic control of asynchronous glacial advances: A case study from Annapurna, Nepal. *Geophysical Research Letters*, 38.

Quincey, D. J., Braun, M., Glasser, N. F., Bishop, M. P., Hewitt, K., and Luckman, A. (2011). Karakoram glacier surge dynamics. *Geophysical Research Letters*, 38(18):L18504.

Quincey, D. J., Copland, L., Mayer, C., Bishop, M., Luckman, A., and Belo, M. (2009). Ice velocity and climate variations for Baltoro Glacier, Pakistan. *Journal of Glaciology*, 55(194):1061–1071.

Quincey, D. J., Glasser, N. F., Cook, S. J., and Luckman, A. (2015). Heterogeneity in Karakoram glacier surges. *Journal of Geophysical Research: Earth Surface*, 120(7):1288–1300.

Raghavan, K. (1973). Tibetan anticyclone and tropical easterly jet. *Pure and Applied Geophysics*, 110(1):2130–2142.

Rankl, M., Kienholz, C., and Braun, M. (2014). Glacier changes in the Karakoram region mapped by multimission satellite imagery. *The Cryosphere*, 8(3):977–989.

Rasul, G. (2010). The role of the Himalayan mountain systems in food security and agricultural sustainability in South Asia. *International Journal of Rural Management*, 6(1):95–116.

Rasul, G. (2014). Food, water, and energy security in South Asia: A nexus perspective from the Hindu Kush Himalayan region. *Environmental Science & Policy*, 39:35–48.

Rasul, G. (2015). Water for growth and development in the Ganges, Brahmaputra, and Meghna basins: An economic perspective. *International Journal of River Basin Management*, 13(3):387–400.

Reid, T. and Brock, B. (2014). Assessing ice-cliff backwasting and its contribution to total ablation of debris-covered Miage glacier, Mont Blanc massif, Italy. *Journal of Glaciology*, 60(219):3–13.

Reynolds, J. M. (2000). On the formation of supraglacial lakes on debris-covered glaciers. *IAHS publication*, pages 153–164.

Reznichenko, N., Davies, T., Shulmeister, J., and McSaveney, M. (2010). Effects of debris on ice-surface melting rates: An experimental study. *Journal of Glaciology*, 56(197):384–394.

Richardson, S. D. and Reynolds, J. M. (2000). An overview of glacial hazards in the Himalayas. *Quaternary International*, 65-66(0):31–47.

Roohi, R. (2007). *Research on global changes in Pakistan*, volume Volume 10, pages 329–340. Elsevier.

Rowan, A. V., Egholm, D. L., Quincey, D. J., and Glasser, N. F. (2015). Modelling the feedbacks between mass balance, ice flow and debris transport to predict the response to climate change of debris-covered glaciers in the Himalaya. *Earth and Planetary Science Letters*, 430:427–438.

Rowan, A. V., Quincey, D. J., Gibson, M. J., Glasser, N. F., Westoby, M. J., Irvine-Fynn, T. D., Porter, P. R., and Hambrey, M. J. (2018). The sustainability of water resources in High Mountain Asia in the context of recent and future glacier change. *Geological Society, London, Special Publications*, 462(1):189–204.

Ruiz-Arias, J. A., Tovar-Pescador, J., Pozo-Vázquez, D., and Alsamamra, H. (2009). A comparative analysis of DEM-based models to estimate the solar radiation in mountainous terrain. *International Journal of Geographical Information Science*, 23(8):1049–1076.

Sakai, A. and Fujita, K. (2010). Formation conditions of supraglacial lakes on debris-covered glaciers in the Himalaya. *Journal of Glaciology*, 56(195):177–181.

Sakai, A., Nakawo, M., and Fujita, K. (1998). Melt rate of ice cliffs on the Lirung Glacier, Nepal Himalayas, 1996. *Bull. Glacier Res*, 16:57–66.

Sakai, A., Nakawo, M., and Fujita, K. (2002). Distribution characteristics and energy balance of ice cliffs on debris-covered glaciers, Nepal Himalaya. *Arctic, Antarctic, and Alpine Research*, 34(1):12–19.

Sakai, A., Takeuchi, N., Fujita, K., and Nakawo, M. (2000). Role of supraglacial ponds in the ablation process of a debris-covered glacier in the Nepal Himalayas. *Debris-Covered Glaciers*, (264):119–130.

Scherler, D., Bookhagen, B., and Strecker, M. R. (2011). Spatially variable response of Himalayan glaciers to climate change affected by debris cover. *Nature Geosci*, 4(3):156–

159.

Scherler, D. and Strecker, M. R. (2012). Large surface velocity fluctuations of Biafo Glacier, central Karakoram, at high spatial and temporal resolution from optical satellite images. *Journal of Glaciology*, 58(209):569–580.

Searle, M. P. (1991). *Geology and tectonics of the Karakoram Mountains*. John Wiley & Sons Inc.

Seong, J. C. (2015). Sun position calculator (SPC) for Landsat imagery with geodetic latitudes. *Computers & Geosciences*, 85:68–74.

Seong, Y. B., Bishop, M. P., Bush, A., Clendon, P., Copland, L., Finkel, R. C., Kamp, U., Owen, L. A., and Shroder, J. F. (2009). Landforms and landscape evolution in the Skardu, Shigar and Braldu Valleys, Central Karakoram. *Geomorphology*, 103(2):251–267.

Seong, Y. B., Owen, L. A., Bishop, M. P., Bush, A., Clendon, P., Copland, L., Finkel, R. C., Kamp, U., and Shroder, J. F. (2008). Rates of fluvial bedrock incision within an actively uplifting orogen: Central Karakoram Mountains, northern Pakistan. *Geomorphology*, 97(3):274 – 286.

Sevestre, H. and Benn, D. I. (2015). Climatic and geometric controls on the global distribution of surge-type glaciers: Implications for a unifying model of surging. *Journal of Glaciology*, 61(228):646–662.

Shekhar, M. S., Chand, H., Kumar, S., Srinivasan, K., and Ganju, A. (2010). Climate-change studies in the western Himalaya. *Annals of Glaciology*, 51(54):105–112.

Shepherd, A., Ivins, E., Rignot, E., Smith, B., Van Den Broeke, M., Velicogna, I., Whitehouse, P., Briggs, K., Joughin, I., Krinner, G., et al. (2018). Mass balance of the Antarctic ice sheet from 1992 to 2017. *Nature*, 558:219–222.

Sherpa, S. F., Shrestha, M., Eakin, H., and Boone, C. G. (2019). Cryospheric hazards and risk perceptions in the Sagarmatha (Mt. Everest) National Park and Buffer Zone, Nepal.

Natural Hazards, pages 1–20.

Shrestha, M., Koike, T., Hirabayashi, Y., Xue, Y., Wang, L., Rasul, G., and Ahmad, B. (2015). Integrated simulation of snow and glacier melt in water and energy balance-based, distributed hydrological modeling framework at Hunza River Basin of Pakistan Karakoram region. *Journal of Geophysical Research: Atmospheres*, 120(10):4889–4919.

Shroder, J. F. and Bishop, M. P. (2010). Glaciers of Pakistan. *Satellite image atlas of glaciers of the world: Asia, USGS Professional Paper*.

Shroder, J. F., Owen, L. A., Seong, Y. B., Bishop, M. P., Bush, A., Caffee, M. W., Copland, L., Finkel, R. C., and Kamp, U. (2011). The role of mass movements on landscape evolution in the Central Karakoram: Discussion and speculation. *Quaternary International*, 236(1):34 – 47. Quaternary Paleoenvironmental Change and Landscape Development in Tibet and the Bordering Mountains.

Slater, A. G. (2016). Surface solar radiation in North America: A comparison of observations, reanalyses, satellite, and derived products. *Journal of Hydrometeorology*, 17(1):401–420.

Smart, W. (1970). *Textbook on Spherical Astronomy*. Press Syndicate of the University of Cambridge, 6th edition.

Song, C., Sheng, Y., Ke, L., Nie, Y., and Wang, J. (2016). Glacial lake evolution in the southeastern Tibetan Plateau and the cause of rapid expansion of proglacial lakes linked to glacial-hydrogeomorphic processes. *Journal of Hydrology*, 540:504–514.

Stocker, T., Dahe, Q., Plattner, G., et al. (2013). Working group I contribution to the IPCC Fifth Assessment Report (AR5), climate change 2013: The physical science basis. Technical report.

Stroeve, J. C., Markus, T., Boisvert, L., Miller, J., and Barrett, A. (2014). Changes in Arctic melt season and implications for sea ice loss. *Geophysical Research Letters*, page

2013GL058951.

The Astronomical Almanac (Annual Edition) (2013). *The Astronomical Almanac (Annual Edition)*. U.S. Nautical Almanac Office and Her Majesty's Nautical Almanac Office, UK.

Ugwu, A. and Ugwuanyi, J. (2011). Performance assessment of Hargreaves model in estimating solar radiation in Abuja using minimum climatological data. *International Journal of the Physical Sciences*, 6(31):7285–90.

Van Aalst, M. K. (2006). The impacts of climate change on the risk of natural disasters. *Disasters*, 30(1):5–18.

Vartiainen, E. (2000). A new approach to estimating the diffuse irradiance on inclined surfaces. *Renewable Energy*, 20(1):45–64.

Veettil, B. K., Bianchini, N., Bremer, U. F., Maier, E. L. B., and Simoes, J. C. (2016). Recent variations of supraglacial lakes on the Baltoro Glacier in the central Karakoram Himalaya and its possible teleconnections with the pacific decadal oscillation. *Geocarto International*, 31(1):109–119.

Veettil, B. K., Franz Bremer, U., Efrain Bica Grondona, A., and Florencio De Souza, S. (2014). Recent changes occurred in the terminus of the Debris-covered Bilafond Glacier in the Karakoram Himalayas using remotely sensed images and digital elevation models (1978-2011). *Journal of Mountain Science*, 11(2):398–406.

Velicogna, I. (2009). Increasing rates of ice mass loss from the Greenland and Antarctic ice sheets revealed by GRACE. *Geophysical Research Letters*, 36(19).

Vellinga, P. and Leatherman, S. (1989). Sea level rise, consequences and policies. *Climatic Change*, 15(1-2):175–189.

Vindel, J., Polo, J., and Zarzalejo, L. (2015). Modeling monthly mean variation of the solar global irradiation. *Journal of Atmospheric and Solar-Terrestrial Physics*, 122:108–118.

Vindel, J. M. and Polo, J. (2014). Markov processes and Zipf's law in daily solar irradiation at Earth's surface. *Journal of Atmospheric and Solar-Terrestrial Physics*, 107:42–47.

Vörösmarty, C. J., Green, P., Salisbury, J., and Lammers, R. B. (2000). Global water resources: Vulnerability from climate change and population growth. *Science*, 289(5477):284–288.

Wagnon, P., Linda, A., Arnaud, Y., Kumar, R., Sharma, P., Vincent, C., Pottakkal, J. G., Berthier, E., Ramanathan, A., Hasnain, S. I., and Chevallier, P. (2007). Four years of mass balance on Chhota Shigri Glacier, Himachal Pradesh, India, a new benchmark glacier in the western Himalaya. *Journal of Glaciology*, 53(183):603–611.

Wake, C. P. (1989). Glaciochemical investigations as a tool for determining the spatial and seasonal variation of snow accumulation in the central Karakorum, northern Pakistan. *Annals of Glaciology*, 13:279–284.

Walther, G.-R., Post, E., Convey, P., Menzel, A., Parmesan, C., Beebee, T. J. C., Fromentin, J.-M., Hoegh-Guldberg, O., and Bairlein, F. (2002). Ecological responses to recent climate change. *Nature*, 416(6879):389–395.

Webster, P. J. and Yang, S. (1992). Monsoon and Enso: Selectively Interactive Systems. *Quarterly Journal of the Royal Meteorological Society*, 118(507):877–926.

Weng, F., Yong, H., and Van Deist, P. (2005). JCSDA Community Radiative Transfer Model (CRTM). In *Proceedings of 14th International TOVS Study Conference. Beijing*.

Wilcox, S. (2012). National solar radiation database 1991-2010 update: User's manual. Technical report, National Renewable Energy Laboratory.

Wild, M. and B., L. (2010). The Earth radiation balance as driver of the global hydrological cycle. *Environmental Research Letters*, 5(2):025203.

Wild, M., Folini, D., Schär, C., Loeb, N., Dutton, E. G., and König-Langlo, G. (2013). The global energy balance from a surface perspective. *Climate Dynamics*, 40(11-12):3107–3134.

Xu, J., Grumbine, R. E., Shrestha, A., Eriksson, M., Yang, X., Wang, Y. U. N., and Wilkes,

A. (2009). The Melting Himalayas: Cascading effects of climate change on water, biodiversity, and livelihoods. *Conservation Biology*, 23(3):520–530.

Yan, G., Wang, T., Jiao, Z., Mu, X., Zhao, J., and Chen, L. (2016). Topographic radiation modeling and spatial scaling of clear-sky land surface longwave radiation over rugged terrain. *Remote Sensing of Environment*, 172:15–27.

Yanai, M. and Wu, G.-X. (2006). *Effects of the Tibetan Plateau*, pages 513–549. Springer Berlin Heidelberg, Berlin, Heidelberg.

Yao, T., Thompson, L., Yang, W., Yu, W., Gao, Y., Guo, X., Yang, X., Duan, K., Zhao, H., and Xu, B. (2012). Different glacier status with atmospheric circulations in Tibetan Plateau and surroundings. *Nature Climate Change*, 2(9):663–667.

Yu, W. S., Yao, T. D., Kang, S. C., Pu, J. C., Yang, W., Gao, T. G., Zhao, H. B., Zhou, H., Li, S. H., Wang, W. C., and Ma, L. L. (2013). Different region climate regimes and topography affect the changes in area and mass balance of glaciers on the north and south slopes of the same glacierized massif (the West Nyainqentanglha Range, Tibetan Plateau). *Journal of Hydrology*, 495:64–73.

Zafar, M. U., Ahmed, M., Rao, M. P., Buckley, B. M., Khan, N., Wahab, M., and Palmer, J. (2016). Karakorum temperature out of phase with hemispheric trends for the past five centuries. *Climate Dynamics*, 46(5-6):1943–1952.

Zhang, X., Liang, S., Wild, M., and Jiang, B. (2015). Analysis of surface incident shortwave radiation from four satellite products. *Remote Sensing of Environment*, 165:186–202.

APPENDIX A

NOTATION

a Semi-major axis of the reference ellipsoid [m].

a_o Semi-major axis of the orbit [km].

b Semi-minor axis of the reference ellipsoid [m].

D Sun-Earth distance [m] or [km].

D_m Mean Sun-Earth distance [m] or [km].

D_c Day of year.

E Liner eccentricity of the reference ellipsoid [m].

E^0 Exoatmospheric spectral irradiance at normal to the Sun surface [W m$^{-2}\mu$m^{-1}].

E_m^0 Exoatmospheric spectral irradiance at normal to the Sun surface and at mean Sun-Earth distance [W m$^{-2}\mu$m^{-1}].

E_a Diffuse-skylight aerosol-scattered spectral irradiance [W m$^{-2}\mu$m^{-1}].

E_b Direct/beam spectral irradiance [W m$^{-2}\mu$m^{-1}].

E_{bn} Direct/beam spectral irradiance at normal to the Sun surface [W m$^{-2}\mu$m^{-1}].

E_d Diffuse-skylight spectral irradiance [W m$^{-2}\mu$m^{-1}].

E_d^h Diffuse-skylight spectral irradiance on a horizontal surface [W m$^{-2}\mu$m^{-1}].

E_g Diffuse-skylight spectral irradiance scattered multiple times between ground and sky [W m$^{-2}\mu$m^{-1}].

E_r Diffuse-skylight Rayleigh-scattered spectral irradiance [W m$^{-2}\mu$m^{-1}].

E_t Total surface irradiance [W m$^{-2}\mu$m^{-1}].

E_t^h Total surface irradiance on a horizontal surface [W m$^{-2}\mu$m^{-1}]

ET Equation of Time [decimal hours] or [radians].

e Orbital eccentricity [dimensionless].

e_{re} First numerical eccentricity of the reference ellipsoid [dimensionless].

e'_{re} Second numerical eccentricity of the reference ellipsoid [dimensionless].

F_{ec} Eccentricity correction factor [dimensionless].

F_s The fraction of aerosol scatter downward [dimensionless].

f The ellipsoidal flattening of the reference ellipsoid [dimensionless].

f^* Gravitational flattening [dimensionless].

$G = 6.6270 \times 10^{-11}$ Universal gravitational constant [$\mathrm{m}^3\,\mathrm{kg}^{-1}\,\mathrm{s}^{-2}$].

GM The product of the universal gravitational constant and the mass of Earth.

GMT Greenwich mean time, same as UT [decimal hours].

g_a Aerosol asymmetry factor [dimensionless].

g_e Ellipsoid gravity at the equator [$\mathrm{m\,s^{-2}}$].

g_h Theoretical ellipsoid gravity above or below the ellipsoid [$\mathrm{m\,s^{-2}}$].

g_p Ellipsoid gravity at the poles $[\mathrm{m\,s^{-2}}]$.

g_t Theoretical ellipsoid gravity at the ellipsoid surface $[\mathrm{m\,s^{-2}}]$.

g_u The component of $\vec{g}_{total}$ in the u direction $[\mathrm{m\,s^{-2}}]$.

g_β The component of $\vec{g}_{total}$ in the β direction $[\mathrm{m\,s^{-2}}]$.

$g*$ True gravitational acceleration $[\mathrm{m\,s^{-2}}]$.

$\vec{g}_{total}$ Theoretical gravity vector $[\mathrm{m\,s^{-2}}]$.

H Height relative to sea level [m] or [km].

H_{ref} Reference height above sea level [km].

H_s Scale height of the atmosphere [km].

H_{GMS} Hour angle of the mean Sun at the Greenwich meridian [radians].

H_{MS} Hour angle of the mean Sun [radians].

H_{TS} Hour angle of the true Sun [radians].

h Height relative to the ellipsoid [m].

k Numerical abbreviation [dimensionless].

$k_B = 1.380658 \times 10^{-23}$ Stephan-Boltzman constant $[\mathrm{kg\,m^2\,s^{-2}\,K^{-1}\,molec.^{-1}}]$.

M_a Mean anomaly [radians].

M_e Earth's mass [kg].

$\bar{M} = 4.8096 \times 10^{-26}$ The average mass of one air molecule $[\mathrm{kg}]$.

m Optical/air mass [dimensionless].

m_a Numerical abbreviation [dimensionless].

m_d Molecular weight of dry air [kg].

m_v Molecular weight of water vapor [kg].

n_d Number of moles of dry air.

n_v Number of moles of water vapor.

P_c Atmospheric pressure correction [dimensionless].

p_a Atmospheric pressure $[\mathrm{hPa}]$ or [mb].

p_{0a} Atmospheric pressure at sea level $[\mathrm{hPa}]$ or [mb].

$p_{a,ref}$ Atmospheric pressure at a reference height z_{ref} $[\mathrm{hPa}]$.

p_d Partial air pressure exerted by dry air $[\mathrm{hPa}]$.

p_v Partial air pressure exerted by water vapor $[\mathrm{hPa}]$.

q Numerical abbreviation [radians].

q_0 Numerical abbreviation [radians].

q' Numerical abbreviation [radians].

q_v Specific humidity $[\mathrm{kg\ kg^{-1}}]$.

R Local ellipsoidal radius [m].

R_n Curvature in the prime vertical [m].

$R_v = 4.6140$ Gas constant for water vapor for dry air [m^3 hPa kg^{-1} K^{-1}].

$R' = 2.8704$ Gas constant for dry air [m^3 hPa kg^{-1} K^{-1}].

T Temperature [K] or [$\circ C$].

T_v Virtual temperature [K].

T_{MS} Mean solar time [decimal hours].

T_{TS} True solar time [decimal hours].

$\mathbf{T}$ Transmission coefficient [dimensionless].

$\mathbf{T}^{\downarrow}$ Total downward atmospheric transmittance coefficient [dimensionless].

$\mathbf{T}_a$ Aerosol atmospheric transmittance coefficient [dimensionless].

$\mathbf{T}_{aa}$ Transmittance term for aerosol absorption [dimensionless].

$\mathbf{T}_{as}$ Transmittance term for aerosol scattering [dimensionless].

$\mathbf{T}_r$ Rayleigh atmospheric transmittance coefficient [dimensionless].

$\mathbf{T}_{O_3}$ Ozone atmospheric transmittance coefficient [dimensionless].

$\mathbf{T}_{gas}$ Miscellaneous gases atmospheric transmittance coefficient [dimensionless].

$\mathbf{T}_{H_2O}$ Water vapor atmospheric transmittance coefficient [dimensionless].

UT Universal time, same as GMT [decimal hours].

u Semi-minor axis of the ellipsoid of revolution that passes through a point [m].

u_{O_3} Effective path length for ozone [dimensionless].

V Volume [m^3].

v_A True anomaly [radians].

w Numerical abbreviation used in the computation of gravitational acceleration [m].

w_p Total precipitable water [$g\ cm^{-2}$] or [cm].

w_v Mass mixing ratio of water vapor [$\mathrm{kg\ kg^{-1}}$].

x Horizontal coordinate of a point in the x-axis of a rectangular coordinate system [m].

y Horizontal coordinate of a point in the y-axis of a rectangular coordinate system [m].

z Vertical coordinate of a point [m].

α Wavelength exponent used in Ångstrøm turbidity formula [dimensionless].

α_d Difference between the geodetic and geocentric latitude [radians].

α_g Ground albedo [dimensionless].

α_s Solar elevation angle (corrected for parallax and refraction) [radians].

α_s^a Apparent solar elevation angle (corrected for parallax) [radians]

α_{sky} Sky reflectivity [dimensionless].

α_{FMS} Right ascension of the fictitious mean Sun [radians].

α_{MS} Right ascension of the mean Sun [radians].

α_{TS} Right ascension of the true Sun [radians].

β Reduced latitude [radians].

β The Ångstrøm turbidity coefficient [dimensionless].

β_λ Numerical abbreviation [dimensionless].

δ Solar declination [radians].

δg_A Atmospheric gravity correction.

$\delta\theta_p$ Parallax correction [radians].

$\delta\theta_r$ Atmospheric refraction correction [radians].

$\delta\phi_{gc}$ Grid convergence [radians].

ϵ Obliquity of the orbit [radians].

θ_i Solar incidence angle [radians].

θ_s Solar zenith angle (corrected for parallax and atmospheric refraction) [radians].

$\theta_{s,deg}$ Solar zenith angle (corrected for parallax and atmospheric refraction) [degrees].

θ_t Terrain slope angle [radians].

θ_s^g Geocentric solar zenith angle [radians].

θ_s^a Apparent solar zenith angle (corrected for parallax) [radians].

λ Wavelength [μm].

λ_l Geodetic longitude [rad].

λ_{cm} Longitude of the central meridian of the projection [radians] or [degrees].

λ_{MS0} Longitude of the mean Sun at the vernal equinox [radians].

λ_{MS} Longitude of the mean Sun [radians].

λ_{TS} Longitude of the true Sun [radians].

π Mathematical constant [dimensionless].

ρ_a Air density [$\mathrm{kg\ m^{-3}}$].

ρ_d Density of dry air [$\mathrm{kg\ m^{-3}}$].

ρ_v Density of water vapor [$\mathrm{kg\,m^{-3}}$].

τ Optical thickness/depth [dimensionless].

τ_a Aerosol optical thickness/depth [dimensionless].

ϕ_s^{nc} Solar azimuth angle (not corrected for grid convergence) [radians].

ϕ_s Solar azimuth angle (corrected for grid convergence) [radians].

ϖ Longitude of perihelion [radians].

φ Geodetic latitude [radians].

φ_{gc} Geocentric latitude [radians].

Ω Angular velocity of Earth [$\mathrm{rad/s}$].

ω Aerosol single scattering albedo [dimensionless].